Nonlinear Dynamics of Trapped Beams

Dissertation

zur Erlangung des akademischen Grades
doctor rerum naturalium (Dr. rer. nat.)

vorgelegt dem Rat der
Physikalisch-Astronomischen Fakultät
der Friedrich-Schiller-Universität Jena

von

Diplomphysiker Stefan Skupin
geboren am 8. Mai 1976 in Düsseldorf

Gutachter

1. ______________________

2. ______________________

3. ______________________

Tag der letzten Rigorosumsprüfung: ______________________

Tag der öffentlichen Verteidigung: ______________________

Contents

1. Introduction 1

2. Modeling the propagation of trapped beams 6

2.1. Beam propagation in a weak-guiding nonlinear optical waveguide . . . 8
2.2. Femtosecond pulsed beam propagation in air 11

3. Beams in a nonlinear optical waveguide 20

3.1. Stability of weakly nonlinear linearly guided beams 21
  3.1.1. Linear modes and nonlinear bound states 22
  3.1.2. Stability analysis of nonlinear bound states 23
  3.1.3. Stability criterion for low-power bound states 28
  3.1.4. Numerical results 32
3.2. Influence of the waveguide on highly nonlinear collapsing beams 35
  3.2.1. Collapse in the two dimensional Nonlinear Schrödinger Equation 37
  3.2.2. Collapse behavior in the presence of a waveguide 40
  3.2.3. Numerical results 42

4. High-intense femtosecond pulsed beams in air 45

4.1. Dynamics of a single filaments 47
  4.1.1. Rotationally symmetric solution 47
  4.1.2. Azimuthal perturbation analysis 51
4.2. Multiple filamentation of femtosecond pulsed beams 55
  4.2.1. The time-averaged model 55
  4.2.2. Time-averaged versus fully space-time-resolved simulations . . . 62
  4.2.3. Time-averaged simulations versus long-range experiments 67
4.3. Interaction of light filaments with obscurants in aerosols 77
  4.3.1. Single filament-droplet interaction 78
  4.3.2. Multifilamentation transmission through fog 83

5. Conclusion and further prospects 86

Bibliography 91
- References . . . 91
- List of publications . . . 99

A. Mathematical details i
- A.1. Components of unstable modes have equal norm . . . i
- A.2. Power integral and Hamiltonian are constants of motion . . . ii
- A.3. Computing the virial . . . ii
- A.4. Spectral problem for soliton stability against non-isotropic perturbations iii

B. Numerical details v
- B.1. Numerical schemes for pulsed-beam propagation in air . . . v
  - B.1.1. (2D+1)-dimensional time-averaged code . . . vii
  - B.1.2. Radial code . . . viii
  - B.1.3. (3D+1)-dimensional code . . . ix
- B.2. Complementary numerical aspects . . . ix

C. Symbols and conventions xi

Zusammenfassung xiii

Acknowledgments xiv

Ehrenwörtliche Erklärung xv

Lebenslauf xvi

1. Introduction

This thesis is about the nonlinear propagation of light in waveguides and homogeneous transparent media, namely the atmosphere. In both systems light is spatially trapped, although the underlying physics is a completely different issue. In the waveguide this trapping is a linear effect resulting in localized beam shapes (modes) which do not diffract. In homogeneous media trapping is the result of a nonlinear effect, since in the linear regime any localized beam shape broadens due to diffraction. Nonlinear trapping is usually called self-trapping, because the beam generates its own trap. Moreover, both trapping effects can simultaneously appear in a nonlinear waveguide. With nonlinear waveguide we mean a linear guiding structure made from a nonlinear material. Nevertheless, even though nonlinear light propagation in waveguides and in homogeneous media are different issues, they have a very important feature in common: Both problems can be modeled by an extended nonlinear Schrödinger equation.

The nonlinear Schrödinger equation (NLS) is among the most prominent equations in nonlinear physics, especially in nonlinear optics. It has been studied for more than 40 years, and it is employed in numerous fields well beyond plasma physics and nonlinear optics, where it originally appeared. Gravity waves on deep water follow a NLS equation, a modified NLS equation appears in the theory of superconductivity as Ginzburg-Landau equation, and under certain approximation it can describe the propagation of the so-called Davydov solitons on an a-helix protein (see [1] for details). In the mean-field approximation, the dynamics of Bose-Einstein condensates is described by the Gross-Pitaevskii equation, which is nothing but an extended NLS equation [2]. Moreover, the NLS equation with one transverse dimension is integrable by means of the inverse scattering transform. Other nonlinear propagation equations (e.g., the Korteweg-de-Vries equation), may be reduced to the NLS through multi-scale expansions [3].

As far as the NLS equation is concerned, one of the major issues is its dimensionality n, which crucially determines its features. Here, we use the common terminology "(nD+1)-dimensional NLS equation", where n is the number of transverse dimensions, and the "1" represents the propagation direction. In the first pioneering works concerning self-trapping of optical beams [4, 5] and hydromagnetic waves in plasmas [6], already one (slab shaped beam) and two (cylindrical beam) transverse dimensions were considered. The fundamental difference between the (1D+1)-dimensional and the (2D+1)-dimensional NLS equation lies in the self-trapping itself. For the integrable (1D+1)-dimensional equation, self-trapping leads to stable soliton solutions. The prime example for this system are optical (temporal) solitons in fibers [7, 8]. In contrast to that, for the (2D+1)-dimensional NLS equation (and also for higher dimensions) self-trapping may lead to catastrophic self-focusing and collapse [9]. However, collapse is a mathematical phenomenon which does not take place in the real physical world. The most apparent mechanism to stop the collapse is the modification of the medium by the self-focusing field itself, e.g. ionization, like in the case of high intense light propagation in transparent media [10–12]. Another possibility is to "tame" the self-focusing process by coupling the field to an appropriate potential [13–16].

This thesis is organized in two major parts. First we consider beams in a nonlinear optical waveguide, namely a weakly-guiding structure with a Kerr nonlinearity (Chapters 2.1 and 3). Here a (2D+1)-dimensional NLS equation governs the evolution of the slowly-varying envelope of the electric field. The waveguide can be considered as an additional linear trapping potential. The linear modes of the waveguide have an analog in the nonlinear regime, the nonlinear bound states or spatial "solitons". In fact, the linear modes of the waveguide can be considered as the zero power limit of nonlinear bound states. Because nonlinear bound states are not necessarily stable, we discuss the stability of these solitons. We make use of the fact that in the low power limit the linear modes of the refractive index profile also appear as eigenstates of the operator, which determines the stability of the nonlinear bound states. We show that the knowledge of the spectrum of linear modes is sufficient to determine the stability of the nonlinear solutions in the limit of small powers [S1]. Moreover, an estimate of the growth rate versus power is established [S2]. The stability of similar trapped structures was also investigated, e.g., [13–15]. In particular, it was observed that single (unit) vortices with sufficiently small power could be stable in a parabolic trap and preserve their radial shape, apart from an azimuthal rotation [14, 15]. If the power in the waveguide is increased, linear trapping is progressively replaced by nonlinear trapping. Because of the two transverse dimensions catastrophic self-focusing becomes a main obstacle [17]. We provide analytical evidence that the collapse can be suppressed by the waveguide structure. The threshold power for catastrophic self-focusing can be significantly increased [S3].

The second major part of this thesis concerns the propagation of high-intense femtosecond pulsed beams in the atmosphere (Chapters 2.2 and 4). In the mid-1990s, first experiments on the meter-range propagation of femtosecond (fs) laser pulsed beams were performed [10, 18–20]. In these experiments, infrared laser pulses with a duration of about 100 fs produced narrow filaments of several meters. More than 10 % of the energy was observed to be localized in the near-axis area. This phenomenon is attributed to the initial self-focusing of laser radiation, which originates from the Kerr response of air and leads to an increase of the light intensity. This growth is then saturated by the defocusing action of the electron plasma created by photoionization of air molecules. As a result, the maximum light intensity in the filament does not exceed 10^{14} W/cm^2 for infrared pulses [S4, S5]. If the pulse power is less than a few critical powers for self-focusing in air ($P_{cr} \sim 3$ GW @ 800 nm), only a single filament is created [10, 18, 19]. At higher powers, two or more filaments can be produced and the propagation range may be increased [20–23] [S6]. First experimental observations of kilometer-range propagation were reported in [24]. As novel optical sources access the terawatt (TW) range, it is thus mandatory to understand the dynamics of fs light pulsed beams. Especially important is the understanding of their decay into multiple small-scale structures in view of improving various applications, such as atmospheric remote sensing techniques [24].

Filaments originate from modulational instability (MI) of pulsed beams triggered by the nonlinear response of air. Applied to an optical background, MI breaks up high-power beams into small-scale cells. Each of them convey a power close to $P_{fil} \simeq \pi^2 P_{cr}/4$ [25–27]. These cells are then amplified through the collapse dynamics and relax their inner power to the critical one, until they reach the ionization threshold near which they give rise to various transverse patterns and undergo strong temporal distortions [27] [S7, S8]. At relatively low powers ($\leq 25\ P_{cr}$), a beam may disintegrate into a couple of small spots that fuse as they attain the full ionization regime [22]. This fusion mechanism reduces the ultimate number of output filaments along the propagation axis. For broader beams conveying much higher energies, another scenario was reported [11]. Elaborated from 3D numerical simulations of a central portion of the pulse over a dozen of meters, a propagation sustained by random nucleation of small-scale filaments was proposed: Collapsing cells resulting from MI are regularized via plasma defocusing with very small losses from multiphoton absorption (MPA). Recurrent collapse events, which are fed by the energy reservoir created from anterior defocused filaments, then form an "optically turbulent light guide", which drives the pulsed beam dynamics. This latter scenario contrasts with the simple picture of light guides that stay robust over long distances. We clarify this apparent controversy by showing that beam propagation is driven by the interplay between random nucleation of small-scale cells and relaxation to long waveguides. After a transient stage along which they vary in location and amplitude, filaments triggered by an isotropic noise are confined within distinct clusters, called "optical pillars", whose evolution can be approximated by an averaged-in-time two-dimensional (2D) model derived from the standard propagation equations for ultrashort pulses. Results from this model are compared with space- and time-resolved numerical simulations and experimental observations. Qualitative features in the evolution of the filament patterns are reproduced by the time-averaged model [S9, S10].

Because of their remarkable robustness, femtosecond filaments constitute reliable "tracks" for transmitting laser beams through fog and clouds, which is a key issue for Lidar (Light Detection And Ranging) detection of atmospheric pollutants [24, 28, 29]. In polluted media, e.g., turbid media or aerosols, it is unavoidable that the beam interacts with obscurants. From the experimental point of view, it was demonstrated in [30] that filaments with a mean diameter of 150 μm (2.7 mJ in energy) survived after hitting water or ink droplets as large as 95 μm. Triggered with 7 mJ, 120 fs pulses at infrared wavelength, a "photon bath" of about 2 mm in diameter surrounded the central part of the beam and was suggested to act as an energy reservoir replenishing the filament. Our simulations confirm this spectacular phenomenon and show that the filament is rapidly rebuilt with a minimal loss of energy over a few cm after the interaction region. However, we propose a different explanation for the robustness of the filaments than the "photon bath". Inspired by our 2D time-averaged model [S11], we identify the filament core with a spatial soliton. Direct comparison between fully time resolved and time-averaged simulations reveal that the self-healing process is indeed determined by soliton dynamics [S12]. The replenishment of the beam after the interaction is shown to be too fast to involve the "photon bath" [S13].

From the physical point of view, we deal with nonlinear light propagation in waveguides and homogeneous transparent media. From the mathematical point of view, we deal with generalized nonlinear Schrödinger equations in two and three transverse dimensions. And from the numerical point of view, we deal with massively parallel beam propagation algorithms. Whichever line of sight the reader prefers, all of them have their entitlement. Without a physical motivation, solving complicated partial differential equations as "end in itself" is rather academic. Moreover, direct comparison with physical experimental results offers comprehensive synergy effects. Without adequate mathematical analysis and modeling, we can only describe the phenomena but lack a deeper understanding. Furthermore, completely different physical systems can share a similar mathematical background. Results found in one system can be applied to another. Last but not least, without numerics many problems have to remain unresolved, and there is no use in a sound model without solution. However, this work is written from the physical point of view because it is supposed to be a PhD thesis in physics and the author considers himself to be a physicist. The mathematics and especially numerics involved are therefore explained only so far as physics is concerned. Although we have to keep in mind that to achieve the results presented here a lot of heavy numerical work was necessary.

The experiments shown in this thesis were performed at the Laboratoire de Spectrométrie Ionique et Moléculaire, Université Cl. Bernard Lyon 1, France by the group of Prof. J. P. Wolf. They were performed in the framework of the Teramobile project, funded jointly by the Centre national de la recherche scientifique (CNRS), the Deutsche Forschungsgemeinschaft (DFG), and the French and German ministries of Foreign affairs. The Teramobile web site is `www.teramobile.org`. Simulations were realized on the COMPAQ alpha cluster (TERA) at the Commissariat à l'Énergie Atomique, Direction des Applications Militaires (CEA/DAM) in Bruyères-le-Châtel, France and on the IBM p690 cluster (JUMP) at the Forschungszentrum Jülich, Germany.

2. Modeling the propagation of trapped beams

In this chapter we provide the model equations for the following work, where we treat two different physical setups. First, in Section 2.1 the propagation equation for a beam in an optical waveguide with a Kerr nonlinearity is derived [31]. It is used to motivate the more general Nonlinear Schrödinger Equation (NLS) with an additional potential. This type of equation is treated in Chapter 3. Second, in Section 2.2 we recapitulate the model equations describing the propagation of ultrashort pulses in air [11, 22, 32–34] [S6, S7]. Because the optical field is also governed by an NLS type equation, general techniques in the derivation are similar to those used in Section 2.1. The model latter is used in Chapter 4.

Maxwell's equations

$$\nabla \cdot \vec{E}(\vec{r},t) = \frac{\rho(\vec{r},t) - \nabla \cdot \vec{P}(\vec{r},t)}{\epsilon_0} \tag{2.1a}$$

$$\nabla \cdot \vec{B}(\vec{r},t) = 0 \tag{2.1b}$$

$$\nabla \times \vec{E}(\vec{r},t) = -\frac{\partial}{\partial t}\vec{B}(\vec{r},t) \tag{2.1c}$$

$$\nabla \times \vec{H}(\vec{r},t) = \vec{J}(\vec{r},t) + \epsilon_0 \frac{\partial}{\partial t}\vec{E}(\vec{r},t) + \frac{\partial}{\partial t}\vec{P}(\vec{r},t) \tag{2.1d}$$

are our starting point, where all fields involved, namely the electric field $\vec{E}$, the polarization vector $\vec{P}$, the magnetic field $\vec{H}$, the magnetic induction vector $\vec{B}$, the carrier density ρ and the current density $\vec{J}$, are real valued.

We consider isotropic, non magnetizable media with a nonlinear polarization vector. Moreover, the spectral range of any fields should be far from any material resonances. Then we can use the conventional description of nonlinear optics, and express

$\vec{P}$ as a power series in $\vec{E}$:

$$\begin{aligned}
\widehat{\vec{P}}(\vec{r},\omega) &= \widehat{\vec{P}}^{(1)}(\vec{r},\omega) + \widehat{\vec{P}}^{(3)}(\vec{r},\omega) + \widehat{\vec{P}}^{(5)}(\vec{r},\omega) + \widehat{\vec{P}}^{(7)}(\vec{r},\omega) + \ldots & \text{(2.2a)} \\
\widehat{P}^{(j)}_{\mu}(\vec{r},\omega) &= \epsilon_0 \sum_{\alpha_1\ldots\alpha_j} \int \cdots \int \chi^{(j)}_{\mu\alpha_1\ldots\alpha_j}(\vec{r},-\omega_\sigma;\omega_1,\ldots,\omega_j) & \text{(2.2b)} \\
&\quad \times \widehat{E}_{\alpha_1}(\vec{r},\omega_1)\ldots\widehat{E}_{\alpha_j}(\vec{r},\omega_j)\delta(\omega-\omega_\sigma)d\omega_1\ldots d\omega_j & \\
\omega_\sigma &= \omega_1 + \ldots + \omega_j. & \text{(2.2c)}
\end{aligned}$$

For the magnetic induction we have

$$\widehat{\vec{B}}(\vec{r},\omega) = \mu_0 \widehat{\vec{H}}(\vec{r},\omega). \tag{2.3}$$

For technical convenience, we express these relations in Fourier space, and the according transformations are defined as

$$\begin{aligned}
\widehat{\vec{F}}(\vec{r},\omega) &= \frac{1}{2\pi}\int \vec{F}(\vec{r},t)e^{i\omega t}dt & \text{(2.4)} \\
\vec{F}(\vec{r},t) &= \int \widehat{\vec{F}}(\vec{r},\omega)e^{-i\omega t}d\omega. & \text{(2.5)}
\end{aligned}$$

In Equation (2.2a) we take into account the fact that in isotropic media all susceptibility tensors $\overleftrightarrow{\chi}^{(\mathrm{j})}$, j even, vanish due to spatial symmetry relations [35]. The subscripts μ, α_1, …, α_j in Equation (2.2b) indicate the respective field vector component in Cartesian coordinates. As indicated by the summation sign, α_1, …, α_j are to be summed over x, y, and z. In the following, we specify Equation (2.2a) for the media under consideration. We shall see later that for the field intensities under consideration $|\vec{P}^{(3)}| \ll |\vec{P}^{(1)}|$ is already justified, thus in the expansion (2.2a) we neglect terms of higher order than three.

The linear polarization $\widehat{\vec{P}}^{(1)}$ can be further simplified. In isotropic media the tensor $\overleftrightarrow{\chi}^{(1)}$ is diagonal and only a single independent element remains: $\chi^{(1)}_{\mu\alpha} = \chi^{(1)}_{xx}\delta_{\mu\alpha}$. Hence, with the convention $\chi^{(1)}(\vec{r},\omega) = \chi^{(1)}_{xx}(\vec{r},-\omega;\omega)$, we have

$$\widehat{\vec{P}}^{(1)}(\vec{r},\omega) = \epsilon_0\chi^{(1)}(\vec{r},\omega)\widehat{\vec{E}}(\vec{r},\omega), \tag{2.6}$$

and we define the scalar dielectric function

$$\epsilon(\vec{r},\omega) = 1 + \chi^{(1)}(\vec{r},\omega). \tag{2.7}$$

The third order nonlinear polarization $\widehat{\vec{P}}^{(3)}$ is determined by the 81 components of the general fourth-rank tensor $\overleftrightarrow{\chi}^{(3)}$. Again we benefit from the isotropy of the medium and from spatial symmetry relations [35] it is possible to show

$$\chi^{(3)}_{\mu\alpha_1\alpha_2\alpha_3} = \chi^{(3)}_{xxyy}\delta_{\mu\alpha_1}\delta_{\alpha_2\alpha_3} + \chi^{(3)}_{xyyx}\delta_{\mu\alpha_3}\delta_{\alpha_1\alpha_2} + \chi^{(3)}_{xyxy}\delta_{\mu\alpha_2}\delta_{\alpha_1\alpha_3}. \tag{2.8}$$

Moreover, we consider media with homogeneous nonlinearity and quasi linearly polarized electric fields $\vec{E} = E_x\vec{e}_x$ only. Therefore, only one relevant component of the tensor remains and with the definition $\chi^{(3)} = \chi^{(3)}_{xxxx} = \chi^{(3)}_{xxyy} + \chi^{(3)}_{xyyx} + \chi^{(3)}_{xyxy}$ we have

$$\begin{aligned}\widehat{\vec{P}}^{(3)}(\vec{r},\omega) &= \vec{e}_x\epsilon_0 \iint \chi^{(3)}(\omega;\omega_1,\omega_2,\omega-\omega_1-\omega_2) \\ &\quad \times \widehat{E}_x(\vec{r},\omega_1)\widehat{E}_x(\vec{r},\omega_2)\widehat{E}_x(\vec{r},\omega-\omega_1-\omega_2)d\omega_1 d\omega_2.\end{aligned} \tag{2.9}$$

As expected, in an isotropic medium the nonlinear polarization vector is parallel to the electric field.

2.1. Beam propagation in a weak-guiding nonlinear optical waveguide

Our aim is a simple but accurate propagation equation for monochromatic beams in a nonlinear waveguide. A small linear index contrast and small nonlinear induced index changes allow us to derive a scalar first order equation without loosing generality. The techniques applied are carefully discussed, also in order to have them ready to hand in the more involved Section 2.2.

For our waveguide, $\epsilon(\vec{r},\omega)$ is assumed real and positive, and we define the linear refractive index $n(\vec{r},\omega) = \sqrt{\epsilon(\vec{r},\omega)}$. Moreover, the index is invariant along propagation direction (z), and we can define a background index as $\lim_{x,y\to\infty} n(x,y,\omega) = n_b(\omega)$. We consider a weakly-guiding waveguide, because we are interested in spatial dynamics. Hence, the relative index change $(n-n_b)/n_b \ll 1$ should be small, and nonlinear effects can influence the guiding properties. Note that this is a different setup to a strong-guiding waveguide, where the spatial behavior is completely determined by the waveguide modes.

Because we are interested in beam propagation only, we consider a quasi linear polarized incident electric field $\vec{E} = E_x\vec{e}_x$ oscillating with the operating frequency ω_0. The complex slowly varying envelope function $\vec{\mathcal{E}}$ of the electric field $\vec{E}$ is defined by

$$\vec{E}(\vec{r},t) = \sqrt{\frac{\omega_0\mu_0}{2k_0}}\vec{\mathcal{E}}(x,y,z)e^{i(k_0 z-\omega_0 t)} + \text{c.c.}, \tag{2.10}$$

where $k_0 = \omega_0 n_b(\omega_0)/c$ is the wavenumber of a plane wave $\sim \exp(ik_0 z - i\omega_0 t)$ propagating in the background medium. The x-component of the optical field is dominant

$$|\mathcal{E}_x| \gg |\mathcal{E}_{y,z}|, \tag{2.11}$$

and we write $\mathcal{E} = \mathcal{E}_x$. For technical convenience, the scalar optical field is normalized such that the intensity is $I = |\mathcal{E}|^2$. The field envelope $\mathcal{E}$ is assumed to change slowly in the variables x, y and z, which is called the paraxial slowly varying envelope approximation (SVEA). More precisely, the envelope has to obey the condition

$$\left|\frac{\partial}{\partial \alpha}\mathcal{E}\right| \ll k_0 |\mathcal{E}|, \tag{2.12}$$

where α is x, y, or z. Physically, Equation (2.12) means that the field envelope $\mathcal{E}$ does not change on length scales comparable to the wavelength $\lambda = 2\pi/k_0$ in the medium.

The Ansatz (2.10) allows us to simplify the expression for the nonlinear polarization. With Equation (2.9) we see

$$\begin{aligned}\vec{P}^{(3)}(\vec{r},t) \;=\;& \epsilon_0 \left(\frac{\omega_0\mu_0}{2k_0}\right)^{\frac{3}{2}} \left[3\chi^{(3)}(-\omega_0;\omega_0,-\omega_0,\omega_0)\,|\mathcal{E}|^2\,\vec{\mathcal{E}} e^{i(k_0 z-\omega_0 t)} + \text{c.c.}\right] \\ &+\epsilon_0 \left(\frac{\omega_0\mu_0}{2k_0}\right)^{\frac{3}{2}} \left[\chi^{(3)}(-3\omega_0;\omega_0,\omega_0,\omega_0)\left(\vec{\mathcal{E}}\cdot\vec{\mathcal{E}}\right)\vec{\mathcal{E}} e^{i(3k_0 z-3\omega_0 t)} + \text{c.c.}\right].\end{aligned} \tag{2.13}$$

It is obvious that the terms in the second line are oscillating with a different frequency, namely the third harmonic $3\omega_0$. If these terms were taken into account, we should also introduce an electric field running at $3\omega_0$. In general these fields remain weak because a plane wave at $3\omega_0$ has a different wave number than $3k_0$. The so-called phase mismatch $\Delta k = 3k_0 - 3\omega_0 n_b(3\omega_0)/c$ leads to destructive interference after a propagation length $\Delta z \sim \pi/\Delta k$. This phase mismatch justifies the disregard of third harmonic generation (THG). Hence, with the definition of the nonlinear refractive index

$$n_2(\omega_0) = \frac{3}{4}\frac{\chi^{(3)}(-\omega_0;\omega_0,-\omega_0,\omega_0)}{\epsilon_0 c n_b^2(\omega_0)}, \tag{2.14}$$

the final expression for the nonlinear polarization vector $\vec{P}^{(3)}$ in our waveguide is

$$\vec{P}^{(3)}(\vec{r},t) = \epsilon_0 \sqrt{\frac{\omega_0\mu_0}{2k_0}} \left[2n_b n_2 |\mathcal{E}|^2\,\vec{\mathcal{E}} e^{i(k_0 z-\omega_0 t)} + \text{c.c.}\right]. \tag{2.15}$$

For n_2 real, this is a so called Kerr nonlinearity. Because we have only one frequency ω_0, frequency arguments will be omitted in what follows.

To sum up, we are looking for a solution of the Equations (2.1) in the nonlinear waveguide, which is close to a linear polarized plane wave propagating in z direction as suggested by the ansatz (2.10). Because there are no free charge carriers in the medium, we have $\vec{J} = 0$ and $\rho = 0$. Equation (2.1a) then reads

$$\nabla \cdot \vec{E} = -\frac{\epsilon_0 \vec{E} \cdot \nabla \epsilon + \nabla \cdot \vec{P}^{(3)}}{\epsilon_0 \epsilon} = -\frac{2n\vec{E} \cdot \nabla n + 2n_b n_2 I \nabla \cdot \vec{E} + 2n_b n_2 \vec{E} \cdot \nabla I}{n^2}. \tag{2.16}$$

Later, when the wave equation will be derived, $\nabla \cdot \vec{E}$ will be neglected because it turns out to be small compared to $\partial_x E_x$, the three derivatives balance and make $\nabla \cdot \vec{E}$ close to zero. To show this crucial relation, we need that $|n - n_b| \ll n_b$ and $|n_2 I| \ll n_b$, which will be verified when we specify the values for the physical parameters. It is obvious that we have to estimate two terms, $\vec{E} \cdot \nabla n$ and $n_2 \vec{E} \cdot \nabla I$. Because of the assumed quasi linear polarization [Equation (2.11)], it is sufficient to deal with $E_x \partial_x n$ and $n_2 E_x \partial_x |\mathcal{E}|^2$. For the second term, it is easy to see that

$$\left| n_2 \vec{E} \cdot \nabla I \right| = \left| n_2 E_x \frac{\partial}{\partial x} |\mathcal{E}|^2 \right| \leq 4 \left| n_2 I \right| \left| \frac{\partial}{\partial x} E_x \right| \ll n_b \left| \frac{\partial}{\partial x} E_x \right|. \tag{2.17}$$

For the first term, we use that the relative index changes ($\ll 1$) are small compared to the relative changes of the field (~ 1), and therefore

$$\left| \vec{E} \cdot \nabla n \right| = \left| E_x \frac{\partial}{\partial x} n \right| \ll n \left| \frac{\partial}{\partial x} E_x \right|. \tag{2.18}$$

Of course, this relation may not be strictly valid in certain domains, especially for extremal values of E_x. But these violations are not due to a large left hand side, rather than to a abnormal small right hand side of Equation (2.18). In particular, $\nabla \cdot \vec{E}$ is not especially large in these domains. Therefore, it is justified to assume

$$\nabla \cdot \vec{E} = 0 \tag{2.19}$$

in the following. Before we continue deriving the wave equation, it might be helpful to reflect the link between SVEA and the vanishing of $\nabla \cdot \vec{E}$, which reads

$$\nabla \cdot \vec{E} = \sqrt{\frac{\omega_0 \mu_0}{2k_0}} e^{i(k_0 z - \omega_0 t)} \left(\frac{\partial}{\partial x} \mathcal{E} + \frac{\partial}{\partial y} \mathcal{E}_y + \frac{\partial}{\partial z} \mathcal{E}_z + i k_0 \mathcal{E}_z \right) + \text{c.c.}. \tag{2.20}$$

Because of the assumed quasi linear polarization [Equation (2.11)] we can neglect $\partial_y \mathcal{E}_y$ and $\partial_z \mathcal{E}_z$, and Equation (2.19) implies that $\mathcal{E}_z \approx i \partial_x \mathcal{E} / k_0$. We see that SVEA ($|\partial_x \mathcal{E}| \ll k_0 |\mathcal{E}|$) is crucial here to raise $k_0 \mathcal{E}_z$ in the same order of magnitude as $\partial_x \mathcal{E}$.

With Equations (2.3), (2.19) and $\vec{J} = 0$ Maxwell's equations lead to the wave equation

$$\Delta \vec{E} - \frac{1}{c^2}\frac{\partial^2}{\partial t^2}\vec{E} = \mu_0 \frac{\partial^2}{\partial t^2}\vec{P}. \tag{2.21}$$

Using Equations (2.6), (2.7), (2.10) and (2.15) the wave equation reads

$$\frac{\partial}{\partial z}\left(2ik_0\mathcal{E} + \frac{\partial}{\partial z}\mathcal{E}\right) + \Delta_\perp \mathcal{E} + \frac{\omega_0^2}{c^2}(n+n_b)(n-n_b)\mathcal{E} + 2k_0\frac{\omega_0}{c}n_2\left|\mathcal{E}\right|^2\mathcal{E} = 0, \tag{2.22}$$

where $\Delta_\perp = \partial_x^2 + \partial_y^2$. The SVEA condition (2.12) and $|n - n_b| \ll n_b$ allow us to derive the final propagation equation

$$i\frac{\partial}{\partial z}\mathcal{E}(\vec{r}) + \frac{1}{2k_0}\triangle_\perp \mathcal{E}(\vec{r}) + \frac{\omega_0}{c}n_2\left|\mathcal{E}(\vec{r})\right|^2\mathcal{E}(\vec{r}) + \frac{\omega_0}{c}\left(n(x,y) - n_b\right)\mathcal{E}(\vec{r}) = 0. \tag{2.23}$$

Equation (2.23) describes the propagation of the field envelope $\mathcal{E}$ in a weak-guiding optical waveguide with a Kerr nonlinearity in the scalar, slowly varying envelope approximation. Typical values for the parameters in a silica bulk medium are $n_b = 1.4$, $|n - n_b| \leq 5 \times 10^{-3}$, $n_2 = 3 \times 10^{-16}$ cm^2/W at a vacuum wavelength $\lambda_0 = 600$ nm. The damage threshold for silica is about 10 J/cm^2 for nanosecond pulses [36] corresponding to $\sim 10^{10}$ W/cm^2, up to which the model should be valid. For shorter, femtosecond pulses this damage threshold is 1000 times higher, but since we treat cw beams the lower value for nanosecond pulses is relevant. Mathematically, Equation (2.23) is a (2D+1)-dimensional nonlinear Schrödinger equation with additional potential.

2.2. Femtosecond pulsed beam propagation in air

In contrast to the previous section, where we consider spatial dynamics in an inhomogeneous medium, we here treat a spatio-temporal problem, but in a homogeneous medium. Hence, we will have a third "transverse" dimension in our final propagation equation, namely the time. Moreover, intensities exceeding the ionization threshold of the medium (air) lead to the generation of free carriers and therefore a current density $\vec{J} \neq 0$. Thus, a second equation, describing the evolution of the carrier density, will be derived. However, even though more complicated physics than in the previous section is involved, we will follow the same procedure and derive a scalar first order NLS-type propagation equation for the optical field.

In air, $\epsilon(\omega)$ is real and positive for wavelengths ranging from the infrared to the ultraviolet. The linear refractive index is defined by $n(\omega) = \sqrt{\epsilon(\omega)}$ and the wavenumber by $k(\omega) = \omega n(\omega)/c$. We are interested in the propagation of a quasi linear polarized pulsed beam, whose spectrum is centered around the operating frequency ω_0. Assuming a sufficiently small spectral bandwidth $\Delta\omega$, we can expand $k(\omega)$ in a Taylor series around ω_0

$$\begin{aligned} k(\omega) &= k_0 + k'\overline{\omega} + \frac{1}{2}k''\overline{\omega}^2 + \frac{1}{6}k'''\overline{\omega}^3 + \dots & \text{(2.24a)} \\ k^2(\omega) &= k_0^2 + 2k_0k'\overline{\omega} + k'^2\overline{\omega}^2 + k_0k''\overline{\omega}^2 + k'k''\overline{\omega}^3 + \frac{1}{3}k_0k'''\overline{\omega}^3 + \dots, & \text{(2.24b)} \end{aligned}$$

where $\overline{\omega} = \omega - \omega_0$. The complex slowly varying envelope function $\vec{\mathcal{E}}$ of the electric field $\vec{E}$ is defined by

$$\vec{E}(\vec{r},t) = \sqrt{\frac{\omega_0\mu_0}{2k_0}}\vec{\mathcal{E}}(x,y,z,t)e^{i(k_0z-\omega_0t)} + \text{c.c.}, \tag{2.25}$$

analogous to Equation (2.10), but here the envelope is time dependent. As for the waveguide, the x-component of the optical field is assumed to be the dominant one, $|\mathcal{E}_x| \gg |\mathcal{E}_{y,z}|$, and we write $\mathcal{E} = \mathcal{E}_x$. The field envelope $\mathcal{E}$ is assumed to change slowly in $\alpha = x$, y, z and t

$$\begin{aligned} \left|\frac{\partial}{\partial\alpha}\mathcal{E}\right| &\ll k_0\,|\mathcal{E}| & \text{(2.26a)} \\ \left|\frac{\partial}{\partial t}\mathcal{E}\right| &\ll \omega_0\,|\mathcal{E}|\,. & \text{(2.26b)} \end{aligned}$$

This is justified if the field envelope $\mathcal{E}$ does not change on length scales comparable to the wavelength $\lambda = 2\pi/k_0$ and time scales comparable to the optical cycle $T_{cyc} = 2\pi/\omega_0$.

Strictly speaking, the computation of the third order nonlinear polarization vector $\vec{P}^{(3)}$ for pulses requires the knowledge of the frequency dependencies of the nonlinear susceptibility over the relevant part of the spectrum [see Equation (2.9)]. However, this is far beyond the scope of this work, since we are interested in a simpler model for understanding the physical basics. Here, we will use a common approximation to describe the propagation of infrared femtosecond pulses in air [34, 37], reading

$$\begin{aligned} \vec{P}^{(3)}(\vec{r},t) &= \epsilon_0\sqrt{\frac{\omega_0\mu_0}{2k_0}}\left[2n_bn_2\int\mathcal{R}(t-t')\,|\mathcal{E}(t')|^2\,dt'\vec{\mathcal{E}}e^{i(k_0z-\omega_0t)} + \text{c.c.}\right] & \text{(2.27a)} \\ \mathcal{R}(t) &= (1-x_{dK})\,\delta(t) + x_{dK}\frac{1+\Omega^2\tau_K^2}{\Omega\tau_K^2}\Theta(t)e^{-\frac{t}{\tau_K}}\sin(\Omega t), & \text{(2.27b)} \end{aligned}$$

where δ denotes the δ-distribution and Θ the Heavyside function (the unit of $\delta(t)$ is s^{-1}, for definitions see Appendix C). The above intensity dependent nonlinear polarization accounts for non-resonant and incoherent nonlinear effects. As in the previous section, we neglect third harmonic generation due to the large phase mismatch $\Delta k = 3k_0 - k(3\omega_0)$ (e.g. $\Delta k = -5$ cm^{-1} @ 800 nm). The Kerr response of air $\mathcal{R}(t)$ possesses both retarded and instantaneous components at the ratio of x_{dK}. The instantaneous part $\sim \delta(t)$ describes the response from the bound electrons. Electronic response times are about a few femtosecond or less, and therefore considerably smaller than the duration of the pulse envelopes under consideration. The retarded part $\sim \exp(-t/\tau_K)$ accounts for nuclear response, namely the rotational Raman contribution. The delay time τ_K and the inverse resonance frequency $1/\Omega$ lie in the same range as the accounted pulse lengths ~ 100 fs.

As mentioned before, high intensities require the modeling of both ionization of air molecules and feedback of the generated charge carriers to the laser field. Of all molecular species in the atmosphere the oxygen molecule has the lowest ionization potential $U_i = 12.1$ eV. Oxygen, contributing $\sim 20\%$ to the neutral molecule density, is already the key-player of the infrared ionization processes in air. Other possible scenarios, e.g. the ionization of nitrogen, can be neglected [33]. From simple energy considerations we can deduce the number of photons $K = \mathrm{mod}(U_i/\hbar\omega_0) + 1$ that are necessary for this multiphoton ionization (MPI) process. Here we assume a single photon energy $\sim \hbar\omega_0$ for all photons involved, because around the center frequency ω_0 we have the highest spectral intensity. The Keldysh theory delivers a MPI ionization rate

$$\mathcal{W}_{MPI} = \sigma_K I^K = \sigma_K \left|\mathcal{E}\right|^{2K}, \tag{2.28}$$

which is valid up to intensities of $\sim 10^{13}$ W/cm^2. For higher intensities, tunnel ionization starts to contribute [38, 39]. Femtosecond pulsed beams in air reach peak intensities of about $\sim 10^{14}$ W/cm^2, which is beyond the validity of the MPI limit. However, considerable ionization takes place in the range $10^{13} - 10^{14}$ W/cm^2 only. In this range it is possible to infer a MPI-like formulation from the more general Perelomov-Popov-Terent'ev theory [40] by adjusting σ_K properly.

Later we will see that we have to take into account a second ionization mechanism for oxygen, the avalanche ionization by free electrons accelerated by the laser field. This mechanism is much weaker than MPI, and is only included for consistency. The equation for the evolution of the electron density ρ_e reads

$$\frac{\partial}{\partial t}\rho_e(\vec{r}, t) = \left(\mathcal{W}_{MPI} + \mathcal{W}_{AI}\right)\rho_{nt}, \tag{2.29}$$

where $\mathcal{W}_{AI}$ is the avalanche ionization rate, and ρ_{nt} is the neutral molecule density of oxygen. Here we neglect both diffusion and recombination of carriers, because these processes are acting on time scales $\geq$ 10 ps. Hence, they are too slow to influence femtosecond pulses. Moreover, expected electron densities $\rho_e \leq 10^{16}$ cm^{-3} justify the assumption of a constant neutral density $\rho_{nt} = 5.4 \times 10^{18}$ cm^{-3} at atmospheric pressure. It is worth noticing that the electron density ρ_e is also a slowly varying entity, like $\mathcal{E}$. It does not take into account the fast small-scale motion ($\sim$ 1 nm) of the electrons.

Such fast small-scale motions, namely oscillations of the free electrons driven by the electric field, are included by a Drude model. We assume a free electron gas on a positive background. This background are the ions, which provide the shielding of the electron charges. Because the mass of the ions is $\sim$ 30000 times the electron mass, we neglect ion motions and therefore their contribution to the current density. Then the free electron current density $\vec{J}_e(\vec{r}, t)$ is governed by

$$\frac{\partial}{\partial t}\vec{J}_e + \frac{1}{\tau_0}\vec{J}_e = \frac{q_e^2}{m_e}\rho_e\vec{E}, \tag{2.30}$$

where we neglect diffusion. Here $q_e = 1.6 \times 10^{-19}$ C accounts for the electron charge, $\tau_0 = 3.5 \times 10^{-13}$ s is the electron collision time and $m_e = 9.1 \times 10^{-31}$ kg the electron mass. The motion of the free electrons is dominated by the fast oscillations of the linear polarized optical field at ω_0, and it is justified to introduce a complex slowly varying envelope $\vec{\mathcal{J}}_e$,

$$\vec{J}_e(\vec{r}, t) = \sqrt{\frac{\omega_0\mu_0}{2k_0}}\vec{\mathcal{J}}_e(x, y, z, t)e^{i(k_0 z - \omega_0 t)} + \text{c.c.}, \tag{2.31}$$

analogous to Equation (2.25). We can solve Equation (2.30) formally as

$$\vec{\mathcal{J}}_e = \frac{q_e^2}{m_e\omega_0}\left(-i\hat{T} + \frac{1}{\tau_0\omega_0}\right)^{-1}\rho_e\vec{\mathcal{E}}, \tag{2.32}$$

where $\hat{T} = 1 + i\partial_t/\omega_0$. A SVEA condition like (2.26b) can be formulated for ρ_e as well as for $\vec{\mathcal{J}}_e$ and reads $|\partial_t\rho_e\vec{\mathcal{E}}|/\omega_0 \ll |\rho_e\vec{\mathcal{E}}|$. Thus, together with $1/\tau_0\omega_0 \ll 1$ it is justified to simplify Equation (2.32) to

$$\vec{\mathcal{J}}_e = \frac{q_e^2}{m_e\omega_0}\left(\frac{1}{\tau_0\omega_0} + i\hat{T}^{-1}\right)\rho_e\vec{\mathcal{E}}, \tag{2.33}$$

which is much more convenient in the following derivation.

As in the case of the ionization rates, we have to consider a second contribution to the current density: The generation of free carriers by MPI. Because this term will lead to the expression for the multiphoton absorption (MPA) in our final equations, we call it $\vec{J}_{MPA}$ and

$$\vec{J}(\vec{r},t) = \vec{J}_e(\vec{r},t) + \vec{J}_{MPA}(\vec{r},t). \tag{2.34}$$

The corresponding complex slowly varying envelopes $\vec{\mathcal{J}}$ and $\vec{\mathcal{J}}_{MPA}$ are defined as the analogues of $\vec{\mathcal{J}}_e$ [Equation (2.31)].

Via the energy conservation law it is possible to derive self-consistent expressions for $\mathcal{W}_{AI}$ and $\vec{J}_{MPA}$. The temporal evolution of the local energy density w in the medium is determined by

$$\frac{d}{dt} w(\vec{r},t) = \vec{J}(\vec{r},t) \cdot \vec{E}(\vec{r},t). \tag{2.35}$$

Hence, we can compute the energy transferred to the medium by the pulse at the position $\vec{r}$ in a small volume $\Delta V = \lambda_0^3$ by

$$\begin{aligned} W_{\Delta V}(\vec{r}) &= \int_0^{\lambda_0}\int_0^{\lambda_0}\int_0^{\lambda_0}\int_{-\infty}^{\infty} \vec{J}(\vec{r}+\vec{r}',t)\cdot\vec{E}(\vec{r}+\vec{r}',t)dtd^3r' \qquad (2.36)\\ &= \lambda_0^3 \int \frac{\mu_0 q_e^2}{m_e\tau_0\omega_0 k_0}\rho_e(\vec{r},t)\left|\mathcal{E}(\vec{r},t)\right|^2 + \frac{\omega_0\mu_0}{2k_0}\left[\vec{\mathcal{J}}_{MPA}(\vec{r},t)\cdot\vec{\mathcal{E}}^*(\vec{r},t) + \text{c.c.}\right] dt. \end{aligned}$$

Note that terms containing iT^{-1} cancel via integration by parts, and that fast oscillating terms proportional to $\exp[\pm i2(k_0 z - \omega_0 t)]$ do not contribute to the integral. Moreover, the choice of ΔV is arbitrary, its dimensions just have to be large against the scales of the electron movement and small compared to length scales of the slowly varying envelopes.

On the other hand, we know that energy transferred to the medium by the optical field causes ionization of neutral oxygen molecules. Here we assume that all energy losses due to electron-ion collision [term $\sim 1/\tau_0$ in Equation (2.30)] contribute to the avalanche ionization. This is justified by the fact that the kinetic energy of the free electrons can reach up to ~ 20 eV, which is sufficient for a ballistic ionization process. Hence we have

$$W_{\Delta V}(\vec{r}) = \lambda_0^3 \int \left[\sigma_K \left|\mathcal{E}(\vec{r},t)\right|^{2K} \rho_{nt}(\vec{r},t) K\hbar\omega_0 + \mathcal{W}_{AI}(\vec{r},t)\rho_{nt}(\vec{r},t)U_i\right] dt. \tag{2.37}$$

The first term on the right-hand-side gives the energy consumption of MPI (one process needs $K\hbar\omega_0$ in energy), the second term the energy consumption of avalanche ionization (consumes U_i). In terms of SVEA, the energy transfer is local and instantaneous. Both ionization processes act on time scales comparable to the oscillation of the carrier wave or less, and the motion of the free electrons takes place on nanometer scales. Therefore, it is justified to omit the time integral when we equate the expressions of Equations (2.36) and (2.37):

$$\frac{\mu_0 q_e^2}{m_e \tau_0 \omega_0 k_0} \rho_e \left|\mathcal{E}\right|^2 + \frac{\omega_0 \mu_0}{k_0} \Re\Big(\vec{\mathcal{J}}_{MPA} \cdot \vec{\mathcal{E}}^*\Big) = \sigma_K \left|\mathcal{E}\right|^{2K} \rho_{nt} K \hbar \omega_0 + \mathcal{W}_{AI} \rho_{nt} U_i. \tag{2.38}$$

We claimed above that we can derive $\mathcal{W}_{AI}$ and $\vec{J}_{MPA}$ self-consistently. Indeed, Equation (2.38) links both $\mathcal{W}_{AI}$ and $\vec{J}_{MPA}$ to known quantities. However, additional arguments are necessary to make them unique. First, we assume that $\vec{J}_{MPA}$ causes energy losses only, e.g., $|\Im(\vec{\mathcal{J}}_{MPA} \cdot \vec{\mathcal{E}}^*)| = 0$. This is a rather formal constraint, because there is no physical argument that MPA should influence the optical field other than by losses. Second, we assume that the current density $\vec{J}_{MPA}$ is caused by MPI only, and that $\vec{J}_{MPA}$ is parallel to $\vec{E}$. On these assumptions Equation (2.38) leads to

$$\vec{\mathcal{J}}_{MPA} = \frac{k_0 \beta^{(K)}}{\omega_0 \mu_0} \left|\mathcal{E}\right|^{2(K-1)} \vec{\mathcal{E}}, \tag{2.39}$$

where $\beta^{(K)} = \sigma_K K \hbar \omega_0 \rho_{nt}$, and

$$\mathcal{W}_{AI} = \frac{\sigma}{U_i \rho_{nt}} \rho_e \left|\mathcal{E}\right|^2, \tag{2.40}$$

where $\sigma = \mu_0 q_e^2 / m_e \tau_0 \omega_0 k_0$. Thus, we have derived self-consistent expressions for $\mathcal{W}_{AI}$ and $\vec{J}_{MPA}$.

We proceed as in the previous section and justify that we can neglect $\nabla \cdot \vec{E}$ in the derivation of the wave equation. In particular, Equation (2.1a) reads

$$\nabla \cdot \vec{E} = \frac{\rho - \nabla \cdot \vec{P}^{(3)}}{\epsilon_0 \epsilon}, \tag{2.41}$$

and we want to show that $|\nabla \cdot \vec{E}| \ll |\partial_x E_x|$. Despite of the more complicated expression, the magnitude of the nonlinear polarization is still $\sim |n_2 I|$, and we will see later that $|n_2 I| \ll n_b = n(\omega_0)$. Therefore we have $|\nabla \cdot \vec{P}^{(3)}|/\epsilon_0\epsilon \ll |\partial_x E_x|$ analogous to the previous case. What is new here is the term $\rho/\epsilon_0\epsilon$. The carrier density $\rho = q_e(\rho_{ion} - \rho_e)$ contains both the contributions from the free electrons and the ions. In the current density $\vec{J}$ it is justified to neglect the contribution of the ions because of their huge mass compared to the electrons. The continuity equation

$$\frac{\partial}{\partial t}\rho + \nabla \cdot \vec{J} = 0, \tag{2.42}$$

can be derived straight forward from Maxwell's equations. We use it to substitute ρ

in Equation (2.41) and get

$$\left(\frac{\partial}{\partial t} - i\omega_0\right) \nabla \cdot \left[\vec{\mathcal{E}} e^{ik_0 z}\right] = -\frac{\nabla \cdot \left[\vec{\mathcal{J}} e^{ik_0 z}\right]}{\epsilon_0 \epsilon} \tag{2.43}$$

for the complex envelopes. Now we plug in the expressions for $\vec{\mathcal{J}}_e$ and $\vec{\mathcal{J}}_{MPA}$ and get

$$\nabla \cdot \left[\vec{\mathcal{E}} e^{ik_0 z}\right] = \hat{T}^{-1} \nabla \cdot \left(\hat{T}^{-1} \frac{\rho_e}{n_b^2 \rho_c} \vec{\mathcal{E}} e^{ik_0 z} - i\frac{\sigma \rho_e}{k_0} \vec{\mathcal{E}} e^{ik_0 z} - i\frac{\beta^{(K)} \left|\mathcal{E}\right|^{2(K-1)}}{k_0} \vec{\mathcal{E}} e^{ik_0 z}\right), \tag{2.44}$$

where $\rho_c = m_e \epsilon_0 \omega_0^2 / \, q_e^2$ is the critical plasma density. First of all, we can drop the operator $\hat{T}$, since the SVEA condition (2.26b) guarantees $\hat{T} = 1 + i\partial_t/\omega_0 \sim \hat{\mathbb{I}}$. Moreover, it turns out that $\rho_e/\rho_c \ll n_b^2$, $\sigma \rho_e \ll k_0$ and $\beta^{(K)} |\mathcal{E}|^{2(K-1)} \ll k_0$ (see end of this section). Therefore, we are left with the tasks to show $|\mathcal{E} \partial_x \rho_e| \sim \rho_e |\partial_x \mathcal{E}|$ and $|\mathcal{E} \partial_x |\mathcal{E}|^{2(K-1)}| \sim |\mathcal{E}|^{2(K-1)} |\partial_x \mathcal{E}|$. For the first task, we can conclude using Equations (2.28) and (2.29) that

$$\left|\mathcal{E} \frac{\partial}{\partial x} \rho_e\right| \sim 2K \left|\rho_e \frac{\partial}{\partial x} \mathcal{E}\right|, \tag{2.45}$$

where we neglect avalanche ionization. For the second task, it is easy to see that

$$\left|\mathcal{E} \frac{\partial}{\partial x} \left|\mathcal{E}\right|^{2(K-1)}\right| \leq 2\left(K-1\right) \left|\mathcal{E}\right|^{2(K-1)} \left|\frac{\partial}{\partial x} \mathcal{E}\right|. \tag{2.46}$$

Hence, as in the previous section, $\nabla \cdot \vec{E} = 0$ is justified and we are able to derive the wave equation

$$\Delta \vec{E} - \frac{1}{c^2} \frac{\partial^2}{\partial t^2} \vec{E} = \mu_0 \left(\frac{\partial^2}{\partial t^2} \vec{P} + \frac{\partial}{\partial t} \vec{J}\right). \tag{2.47}$$

If we plug in the SVEA ansatz and the expressions for polarization [Equations (2.2a), (2.6), and (2.27)] and current density [Equations (2.33), (2.34), and (2.39)] derived above we get

$$\begin{aligned}
&\left(\frac{\partial}{\partial z} + ik_0\right)^2 \mathcal{E} + \Delta_\perp \mathcal{E} + \int k^2(\omega_0 + \varpi) \widehat{\mathcal{E}}(\vec{r}, \varpi) e^{-i\varpi t} d\varpi \qquad (2.48)\\
= \;& -\frac{2k_0^2 n_2}{n_b} \hat{T}^2 \int \mathcal{R}(t-t') \left|\mathcal{E}(t')\right|^2 dt' \mathcal{E} + \frac{k_0^2}{n_b^2 \rho_c} \rho_e \mathcal{E} - ik_0 \hat{T} \left(\sigma \rho_e \mathcal{E} + \beta^{(K)} \left|\mathcal{E}\right|^{2(K-1)} \mathcal{E}\right),
\end{aligned}$$

where $\widehat{\mathcal{E}}$ denotes the Fourier transform of $\mathcal{E}$.

Our goal is to model the evolution of short laser pulses propagating in air. These pulses are traveling at a certain velocity in z-direction. In the linear regime, they travel at the group velocity $v_g(\omega_0) = 1/k'$, and it is a good assumption that the nonlinear effects under consideration will not change this too much. Hence, the derivation of the field envelope $\mathcal{E}$ with respect to z is dominated by the motion of the pulse, and we have

$$\left|\frac{\partial}{\partial z}\mathcal{E}+k'\frac{\partial}{\partial t}\mathcal{E}\right| \ll \left|\frac{\partial}{\partial z}\mathcal{E}\right|. \tag{2.49}$$

Hence, with the transformation into coordinates moving with the pulse, $\tilde{t}=t-k'z$ and $\tilde{z}=z$, it is possible to achieve an even weaker dependency of the field envelope on the propagation variable: With Equations (2.26) and (2.49) we see

$$\left|\frac{\partial}{\partial \tilde{z}}\mathcal{E}\right| = \left|\partial_z\mathcal{E}+k'\partial_t\mathcal{E}\right| \ll \left|\frac{\partial}{\partial z}\mathcal{E}\right| \ll k_0\left|\mathcal{E}\right|. \tag{2.50}$$

For simplicity, we will remove the tilde $\sim$ after applying the transformation and with Equation (2.24b) we get

$$\begin{aligned}
&\frac{\partial}{\partial z}\left(1+i\frac{k'}{k_0}\frac{\partial}{\partial t}-\frac{i}{2k_0}\frac{\partial}{\partial z}\right)\mathcal{E}-\frac{i\Delta_\perp\mathcal{E}}{2k_0}+\frac{ik''}{2}\left(1+i\frac{k'}{k_0}\frac{\partial}{\partial t}+\frac{i}{3}\frac{k'''}{k''}\frac{\partial}{\partial t}\right)\frac{\partial^2\mathcal{E}}{\partial t^2} \\
= \; &\frac{ik_0n_2}{n_b}\hat{T}^2\int\mathcal{R}(t-t')\left|\mathcal{E}(t')\right|^2dt'\mathcal{E}-\frac{ik_0}{2n_b^2\rho_c}\rho_e\mathcal{E}-\frac{1}{2}\hat{T}\left(\sigma\rho_e\mathcal{E}+\beta^{(K)}\left|\mathcal{E}\right|^{2(K-1)}\mathcal{E}\right).
\end{aligned} \tag{2.51}$$

In air, it is justified to assume $k'=1/c$, $n_b=1$ and therefore $1+ik'\partial_t/k_0=\hat{T}$. With Relation (2.50) we neglect the second derivative with respect to z, and after multiplying with the inverse operator $\hat{T}^{-1}$ the ultimate propagation equation reads

$$\begin{aligned}
&\frac{\partial}{\partial z}\mathcal{E}-\frac{i}{2k_0}\hat{T}^{-1}\Delta_\perp\mathcal{E}+i\frac{k''}{2}\frac{\partial^2}{\partial t^2}\mathcal{E}-\frac{k'''}{6}\frac{\partial^3}{\partial t^3}\mathcal{E} \\
= \; &ik_0n_2\hat{T}\int\mathcal{R}(t-t')\left|\mathcal{E}(t')\right|^2dt'\mathcal{E}-i\frac{k_0}{2\rho_c}\hat{T}^{-1}\rho_e\mathcal{E}-\frac{\sigma}{2}\rho_e\mathcal{E}-\frac{\beta^{(K)}}{2}|\mathcal{E}|^{2K-2}\mathcal{E},
\end{aligned} \tag{2.52}$$

where we consequently neglect derivations with respect to t of order higher than three. It is interesting to note that Equation (2.52) takes into account all deviations from unity of the order $\left|\partial_t\mathcal{E}\right|/\omega_0$ and therefore goes beyond ordinary SVEA [41].

In this work, emphasis is laid on the spatial dynamics of the pulsed beams. Hence, for sake of simplicity, we assume $k'''=0$ and $\hat{T}=\hat{\mathbb{I}}$. These assumptions are justified by the SVEA condition (2.26b) and $k'''/k''\sim 1/\omega_0$. Moreover, we neglect the $\sin(\Omega t)$ dependency in the Raman response function [Equation (2.27)]. The resulting simplified nonlinear response provides a reasonable and numerically tractable description of the nonlinear polarization of air. This step is motivated from the numerical point of view, in order to save computational efforts. The influence of the oscillation in the response function on the solution is weak [33], but requires to solve a second order differential equation in time in each step instead of a first order one. The resulting equations form the standard model for femtosecond pulse propagation in air [11,22,32–34] [S6,S7]

$$\begin{aligned}
\frac{\partial}{\partial z}\mathcal{E} &= i\frac{1}{2k_0}\Delta_\perp\mathcal{E} - i\frac{k''}{2}\frac{\partial^2}{\partial t^2}\mathcal{E} + ik_0 n_2 \int \mathcal{R}(t-t')\left|\mathcal{E}(t')\right|^2 dt'\mathcal{E} \qquad (2.53a)\\
&\quad -i\frac{k_0}{2\rho_c}\rho_e\mathcal{E} - \frac{\sigma}{2}\rho_e\mathcal{E} - \frac{\beta^{(K)}}{2}|\mathcal{E}|^{2K-2}\mathcal{E},\\
\mathcal{R}(t) &= (1-x_{dK})\,\delta(t) + \frac{x_{dK}}{\tau_K}\Theta(t)e^{-\frac{t}{\tau_K}}, \qquad (2.53b)\\
\frac{\partial}{\partial t}\rho_e &= \sigma_K\rho_{nt}|\mathcal{E}|^{2K} + \frac{\sigma}{U_i}\rho_e|\mathcal{E}|^2. \qquad (2.53c)
\end{aligned}$$

For an operating wavelength $\lambda_0 = 2\pi/k_0 = 800$ nm the pertinent parameters are given in Table 2.1. The peak intensity $|\mathcal{E}|^2$ never exceeds 10^{14} W/cm^2, and $\rho_e \leq 10^{17}$ cm^{-3}. The resulting nonlinear induced index changes $\sim n_2 I$ and $\sim \rho_e/\rho_c$ are in the order of 10^{-4}.

$k_0 = 79 \times 10^3$ cm^{-1}	$k'' = 0.2$ fs^2/cm	$n_2 = 3 \times 10^{-19}$ cm^2/W
$\rho_c = 1.8 \times 10^{21}$ cm^{-3}	$\sigma = 5.4 \times 10^{-20}$ cm^2	$K = 8$
$\beta^{(K=8)} = 3.1 \times 10^{-98}$ cm^{13}/W^7	$x_{dK} = 0.5$	$\tau_K = 70$ fs
$\sigma_{K=8} = 2.9 \times 10^{-99}$ s^{-1} cm^{16}/W^8	$\rho_{nt} = 5.4 \times 10^{18}$ cm^{-3}	$U_i = 12.1$ eV

Table 2.1.: Values of the parameters in Equations (2.53) for $\lambda_0 = 800$ nm.

3. Beams in a nonlinear optical waveguide

The two sections of this chapter deal with the same physical system, namely a weakly-guiding waveguide with a Kerr nonlinearity, but in opposite regimes in terms of the trapping mechanism. In Section 3.1, the trapping is linear due to the waveguide. Nonlinear effects slightly modify the linear modes of the waveguide, which we then call nonlinear bound states. The main focus lies on the analysis of the stability of these nonlinear bound states. Analytical arguments are double-checked by rigorous numerical simulations. Special regard is paid to the decay mechanism of unstable nonlinear bound states. Here we always operate in the low-power regime close to the linear one.

In contrast to that, in Section 3.2 we address highly nonlinear collapsing solutions. In this high-power regime, the beam undergoes nonlinear self-trapping which leads to catastrophic self-focusing and collapse. The linear waveguide acts perturbatively on this nonlinear self-focusing dynamics. We compare this system to the well-known (2D+1)-dimensional NLS equation. By doing so, we are able to transfer classical results to our system, and point out important differences. Finally, we check our analytical arguments by numerical simulations.

For technical convenience, we rescale Equation (2.23) to dimensionless quantities. Moreover, the essential part of the literature on NLS collapse uses this formulation (see e.g. [9, 42]). The transverse coordinates x and y are scaled to the extension of the waveguide r_0. In the case of an optical fiber r_0 is simply the core diameter. For more complicated index distributions, one may choose a typical transverse dimension. Moreover, we normalize the coefficients in front of both the diffraction term and the nonlinearity to unity. With $X = x/r_0$, $Y = y/r_0$, $Z = z/2k_0r_0^2$, and $\sigma = \mathrm{sign}(n_2)$ the modified (2D+1)-dimensional NLS equation for the wave function $\Psi = k_0 r_0 \sqrt{2\,|n_2|\,/n_b}\mathcal{E}$ reads

$$i\frac{\partial}{\partial Z}\Psi + \left(\frac{\partial^2}{\partial X^2} + \frac{\partial^2}{\partial Y^2}\right)\Psi + \sigma\,|\Psi|^2\,\Psi - V\Psi = 0, \tag{3.1}$$

with an bounded potential $V = 2k_0^2 r_0^2 (n_b - n)/n_b$, satisfying $\lim_{R\to\infty} V = 0$.

Another reason for using the dimensionless formulation of Equation (3.1) is the generality of the NLS equation. In particular, it is also known as Gross-Pitaevskii equation, which governs the macroscopic Bose-Einstein condensate (BEC) wave function in the mean-field approximation. Here, the potential models the magnetic trap confining bosons into a condensate. For atoms with attractive interactions, BECs can undergo sequences of collapses [43–45], similar to the self-focusing phenomenon in optics. However, for suitable numbers of particles and/or different interactions, long-living stationary-wave structures as ground states (single-humped) or vortices (with angular momentum; see, e.g., [46]) can form in condensates.

3.1. Stability of weakly nonlinear linearly guided beams

In this section, we present an easy-to-use *sufficient* stability criterion for low-power nonlinear bound states of NLS systems with an "attractive" potential, in optical terms, linearly guided beams undergoing weak nonlinearities. The knowledge of the spectrum of this potential (the linear waveguide modes) is sufficient to determine the stability of the nonlinear bound states in the limit of small powers. Moreover, the theory can be applied in principle to conservative, Hamiltonian systems of arbitrary dimensionality and an arbitrary shaped, but "attractive" potential. However, for the sake of conciseness, we mainly concentrate on the case of a circularly symmetric fiber with focusing or defocusing cubic nonlinearity.

In Section 3.1.1, we determine the linear modes of the potential and their continuation towards nonlinear bound states ("solitons") for higher power levels. In Section 3.1.2, we discuss the stability of these "solitons" for low powers. Here we use the key-property that the linear modes of the potential are related to the eigenfunctions of the linearized NLS operator, which determines the stability of weakly nonlinear waves. More precisely, each of the linear modes appears twice as an eigenfunction, but with shifted eigenvalue. Whereas it is known that the resonance of two linear *localized* eigenfunctions can produce instabilities (see, e.g., Refs [47–49]), the present theory, instead, deals with resonances between *localized* eigenfunctions (discrete eigenvalues) and *delocalized* eigenfunctions (continuous eigenvalues). In Section 3.1.3, we propose a stability criterion for low-power nonlinear bound states, deduced from the existence of the previous resonances. By analyzing the dependency of the perturbation amplitudes on the growth rate, it is shown that the criterion is indeed sufficient for stability. Finally, in Section 3.1.4 our analytical arguments are double-checked by means of a numerical stability analysis and by direct numerical simulations.

Our results can be applied directly to the step-index optical fiber with a focusing Kerr nonlinearity. Guiding high power optical fields through fibers is still a challenging task. Large mode areas have to be used to limit nonlinear effects and to avoid permanent damage. However, this usually implies multi-mode behavior and therefore contradicts the requirement of a well-defined transverse field structure. Our results show that strict single mode behavior is not required and that by tailoring the linear index profile, e.g., an effective potential, a nonlinear destabilization of higher order modes can be achieved. In a numerical example a vortex mode, although linearly guided, decays into the ground state due to the action of the nonlinearity.

3.1.1. Linear modes and nonlinear bound states

In the subsequent analysis, we switch from Cartesian coordinates (X, Y, Z) to cylindrical ones (R, Φ, Z), because we restrict ourselves to radially symmetric waveguides for sake of simplicity. The potential V is assumed to support several localized linear modes $\Theta_{j,M}(R)\exp(iM\Phi + i\gamma_{j,M}Z)$, $M = \ldots, -1, 0, 1, \ldots$, $j = 1, 2, \ldots$, with discrete eigenvalues $\gamma_{j,M}$ ordered as $\gamma_{j_1,M} > \gamma_{j_2,M} \Leftrightarrow j_1 < j_2$. The eigenfunctions $\Theta \equiv \Theta_{j,M}$ obey

$$\begin{aligned} \gamma\Theta &= \hat{D}_M\Theta && (3.2a)\\ \hat{D}_M &= \frac{1}{R}\frac{\partial}{\partial R}\left(R\frac{\partial}{\partial R}\right) - \frac{M^2}{R^2} - V, && (3.2b) \end{aligned}$$

where $|\min V| > \gamma_{j,M} > 0$. For $\gamma = \gamma_c \leq 0$ in Equation (3.2a) we have a continuum of delocalized (radiative) modes $\Theta_{\gamma_c,M}$. Further on, we consider a class of potentials V, for which the discrete spectrum is not degenerated, apart from the trivial degeneration that follows from the elementary symmetry $M \to -M$.

In the following, we use a radially symmetric step-potential $[V(R \leq 1) = -V_0, V(R > 1) = 0]$ as an illustrative example, which models the most common case of an optical fiber. The depth of the potential V_0 determines the number and magnitude of the discrete eigenvalues $\gamma_{j,M}$ and the domain of the continuum. Figure 3.1 shows an example for the discrete (localized modes) and continuous (delocalized modes) eigenvalues of Equation (3.2a). The assumption of a step potential obviously violates the conditions to achieve Equation (2.19): The gradient of the refractive index is infinite at the borders of the fiber core. Nevertheless, it is common to use a step profile as an idealized model of a fiber. The differences compared to more realistic refractive index distributions are small and beyond the scope of this work.

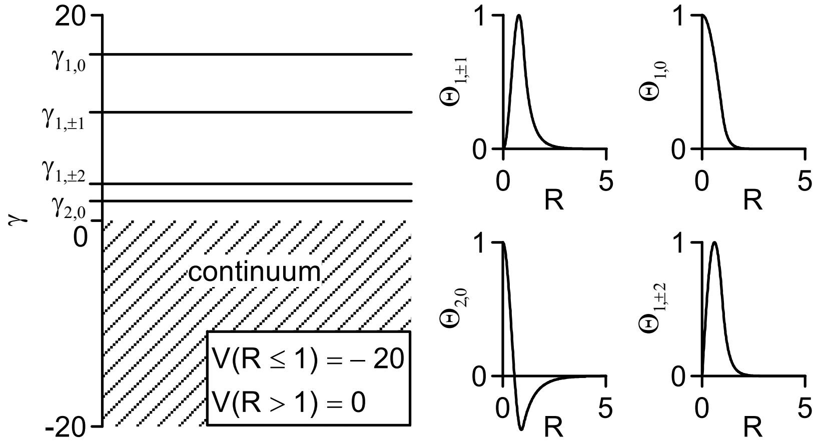

Figure 3.1.: Discrete eigenvalues $\gamma_{j,M}$ of Equation (3.2a) and radial shapes of the corresponding localized linear modes $\Theta_{j,M}$. The given step-potential supports four localized modes.

From each of the localized linear modes $\Theta_{j,M}$ of Equation (3.2a) a branch of nonlinear bound states $\psi(R,\Phi,Z) = U_{j,M}(R)\exp(iM\Phi + i\beta_{j,M}Z)$ of Equation (3.1) emanates [14, 15, 50, 51]. One can interpret the localized linear modes $\Theta_{j,M}$ as "solitons" with zero power $P = 2\pi\int |U_{j,M}|^2\, RdR$, or equivalently corresponding to $\sigma = 0$ (see Figure 3.2). Because both U and Θ are solutions of real-valued differential equations, we consider each of them as being real.

By means of functional relations (see, e.g., [14, 15]), nonlinear bound states $U \equiv U_{j,M}$ of Equation (3.1) can easily be proven to satisfy

$$\beta = \frac{\sigma\int U^4 RdR - \int (\nabla U)^2\, RdR - \int U^2 V RdR}{\int U^2 RdR}, \tag{3.3}$$

where $(\nabla U)^2 = (\partial_R U)^2 + M^2U^2/R^2$ and $\beta \equiv \beta_{j,M}$. Therefore, for $\sigma > 0$ we can expect $\beta > \gamma_{j,M}$ and $\sigma < 0$ indicates $\beta < \gamma_{j,M}$.

3.1.2. Stability analysis of nonlinear bound states

According to the standard procedure for linear stability analysis we introduce a small perturbation δU on the nonlinear bound state U. We plug

$$\Psi = (U + \delta U)\exp(iM\Phi + i\beta Z) \tag{3.4}$$

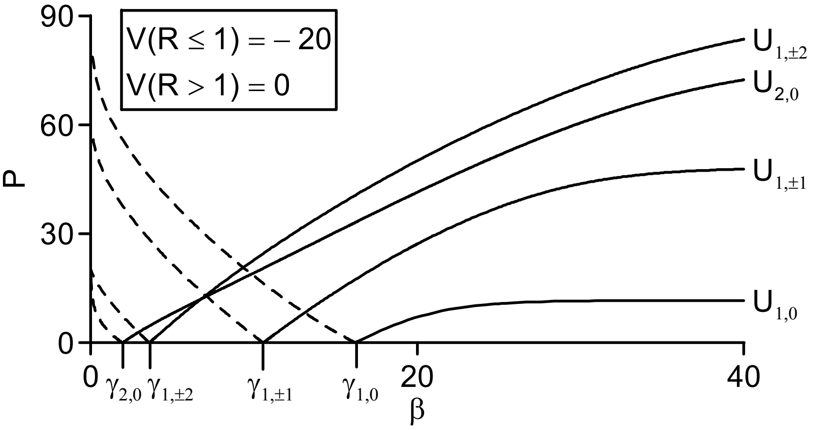

Figure 3.2.: "Soliton" power P versus parameter β ($\sigma = +1$ solid lines, $\sigma = -1$ dashed lines): The four discrete linear modes $\Theta_{j,M}$ can be seen as "solitons" with zero power.

into Equation (3.1) and linearize with respect to the perturbation. The resulting evolution equation for the perturbation δU is given by

$$\begin{aligned} & i\frac{\partial}{\partial Z}\delta U - \beta\delta U - V\delta U + 2\sigma U^2\delta U + \sigma U^2\delta U^* \\ & + \frac{1}{R}\frac{\partial}{\partial R}\left(R\frac{\partial}{\partial R}\right)\delta U + \frac{1}{R^2}\left(\frac{\partial}{\partial\Phi} + iM\right)^2\delta U \quad = \quad 0. \end{aligned} \tag{3.5}$$

With the ansatz

$$\delta U(R,\Phi,Z) = \delta U_1(R)\,\mathrm{e}^{im\Phi+i\lambda Z} + \delta U_2^*(R)\,\mathrm{e}^{-im\Phi-i\lambda^* Z} \tag{3.6}$$

we then derive the eigenvalue problem

$$\hat{L}\begin{pmatrix} \delta U_1 \\ \delta U_2 \end{pmatrix} = \lambda\begin{pmatrix} \delta U_1 \\ \delta U_2 \end{pmatrix}, \tag{3.7a}$$

where δU_1 and δU_2 are independent complex functions and

$$\hat{L} = \begin{pmatrix} \hat{D}_{M+m} - \beta + 2\sigma U^2 & \sigma U^2 \\ -\sigma U^2 & -\hat{D}_{M-m} + \beta - 2\sigma U^2 \end{pmatrix}. \tag{3.7b}$$

Since the resulting linear operator $\hat{L}$ is real, we expect pairs of eigenvalues (λ, λ^*). If for a given bound state U all eigenvalues λ of Equation (3.7a) are real numbers, we call U orbitally stable, otherwise we call it linearly unstable. Table 3.1 summarizes the nomenclature used in this section.

Θ: linear mode of the potential V γ: related eigenvalue M: vorticity of the linear mode Θ	$\gamma\Theta = \hat{D}_M\Theta$
$\Theta_{j,M}$: localized mode $\gamma_{j,M}$: related discrete eigenvalue	$\Theta_{\gamma_c,M}$: delocalized radiative mode $\gamma_{\gamma_c,M}$: related continuous eigenvalue
U: nonlinear bound state (soliton) β: related soliton parameter M: vorticity of the soliton U	$\beta U = \hat{D}_M U + \sigma U^3$
$U_{j,M}$: $\lim\limits_{P\to 0} U_{j,M} = \Theta_{j,M}$	$\beta_{j,M}$: $\lim\limits_{P\to 0} \beta_{j,M} = \gamma_{j,M}$
δU: perturbation to the soliton U $\delta U = \delta U_1 \exp(im\Phi + i\lambda Z)$ $+\delta U_2^* \exp(-im\Phi - i\lambda^* Z)$ λ: related eigenvalue m: vorticity of perturbation δU	$\hat{L}\begin{pmatrix} \delta U_1 \\ \delta U_2 \end{pmatrix} = \lambda \begin{pmatrix} \delta U_1 \\ \delta U_2 \end{pmatrix}$

Table 3.1.: Overview on the nomenclature.

Here we address the stability of the nonlinear bound states U for low powers P. For $\sigma > 0$, this is the only regime where we can expect stability, because for high enough powers the linear potential in Equation (3.1) becomes negligible, and all bound states of the resulting two-dimensional NLS equation are unstable, by either spreading or collapsing to a singularity [52]. So the question we want to answer is: does a linear mode $\Theta_{j,M}$ become always unstable if we increase the power, or can it be continued into a nonlinear state $U_{j,M}$ remaining stable up to a certain threshold power? In order to shed light onto this issue, we split the linear operator of the eigenvalue problem Equation (3.7a) into two operators $\hat{L} = \hat{H} + \sigma\hat{N}$, where

$$\hat{H} = \begin{pmatrix} \hat{D}_{M+m} - \beta & 0 \\ 0 & -\hat{D}_{M-m} + \beta \end{pmatrix} \tag{3.8}$$

is self-adjoint and

$$\hat{N} = \begin{pmatrix} 2U^2 & U^2 \\ -U^2 & -2U^2 \end{pmatrix} \tag{3.9}$$

contains the dependency on the nonlinear bound state U. So, for small powers $\hat{N}$ acts as a perturbation on $\hat{H}$. For $P = 0$ (or $\sigma = 0$) we have $\hat{L} = \hat{H}$, $\beta = \gamma_{j,M}$ and each row of Equation (3.7a) is equivalent to Equation (3.2a). Hence, in the spectrum of operator $\hat{H}$, all the linear modes of the waveguide structure are reproduced twice. The solutions of the eigenvalue problem

$$\hat{H}\begin{pmatrix}\delta U_1\\ \delta U_2\end{pmatrix}=\lambda\begin{pmatrix}\delta U_1\\ \delta U_2\end{pmatrix} \tag{3.10}$$

are the localized eigenfunctions (modes of the discrete spectrum of $\hat{H}$) defined as

$$\begin{pmatrix}\Theta_{k,M'}\\ 0\end{pmatrix},\quad \lambda=\gamma_{k,M'}-\beta,\qquad m=M'-M,\quad \text{and}$$

$$\begin{pmatrix}0\\ \Theta_{k,M'}\end{pmatrix},\quad \lambda=-\gamma_{k,M'}+\beta,\quad m=M-M',$$

and the delocalized eigenfunctions (radiative modes of the continuous spectrum of $\hat{H}$) defined as

$$\begin{pmatrix}\Theta_{\gamma_c,M'}\\ 0\end{pmatrix},\quad \lambda=\gamma_c-\beta,\qquad m=M'-M,\quad \text{and}$$

$$\begin{pmatrix}0\\ \Theta_{\gamma_c,M'}\end{pmatrix},\quad \lambda=-\gamma_c+\beta,\quad m=M-M',$$

where still $\beta=\gamma_{j,M}$. Note that the angular momentum M' consists of the amount of both momenta M (soliton) and m (perturbation) fixed by our ansatz [Equations (3.4, 3.6)].

If $\lambda\leq-\beta$ or $\lambda\geq\beta$ we always find a delocalized eigenfunction of Equation (3.10), either $\begin{pmatrix}\Theta_{\gamma_c,M'}\\ 0\end{pmatrix}$ or $\begin{pmatrix}0\\ \Theta_{\gamma_c,M'}\end{pmatrix}$. Besides, for a certain range of potential depths, some of the discrete eigenvalues $\gamma_{k,M'}$ of Equation (3.2a) lie in the domain $2\beta-\gamma_{k,M'}<0$, so that the *discrete* eigenvalues $\lambda=\pm\left(\gamma_{k,M'}-\beta\right)$ of the localized eigenfunctions $\begin{pmatrix}0\\ \Theta_{k,M'}\end{pmatrix}$ and $\begin{pmatrix}\Theta_{k,M'}\\ 0\end{pmatrix}$ are embedded in the *continuous* parts of the spectrum. In such a configuration, there exists degeneration between a continuous and a discrete eigenvalue. This type of degeneration will be crucial throughout our analysis.

Before we go on and look at the effects of the perturbation $\hat{N}$, it might be helpful to illustrate these considerations with the example of Figure 3.1. As mentioned above, with the knowledge of the eigenvalues of Equation (3.2a) it is easy to construct the spectrum of the operator $\hat{H}$: each eigenvalue γ in Equation (3.2a) creates a pair of eigenvalues $\lambda=\gamma-\beta$ and $\lambda=\beta-\gamma$ in the spectrum of $\hat{H}$. Figure 3.3 shows the construction of the spectrum for two different choices of β. For the vortex state with

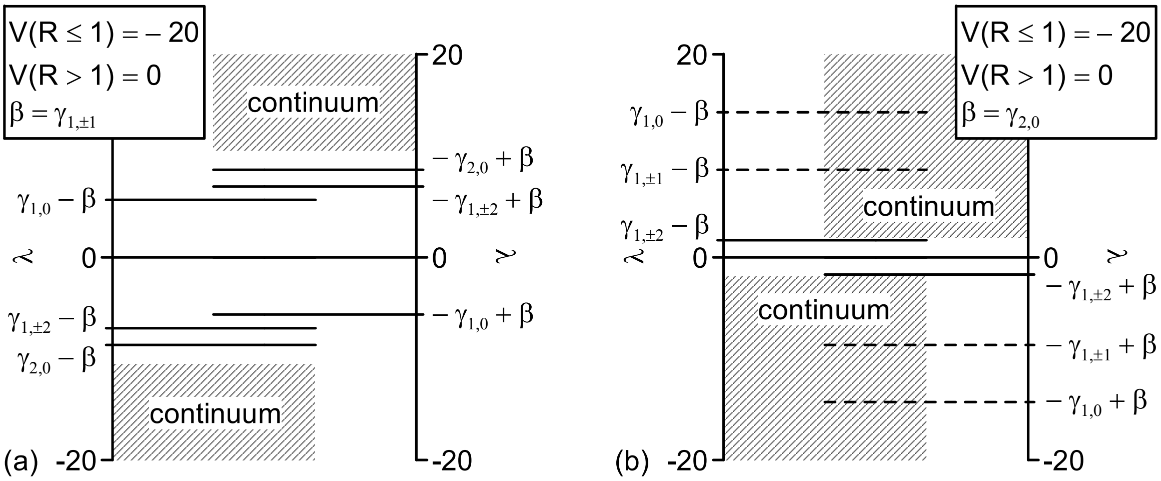

Figure 3.3.: Eigenvalues of Equation (3.10) for two different choices of β. Two spectra of Figure 3.1 are superimposed. One spectrum is shifted by an amount of β downwards (left axis), the other one is mirrored ($\lambda \to -\lambda$) and shifted by an amount of β upwards (right axis). In (a) the discrete and the continuous eigenvalues stay separated, in (b) we observe some discrete eigenvalues embedded in the continuum (dashed lines).

$\beta = \gamma_{1,\pm1}$ [see Figure 3.3 (a)], the discrete eigenvalues and the two continua are clearly separated. The eigenvalues attached to the left axis belong to the first row of operator $\hat{H}$, while those appendant to the right axis belong to the second one. On the contrary, for the multi-humped state with $\beta = \gamma_{2,0}$ [see Figure 3.3(b)], some of the discrete eigenvalues are now embedded in the continuum. So, formally we have a degeneration between continuous and discrete eigenvalues. This degeneration is due to the fact that Equation (3.10) is composed of two *decoupled* equations. When we introduce the perturbation $\hat{N}$, the latter property does no longer hold.

If we start with the spectrum of the operator $\hat{H}$ and switch on the perturbation $\hat{N}$, we expect that eigenvalues of $\hat{H}$ will shift. In particular, any degeneration between discrete eigenvalues and continuous eigenvalues, as described above, should be lifted. Note that trivially degenerated eigenvalues ($M' \to -M'$) will not split, since the generic symmetry is not changed by the nonlinearity. In contrast to $\hat{H}$, the operator $\hat{L}$ is not self adjoint, so eigenvalues can become complex. But since $\hat{L}$ is real, this can only happen in pairs (λ, λ^*). *This property, therefore, implies that two eigenvalues have to be degenerated first, before the pair can move to the complex plane and destabilize the nonlinear bound state under consideration.* So, on the one hand, degeneration of two eigenvalues is necessary for destabilization. On the other hand, we know about any possible degeneration just from looking at the spectrum of the operator $\hat{H}$.

The same conclusion applies to more general nonlinearities and arbitrary dimensionality in Equation (3.1), provided the equation features an “attractive” potential supporting localized linear modes. The key-point is that eigenvalues of the perturbation operator $\hat{L}$ only appear in pairs $(\lambda,\, \lambda^*)$. An operator splitting $\hat{L} = \hat{H} + \sigma\hat{N}$ as above is always possible, where $\hat{H}$ is independent of the nonlinear bound state and self-adjoint. Then, our arguments using discrete eigenvalues of operator $\hat{H}$ embedded in the continuum hold, because two eigenvalues of operator $\hat{L}$ have to be degenerated first, before the pair can move to the complex plane.

In our whole reasoning we have taken for granted that discrete eigenvalues of operator $\hat{L}$ do not vanish or emerge, apart from moving to or coming from the continuum. It is easy to see that this is true for the discretized problem in a finite box $[0, R_{max}]$. Here, the operator $\hat{L}$ is a finite-dimensional square matrix. Because for a sufficiently fine grid and a sufficiently large box in particular the discrete eigenvalues of the continuous, unbounded problem are very well described by the discrete one, our assumption is justified.

3.1.3. Stability criterion for low-power bound states

The above arguments allow us to formulate a stability criterion for low-power nonlinear bound states of Equation (3.1): If a certain localized linear mode Θ_{j_0,M_0} of Equation (3.2a) with eigenvalue γ_{j_0,M_0} fulfills

$$\frac{1}{2}\gamma_{j,M} < \gamma_{j_0,M_0} \text{ for all } j,\, M, \tag{3.11}$$

the corresponding nonlinear bound state U_{j_0,M_0} is linearly stable for small powers. On the contrary, if the criterion (3.11) is not fulfilled, it is likely that an arbitrary small nonlinearity lifts the degeneracy in the spectrum of operator $\hat{L}$ by shifting the two eigenvalues to the complex plane and leading thereby to the instability of the nonlinear bound state. As a direct consequence of this criterion, the ground state with β emanating from $\gamma_{1,0}$ is always stable. Figure 3.4 shows an illustrative example of this destabilization mechanism for $\sigma = +1$. Note that the criterion (3.11) applies to both focusing ($\sigma > 0$) and defocusing ($\sigma < 0$) nonlinearities.

Before proceeding further, it might be helpful to illustrate the criterion (3.11) in the picture of four-wave-mixing. Here, we consider partially degenerate four-wave-mixing: A strong “pump-wave” with wave-number k_1 creates two side bands located symmetrically at the wave-numbers k_3 and k_4, obeying $k_1 - k_3 = k_4 - k_1$, where we assume for definiteness $k_3 < k_4$ (see, e.g., Ref [53]). Of course, the creation of side bands requires the existence of such waves in the medium. Brought forward to

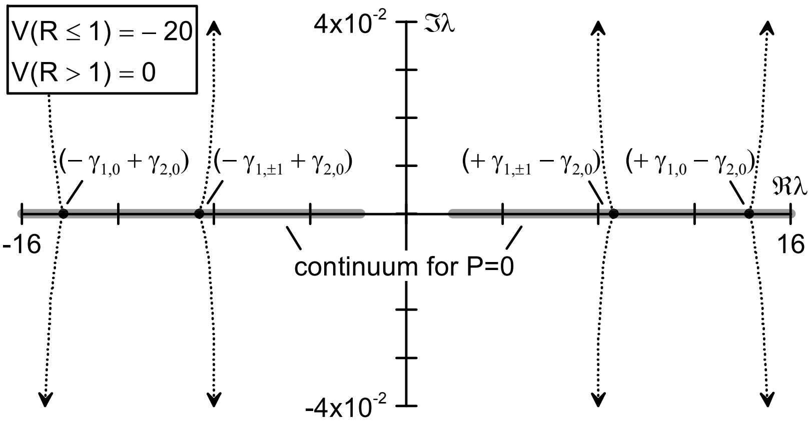
V(R ≤ 1) = – 20
V(R > 1) = 0
4x10^{-2}
$\Im\lambda$
$(-\gamma_{1,0}+\gamma_{2,0})$
$(-\gamma_{1,\pm1}+\gamma_{2,0})$
$(+\gamma_{1,\pm1}-\gamma_{2,0})$
$(+\gamma_{1,0}-\gamma_{2,0})$
$\Re\lambda$
-16
16
continuum for P=0
-4x10^{-2}

Figure 3.4.: The degeneracy of the embedded discrete eigenvalues is lifted by the cubic nonlinearity ($\sigma = +1$); the eigenvalues move to the complex λ-plane. The nonlinear bound state under consideration in this example is the multi-humped state emanating from $\gamma_{2,0}$ ($\beta \geq \gamma_{2,0}$).

our system, the “pump-wave” corresponds to the low-power nonlinear bound state $U_{j_0,M_0} \approx \Theta_{j_0,M_0}$ with $k_1 = \beta \approx \gamma_{j_0,M_0}$. Another mode of the potential $\Theta_{j,M}$ can only be excited as a “third wave” ($k_3 = \gamma_{j,M}$) if there is a matching ”fourth wave”, namely $\Theta_{\gamma_c,M}$ with wave-number $k_4 = \gamma_c = 2\gamma_{j_0,M_0} - \gamma_{j,M}$. If the stability criterion (3.11) is fulfilled, no matching ”fourth wave” exists. Hence, the ”third wave” cannot grow and cause instability of the nonlinear bound state U_{j_0,M_0}. On the contrary, if the criterion is not fulfilled, we always find a matching ”fourth wave” in the continuum.

To clear up the effects of the nonlinearity, we consider the asymptotics of unstable eigenmodes (eigenfunctions of operator $\hat{L}$ with complex eigenvalue λ, $\Im\lambda < 0$) with $\lim_{P\to 0}\Re\lambda \to \lambda_0 > \gamma_{j_0,M_0}$ and $0 < |\Im\lambda| \ll \lambda_0$, $\Im\lambda < 0$ (the case $\lambda_0 < -\gamma_{j_0,M_0}$ can be treated in a similar way). Since in the linear limit [Equation (3.10)] all eigenmodes are stable, we have $\lim_{P\to 0}\Im\lambda \to 0$. By solving Equation (3.7a) in the asymptotic regime $R \to \infty$ and linearizing the exponential arguments with respect to $\Im\lambda$ we find

$$\delta U_1 \sim \frac{1}{\sqrt{R}}\exp\left[\left(-\sqrt{\Re\lambda+\beta} - i\frac{\Im\lambda}{2\sqrt{\Re\lambda+\beta}}\right)R\right] \tag{3.12a}$$

$$\delta U_2 \sim \frac{1}{\sqrt{R}}\exp\left[\left(-i\sqrt{\Re\lambda-\beta} + \frac{\Im\lambda}{2\sqrt{\Re\lambda-\beta}}\right)R\right], \tag{3.12b}$$

where both components δU_1 and δU_2 are localized (finite power integral). This is worth noticing, since in contrast to δU_1, the component δU_2 is delocalized in the linear limit $\Im\lambda = 0$ ($P = 0$ or $\sigma = 0$). Due to the non-diagonal elements of the operator $\hat{N}$ we can conclude that both δU_1 and δU_2 have nonzero norm. More precisely, it is possible to show that

$$\Im\lambda \int \left(|\delta U_1|^2 - |\delta U_2|^2\right) RdR = 0 \tag{3.13}$$

(see Appendix A.1 for details) and therefore

$$\int |\delta U_1|^2 \, RdR = \int |\delta U_2|^2 \, RdR \overset{!}{=} 1. \tag{3.14}$$

Henceforth the symbol $\overset{!}{=}$ signifies that the power integrals of δU_1 and δU_2 can be set equal to unity without loss of generality, by virtue of the linear nature of the equations which these perturbations satisfy. By doing so, Equation (3.14) provides useful information on the maximum of their amplitude in the transverse plane. Together with the asymptotics [Equations (3.12)], we are now able to evaluate the dependency of $\max|\delta U_1|^2$ and $\max|\delta U_2|^2$ on $|\Im\lambda| \ll \lambda_0$, which will allow us to deduce further results.

3.1.3.1. Dependency of $\max|\delta U_1|^2$ on $|\Im\lambda|$

Let us have a look at Equation (3.12a). Since the real part of the exponent in the asymptotic regime $-\sqrt{\Re\lambda+\beta}R$ is independent of $\Im\lambda$, we can conclude that $\delta U_1(R) \approx 0$ at large distances $R \gg 1/\sqrt{\Re\lambda+\beta}$. Hence, the entire "mass" of δU_1 is concentrated at finite distances, where $U \neq 0$ and $V \neq 0$. Since $\int |\delta U_1|^2 \, RdR \overset{!}{=} 1$, we have thus

$$\lim_{P\to 0} \left(\max|\delta U_1|^2\right) = C \tag{3.15}$$

where C is *non-zero.*

Equation (3.15) implies that the criterion (3.11) is indeed *sufficient* for small powers: For a vanishing nonlinearity, we have $\Im\lambda = 0$. For continuity reasons, these unstable eigenmodes must converge to a *localized* eigenfunction of the operator $\hat{H}$ with discrete eigenvalue embedded in the continuum. Otherwise, $\max|\delta U_1|^2$ would jump from $C \neq 0$ to zero for power $P = 0$, because delocalized eigenfunctions cannot keep a finite power integral while having nonzero amplitude. Conversely, since the perturbations become localized in one component (δU_1) and delocalized in the other one (δU_2) in the limit $P \to 0$, instability at low powers *necessarily* starts from discrete eigenvalues "embedded" in the continuum of the operator $\hat{H}$. Furthermore, with this knowledge, we can specify the above constants $\lambda_0 = \gamma_{j,M} - \gamma_{j_0,M_0}$ and $C = \max|\Theta_{j,M}|^2$ with $\int |\Theta_{j,M}|^2 \, RdR \overset{!}{=} 1$.

3.1.3.2. Dependency of $\max|\delta U_2|^2$ on $|\Im\lambda|$

For $|\Im\lambda| \ll \lambda_0$ all the mass of δU_2 lies at large distances $R \to \infty$, and with Equation (3.12b) we are able to compute $\int |\delta U_2|^2 \, RdR \sim 1/|\Im\lambda|$. Since we have fixed $\int |\delta U_2|^2 \, RdR \overset{!}{=} 1$, the previous estimate implies that

$$\max|\delta U_2|^2 \sim |\Im\lambda| \,. \tag{3.16}$$

Besides, if we remember that Equation (3.7a) is a linear differential equation, it is obvious that there exists a Green's function $G(R, R')$ with

$$\delta U_2(R) = \int G(R, R') \, \sigma U(R')^2 \, \delta U_1(R') \, R' dR', \tag{3.17}$$

which means $\max|\delta U_2| \sim \sigma \max U^2$. Hence, we obtain

$$\sqrt{|\Im\lambda|} \sim \sigma \max U^2, \tag{3.18}$$

so the growth rate $|\Im\lambda|$ of the unstable eigenmode is proportional to the squared nonlinearity.

In order to express this dependency in terms of the "soliton parameter" β, we may perform a perturbative analysis in the limit $|\sigma| \ll 1$, similarly to Refs. [49, 54]. We expand the nonlinear bound state U as

$$U = \Theta + \sigma U^{(1)} + \mathcal{O}\big(\sigma^2\big) \tag{3.19}$$

and

$$\beta = \gamma + \sigma\beta^{(1)} + \mathcal{O}\big(\sigma^2\big) \,, \tag{3.20}$$

where $\Theta \equiv \Theta_{j_0,M_0}$ and $\gamma \equiv \gamma_{j_0,M_0}$ satisfy Equation (3.2a). Plugging the ansatz $\psi = U \exp(iM_0\Phi + i\beta Z)$ into Equation (3.1), it is readily found that

$$\beta^{(1)} = \frac{\int \Theta^4 RdR}{\int \Theta^2 RdR} \sim \max\Theta^2. \tag{3.21}$$

Hence, with Equation (3.20) we have $\beta - \gamma \sim \sigma \max\Theta^2$. For small $|\sigma|$, thus $\max\Theta^2 \sim \max U^2$ [see Equation (3.19)], the nonlinearity depends on the "soliton parameter" as $\sigma \max U^2 \sim \beta - \gamma$. Together with Equation (3.18) we get

$$|\Im\lambda| \sim (\beta - \gamma)^2 \,. \tag{3.22}$$

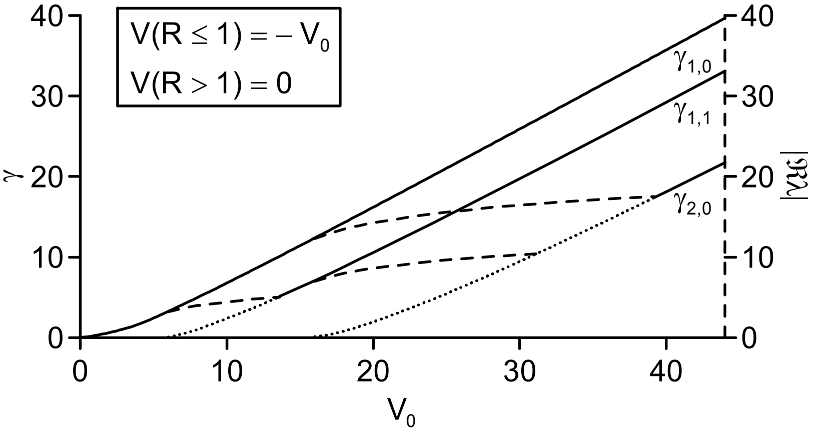

Figure 3.5.: Eigenvalue γ versus the depth of the step-potential V for the linear modes $\Theta_{1,0}$, $\Theta_{1,1}$ and $\Theta_{2,0}$. Solid lines indicate a free-of-degeneration spectrum of operator $\hat{H}$; domains with discrete eigenvalues embedded in the continuum are specified in dotted lines. The dashed lines show the absolute values of the embedded eigenvalues λ of Equation (3.10).

Thus, the growth rate of the unstable eigenmode is proportional to the square of the deviation of the soliton parameter β from the zero power limit γ.

The need that eigenvalues of operator $\hat{L}$ have to be degenerated first before moving to the complex plane yields a sufficient condition for stability of low-power nonlinear bound states in the present framework. However, determining compellable analytical arguments showing that the embedded discrete eigenvalues of the operator $\hat{H}$ *always* lead to complex eigenvalues for the operator $\hat{L}$ (unstable eigenmodes) is still an open issue. Nevertheless, in the numerical examples discussed below we always observe this destabilization mechanism.

3.1.4. Numerical results

Let us return to our example, the radial step-potential, and check the above analytical predictions. We will concentrate on the “solitons” emanating from $\gamma_{1,1}$ (vortex state) and from $\gamma_{2,0}$ (multi-humped state) (see Figure 3.2). Figure 3.5 shows the regions of degenerated λ of Equation (3.10) for the three linear modes $\Theta_{1,0}$, $\Theta_{1,1}$ and $\Theta_{2,0}$. Up to a certain depth of the confining potential V, the stability criterion (3.11) is not fulfilled for the higher order modes. At this depth, the last ”embedded eigenvalue” leaves the continuum. In this context it is important to point out that the above destabilization process is *not* due to weak linear guiding of the respective ”soliton”. If this was the case, we would observe a certain non-zero critical power, below which the “soliton” would be stable. In contrast to this scenario, the destabilization appears for *arbitrary* *small* power.

Since the degeneration of the eigenvalues of Equation (3.10) involves the continuum, the related unstable eigenmodes are stretched over a large area, especially for very small powers. Therefore, conventional solver for Equation (3.7a), like, e.g., the NAG-routine F02ECF [55], failed due to the necessity of a very large computational window. We worked around this problem in solving Equation (3.5) directly with a Beam-Propagation-Method (Crank-Nicholson) and transparent boundary conditions.

To confirm the results of our stability analysis, we present full 2D simulations illustrating the decay of unstable low power vortex and multi-humped "solitons". It turns out that, at least for the examples presented here, the final state is correlated with the dominant unstable eigenmode.

3.1.4.1. The vortex state

We first discuss the vortex state. If $6 < V_0 < 13.6$ (boundaries correspond to the lower/upper bounds in Figure 3.5 for eigenvalue degeneracy), we find $\gamma_{1,0}/2 > \gamma_{1,1}$. Hence, the degenerated eigenvalues of Equation (3.10) are $\pm(\gamma_{1,0} - \gamma_{1,1})$. So, we can guess that the low-power nonlinear vortex state in this range of V_0 has an unstable eigenmode with $m = \pm 1$, so that either $\lim_{P\to 0} \delta U_1 = \Theta_{1,0}$ $(M + m = 0)$ or $\lim_{P\to 0} \delta U_2 = \Theta_{1,0}$ $(M - m = 0)$. The real part of this complex eigenvalue is approximately $|\Re\lambda| \approx \gamma_{1,0} - \gamma_{1,1}$. With a deeper potential than the critical value $V_0 = 13.6$, this instability is expected to disappear. In order to check these predictions, a numerical stability analysis of the vortex state was performed for $V_0 = 8$ and $V_0 = 20$. As expected, for $V_0 = 20$ we observed a stable region of the vortex branch for small powers, whereas for $V_0 = 8$ the branch becomes immediately unstable when the nonlinearity comes into play (see Figure 3.6). We successfully checked numerically the "instability onset value" for the depth of the potential $V_0 = 13.6$. The "instability onset value" and the value at which the first discrete eigenvalue just touches the continuum were observed to coincide.

As far as direct simulations are concerned, the first row in Figure 3.6(c) shows the decay of the vortex "soliton" with $\beta = 2.3$ from the potential depth selected in Figure 3.6(a). Perturbed with 1% random amplitude noise at $Z = 0$, the growing unstable eigenmode ($m = 1$) destroys the "doughnut-shape" of the vortex. We see the phase-singularity drifting away at $Z = 17.5$. At $Z = 77.5$ and $Z = 78.3$, respectively, we show two snapshots of the asymptotic behavior, which consists in a spinning single hump solution with a period $\Delta Z \approx 1.7$. This single hump is nothing else but the nonlinear ground state $U_{1,0}$, where additional rotation is induced by a stable eigenmode with

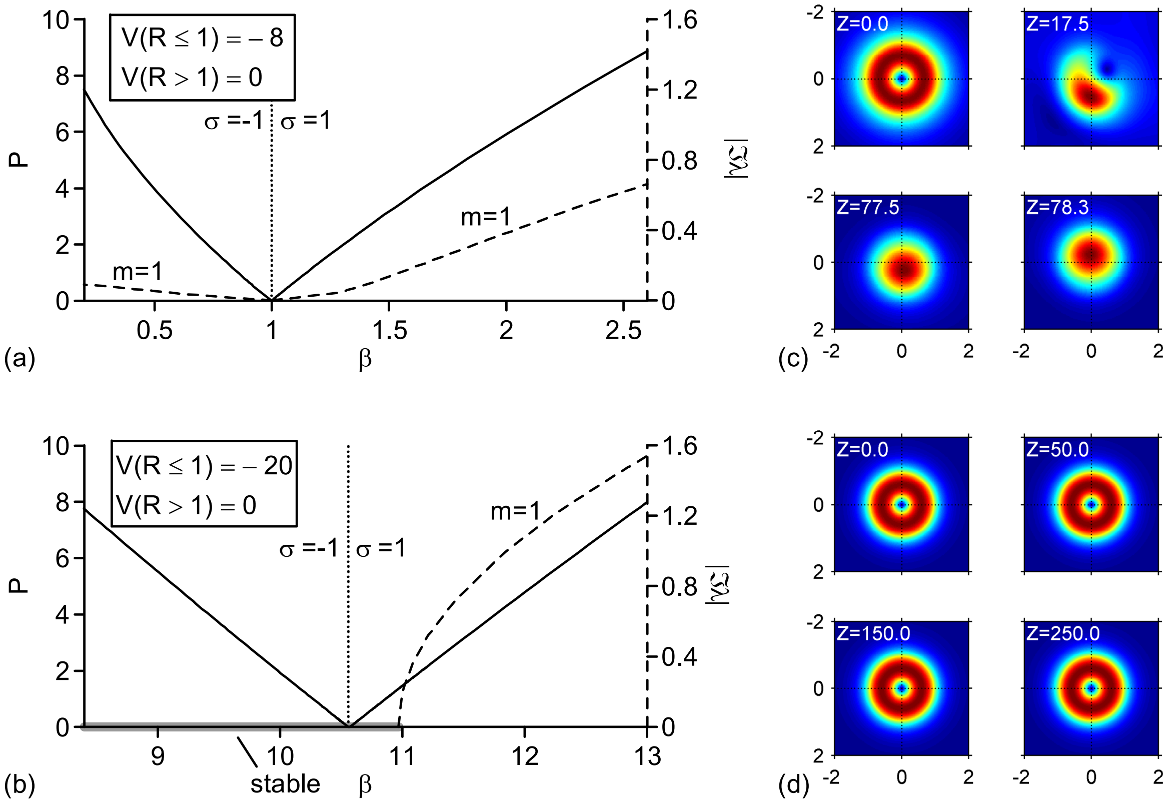

Figure 3.6.: Soliton power P versus soliton parameter β for the vortex state $M = 1$ (solid line). The dashed line shows the computed growth-rate $|\Im\lambda|$ of the unstable eigenmode. If (a) $\gamma_{1,0}/2 - \gamma_{1,1} \geq 0$ the vortex nonlinear bound state is unstable, whereas with (b) $\gamma_{1,0}/2 - \gamma_{1,1} \leq 0$ it is stable for small powers. The evolution of the vortex nonlinear bound state $M = 1$, $\sigma = 1$: (c) instability for $\beta = 2.3$ and $V_0 = 8$; (d) stability for $\beta = 10.966$ (very close to the border of the domain of stability) and $V_0 = 20$.

$m = 1$ and $\lambda = 2\pi/\Delta Z \approx 3.7$. Because we are in the low power regime, we can identify the connection of this eigenmode with $\Theta_{1,1}$, the linear vortex state in Equation (3.2a). Indeed, for $V_0 = 8$ we find $\lambda \approx 3.7 \approx \gamma_{1,0} - \gamma_{1,1}$ (see also Figure 3.5). Figure 3.6(d) displays the numerical verification of the stability predicted for the vortex state with $V_0 = 20$.

3.1.4.2. The multi-humped state

In the case of the multi-humped state, Figure 3.5 shows that, for $16 < V_0 < 31.2$, Equation (3.10) features four degenerated eigenvalues, $\pm(\gamma_{1,0} - \gamma_{2,0})$ related to the ground state $\Theta_{1,0}$, and $\pm(\gamma_{1,1} - \gamma_{2,0})$ related to the vortex state $\Theta_{1,1}$. For potentials deeper than $V_0 = 31.2$ the degeneration of the vortex state first vanishes, and with $V_0 > 39.2$ the stability criterion (3.11) becomes fulfilled. Again, we can confirm these behaviors with a numerical stability analysis (see Figure 3.7). For $V_0 = 20$ the multi-humped branch is unstable for arbitrary small powers due to two unstable eigenmodes. The eigenmode linked to the ground state ($m = 0$) possesses a substantially larger growth rate, so we can expect this one to play the crucial role in the decay of the multi-humped nonlinear bound state (see full 2D simulations in Figure 3.7). The unstable eigenmode associated with the vortex state disappears for a deeper potential ($V_0 = 36$), and choosing $V_0 = 44$ we observe stability for a quite large range of soliton power.

The decay of the multi-humped "solitons" produced by the potentials used in Figure 3.7(a) and (b) with $\beta = 4.3$ and $\beta = 16$ is shown in Figure 3.7(d) and (e), respectively. Again we end up with the stable ground state breathing due to stable eigenmodes with $m = 0$. The periods of oscillation $\Delta Z \approx 0.45$ and $\Delta Z \approx 0.35$ between the two extremal beam shapes shown in the respective last two pictures is compatible with the eigenvalues $\lambda = 14$ and $\lambda = 18$: we retrieve these values as the difference $\gamma_{1,0} - \gamma_{2,0}$ computable from Figure 3.5. As expected, a sufficient depth ($V_0 = 44$) of the potential stabilizes the higher-order nonlinear bound state with $M = 0$ [Figure 3.7(f)]. The fact that unstable "solitons" decay to the stable ground state seems to be generic in this low-power regime. At least, we observed this behavior in all numerical examples. However, for higher powers we have to expect instabilities leading to the collapse of the beam.

To sum up, we presented a sufficient stability criterion for weakly nonlinear bound states (weakly nonlinear guided waves). The simple knowledge of the eigenvalues associated with the linear modes of the potential V (refractive index distribution) allows us to predict the stability of the nonlinear bound states of the extended NLS equation (3.1). In spite of the fact that the criterion is valid for low power solitons only, the example of a step-potential shows that the present results may hold for wider ranges of power, both for focusing and defocusing nonlinearities.

3.2. Influence of the waveguide on highly nonlinear collapsing beams

Now we leave the low-power regime of Equation (3.1) and turn to high-power beams. We look at solutions of the (2D+1)-dimensional NLS equation and consider a small perturbation by an additional "attractive" (waveguide) or "repelling" potential V. In this high power limit, we expect beam-collapse and study the influence of the potential on these self-trapped solutions analytically. First, in Section 3.2.1, we briefly review

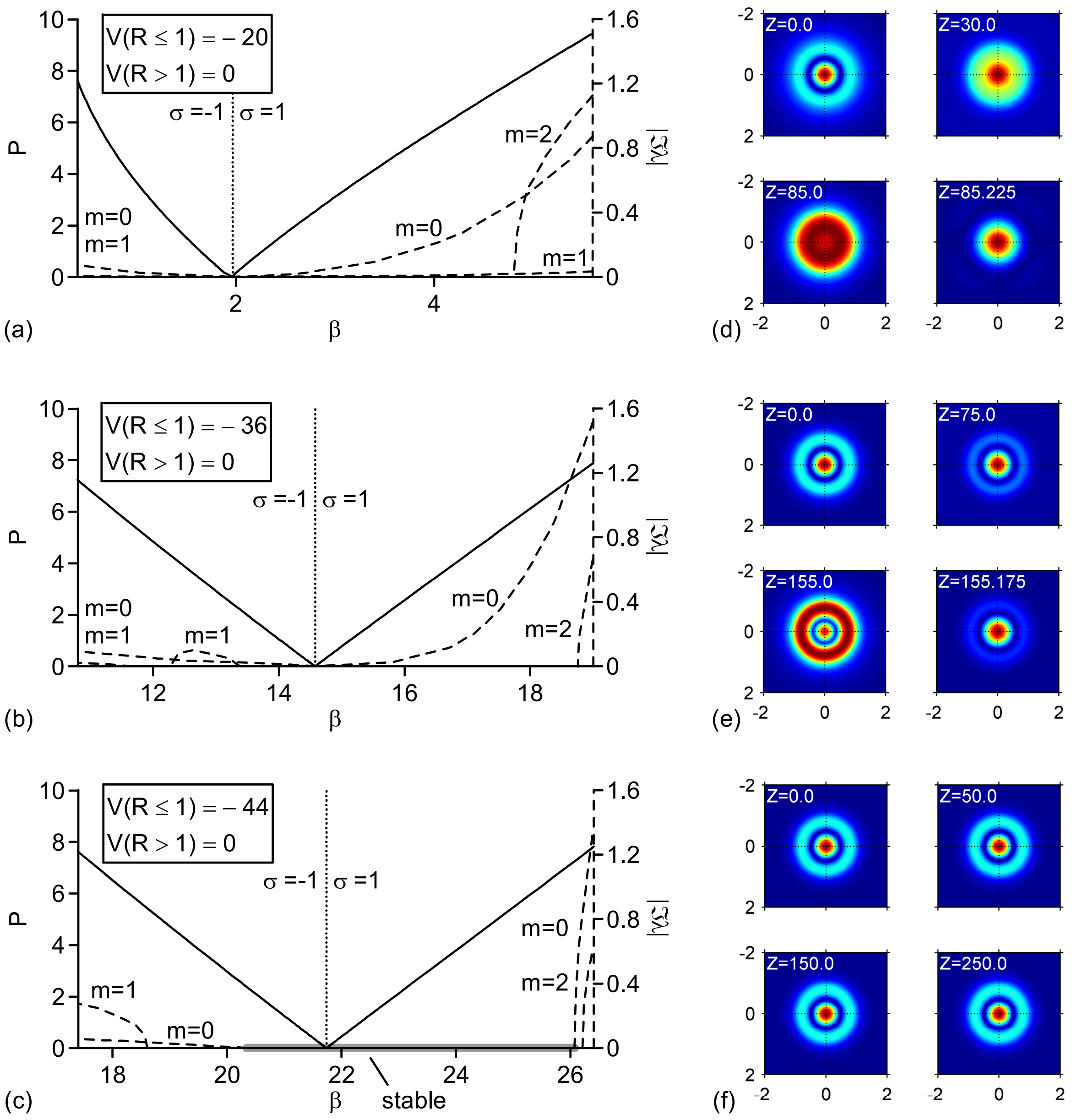

Figure 3.7.: Soliton power P versus parameter β for the multi-humped state $M = 0$ (solid line). The dashed lines show the computed growth-rates $|\Im\lambda|$ of the unstable eigenmodes. If (a) $\gamma_{2,0}/2 - \gamma_{1,1} \geq 0$ and $\gamma_{2,0}/2 - \gamma_{1,0} \geq 0$, the nonlinear bound state has two unstable eigenmodes, whether with (b) $\gamma_{2,0}/2 - \gamma_{1,1} \leq 0$ and $\gamma_{2,0}/2 - \gamma_{1,0} \geq 0$, it has one unstable eigenmode ($m = 0$). In the case of (c) $\gamma_{2,0}/2 - \gamma_{1,1} \leq 0$ and $\gamma_{2,0}/2 - \gamma_{1,0} \leq 0$, the multi-humped state is stable for small powers. The multi-humped nonlinear bound state $M = 0$, $\sigma = 1$: (d) instability for $\beta = 4.3$ and $V_0 = 20$; (e) instability for $\beta = 16$ and $V_0 = 36$; (f) stability for $\beta = 24$ and $V_0 = 44$.

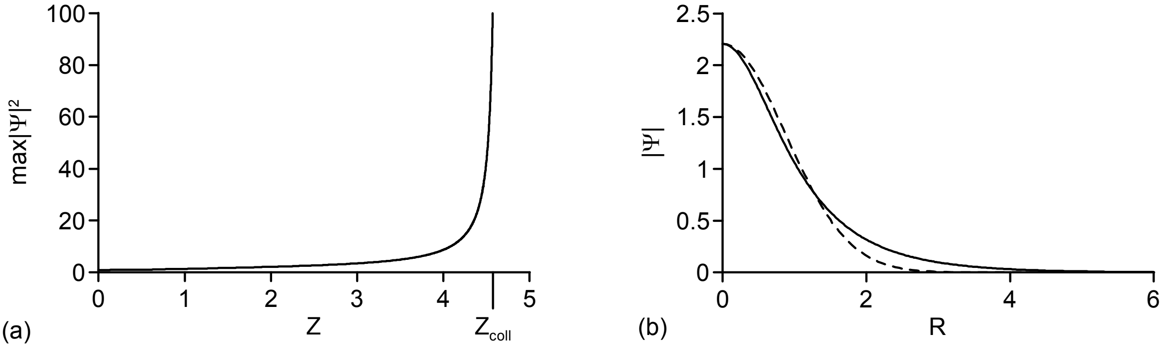

Figure 3.8.: (a) Numerical example for a collapsing solution of the NLS equation. (b) Townes profile T, ground state of the NLS equation [4]; in dashed line a Gaussian with same amplitude and power integral.

some selected features of the NLS equation (for a detailed review see [9]). It is possible to compute upper and lower bounds $P^0_{lcr} < P^0_{thr} < P^0_{ucr}$ for the (unknown) threshold power P^0_{thr} for catastrophic self-focusing. Second, in Section 3.2.2, we show that a similar analysis is possible for Equation (3.1). Surprisingly, the additional potential V can significantly increase the upper bound $P^V_{ucr} > P^0_{ucr}$, even if it is "attractive" like for a waveguide. On the other hand, it turns out that the lower bound $P^V_{lcr} = P^0_{lcr}$ holds for any profile V. Finally, in Section 3.2.3, we verify numerically that indeed even for powers above the upper bound P^0_{ucr} of the homogeneous case a stable propagation is possible (for more detailed numerical investigations, see [56, 57]).

3.2.1. Collapse in the two dimensional Nonlinear Schrödinger Equation

Let us first briefly review selected features of the pure two dimensional NLS equation

$$i\frac{\partial}{\partial Z}\Psi + \left(\frac{\partial^2}{\partial X^2} + \frac{\partial^2}{\partial Y^2}\right)\Psi + |\Psi|^2\Psi = 0. \tag{3.23}$$

For technical convenience, in this section we use Cartesian transversal coordinates X, Y instead of R and Φ. Also, we fix the antecedent parameter σ to unity, because here we treat only focusing nonlinearities.

It is known that for certain initial field distributions $\Psi(X, Y, Z = 0)$ the solution collapses after a finite propagation distance $Z = Z_{coll}$ [see Figure 3.8(a)]. Collapse means in this context that there is at least one pair (X_{coll}, Y_{coll}) with

$$\lim_{Z\to Z_{coll}} \Psi(X_{coll}, Y_{coll}, Z) = \infty.$$

In spite of the fact that for many initial field distributions, at least up to now, only numerics can decide whether the solution collapses or not, there are two quite powerful criteria available. It is possible to derive an universal lower bound $P^0_{lcr} = 11.7$ and a beam shape dependent upper bound P^0_{ucr} for the actual threshold power P^0_{thr}.

In the following analysis we will use two conserved quantities (see Appendix A.2 for details) of the NLS equation, namely the power integral

$$P = \int |\Psi|^2 \, dX dY \tag{3.24}$$

and the Hamiltonian

$$H^0 = \int \left(\left| \frac{\partial}{\partial X} \Psi \right|^2 + \left| \frac{\partial}{\partial Y} \Psi \right|^2 - \frac{1}{2} |\Psi|^4 \right) dX dY. \tag{3.25}$$

3.2.1.1. Lower bound for collapse threshold power for NLS

Weinstein [58] proved that solutions of the NLS do not collapse if their power P is below the critical power

$$P < P^0_{lcr} = P_{Townes} = 2\pi \int T(R)^2 R dR \approx 11.7. \tag{3.26}$$

Here $T(R = \sqrt{X^2 + Y^2})$ is the Townes profile [see Figure 3.8(b)], which is the positive, monotonically decreasing solution of

$$\left(\frac{\partial^2}{\partial R^2} + \frac{1}{R} \frac{\partial}{\partial R} \right) T - T + T^3 = 0, \quad \frac{\partial T}{\partial R}(0) = 0, \quad T(\infty) = 0. \tag{3.27}$$

So Weinstein's criterion provides a lower bound for the threshold power P^0_{thr}. If the power P is smaller than P^0_{lcr}, no catastrophic self-focusing is possible for any initial shape.

The starting idea in Weinstein's proof is that a finite Sobolev norm is sufficient for non collapsing solutions. Let us consider

$$G(Z) = \int \left(\left| \frac{\partial}{\partial X} \Psi \right|^2 + \left| \frac{\partial}{\partial Y} \Psi \right|^2 \right) dX dY = H^0 + \frac{1}{2} \int |\Psi|^4 \, dX dY. \tag{3.28}$$

If $G(Z)$ is bounded for all Z no blowup will occur. It can be shown [58] that the

Townes profile T minimizes the functional

$$J(f) = \frac{\int \left(\left| \frac{\partial}{\partial X} f \right|^2 + \left| \frac{\partial}{\partial Y} f \right|^2 \right) dXdY \int |f|^2 \, dXdY}{\int |f|^4 \, dXdY}. \tag{3.29}$$

Hence we have $J(T) \le J(\Psi)$ for all solutions Ψ. It will turn out later that for the Townes profile the Hamiltonian $H^0_{Townes} = 0$ vanishes, and we get

$$\frac{P_{Townes}}{2} \le \frac{G(Z)P}{\int |\Psi|^4 \, dXdY}. \tag{3.30}$$

Therefore it is $\left[G(Z) - H^0\right] P_{Townes} \le G(Z)P$ and finally we have

$$H^0 \ge G(Z) \left(1 - \frac{P}{P_{Townes}} \right). \tag{3.31}$$

Since H^0 is independent of Z, $G(Z)$ is bounded from above for $P < P_{Townes}$ and the proof is done. No collapse occurs if $P < P_{Townes}$. On the other hand, if $P > P_{Townes}$, $G(Z)$ is unbounded and can go to infinity. Hence, $P > P_{Townes}$ is a *necessary* condition for collapse.

3.2.1.2. Upper bound for collapse threshold power for NLS

The second criterion provides an upper bound for the threshold power P^0_{thr} in the NLS equation [42]. Blow up occurs for sure if the Hamiltonian H^0, which is a constant of motion, is negative. It is easy to see that for any input beam shape

$$B\left(X,Y\right), \quad \int B dXdY = 1, \quad \Psi = \sqrt{P} B$$

the Hamiltonian as a function of P is a parabola which extends to minus infinity. So in terms of the input power this criterion means that catastrophic self-focusing is inevitable if

$$P > P^0_{ucr} = 2 \frac{\int \left(\left| \frac{\partial}{\partial X} B \right|^2 + \left| \frac{\partial}{\partial Y} B \right|^2 \right) dXdY}{\int |B|^4 \, dXdY}. \tag{3.32}$$

In contrast to Weinstein's criterion P^0_{ucr} is strongly dependent on the initial beam shape B.

The key idea for a sufficient collapse criterion is to show that the mean-square radius

$$S(Z) = \int \left(X^2 + Y^2 \right) |\Psi|^2 \, dXdY \tag{3.33}$$

vanishes for a certain propagation distance Z. For the NLS equation, the second derivation of $S(Z)$ with respect to Z is a constant of motion (see Appendix A.3), namely

$$\frac{\partial^2}{\partial Z^2} S = 8H^0. \tag{3.34}$$

Hence, if $H^0 < 0$, $S(Z)$ is a parabola which extends to minus infinity, and therefore becomes zero at finite Z. In particular, we see that for the Townes profile T as a stationary solution S is a constant and the Hamiltonian $H^0_{Townes} = 0$. It is important to note that P^0_{ucr} depends, as the actual power threshold P^0_{thr}, strongly depends on the input beam shape. For example, for a Gaussian input beam $B = \sqrt{2/\pi W_0^2} \exp -(X^2+Y^2)/W_0^2$ with waist W_0 one finds $P^0_{ucr} = 4\pi$ and for a $N = 2$ super-Gaussian input beam $P^0_{ucr} = 4\sqrt{2}\pi$. The numerically determined actual threshold powers are $P^0_{thr} = 11.9$ for the Gaussian and $P^0_{thr} = 12.7$ for the super-Gaussian beam [59]. However, it is common in some contexts to use the general term "critical power" for $P^0_{cr} = 4\pi$, regardless of the actual beam shape (see Section 4).

3.2.2. Collapse behavior in the presence of a waveguide

The above criteria for collapsing solutions can be modified to match the NLS equation with additional potential $V(X,Y)$

$$i\frac{\partial}{\partial Z}\Psi + \left(\frac{\partial^2}{\partial X^2} + \frac{\partial^2}{\partial Y^2}\right)\Psi + |\Psi|^2\Psi - V\Psi = 0. \tag{3.35}$$

Here the conserved Hamiltonian (see Appendix A.2 for details) is

$$H^V = \int \left(\left|\frac{\partial}{\partial X}\Psi\right|^2 + \left|\frac{\partial}{\partial Y}\Psi\right|^2 - \frac{1}{2}|\Psi|^4 + V|\Psi|^2 \right) dXdY. \tag{3.36}$$

3.2.2.1. Lower bound for collapse threshold power for NLS with potential

We find that Weinstein's lower bound holds. If $P < P^V_{lcr} = P^0_{lcr} = P^V_{lcr}$ no collapse occurs for any initial beam shape. To see this, we express

$$G(Z) = H^V + \int \left(\frac{1}{2}|\Psi|^4 - V|\Psi|^2 \right) dXdY \tag{3.37}$$

in terms of the Hamiltonian, and show that $G(Z)$ stays finite for all Z. With Equation (3.30) we have

$$P_{Townes}\left(G(Z) - H^V + \int V\,|\Psi|^2\,dXdY\right) \leq G(Z)P. \tag{3.38}$$

With

$$C_1^V = -\min_{X,Y}\,[V(X,Y)] \tag{3.39}$$

we get $\left[G(Z) - H^V - C_1^V P\right] P_{Townes} \leq G(Z)P$ and finally we have

$$H^V + C_1^V P \geq G(Z)\left(1 - \frac{P}{P_{Townes}}\right). \tag{3.40}$$

Like in Equation (3.31), the right-hand side is independent of Z and $G(Z)$ is bounded from above if $P < P_{Townes}$, no collapse occurs. On the other hand, $P > P_{Townes}$ is a *necessary* condition for collapse.

3.2.2.2. Upper bound for collapse threshold power for NLS with potential

It is more difficult to give a sufficient collapse criterion for the NLS equation with potential. The reason for this is that the second derivations of the mean-square radius $S(Z)$ [Equation (3.33)] with respect to Z is not constant anymore (see Appendix A.3), but

$$\frac{\partial^2}{\partial Z^2}S = 8H^V - 4\int |\Psi|^2\left[2V(X,Y) + \left(X\frac{\partial}{\partial X} + Y\frac{\partial}{\partial Y}\right)V(X,Y)\right]dXdY. \tag{3.41}$$

In order to find an upper bound for this expression we define

$$C_2^V = -\min_{X,Y}\left[V(X,Y) + \frac{1}{2}\left(X\frac{\partial}{\partial X} + Y\frac{\partial}{\partial Y}\right)V(X,Y)\right] \tag{3.42}$$

and get

$$\frac{\partial^2}{\partial Z^2}S \leq 8H^V + 8C_2^V P. \tag{3.43}$$

If $H^V + C_2^V P < 0$, it is obvious that $S(Z)$ will become zero at finite propagation distance. In an analogous manner to the previous section [Equation (3.32)] we can compute an upper bound for the threshold power P_{thr}^V

$$P_{ucr}^V = 2\frac{\int\left(\left|\frac{\partial}{\partial X}B\right|^2 + \left|\frac{\partial}{\partial Y}B\right|^2\right)dXdY + C_2^V + \int V\,|B|^2\,dXdY}{\int |B|^4\,dXdY}. \tag{3.44}$$

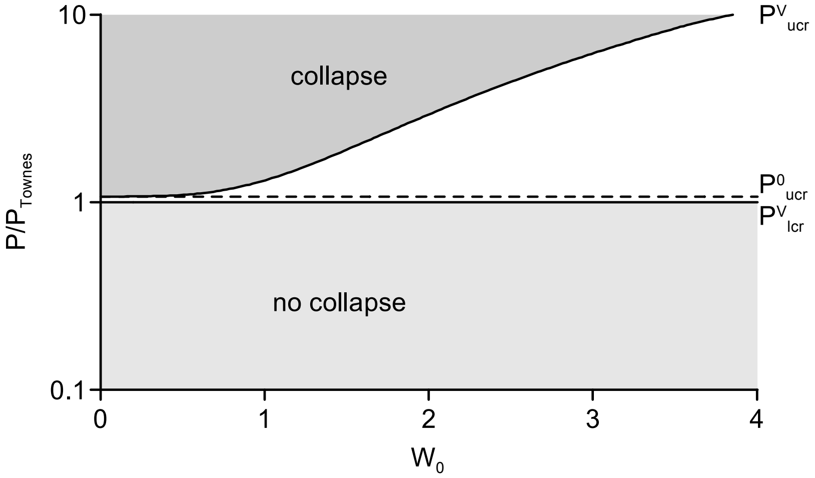

Figure 3.9.: Upper and lower bounds of the threshold power P_{thr}^{V} versus beam-width W_0 for a Gaussian beam and a potential $V = -1.3 \exp\left(-X^2 - Y^2\right)$.

It is important to remember that P_{ucr}^{V} is an upper bound for P_{thr}^{V} only, and may be far from the real threshold power. Moreover, the constant C_2^V contains spatial derivatives of the potential, so, e.g., we run into trouble with a step potential. Nevertheless, P_{ucr}^{V} can be useful to see some general trends. Figure 3.9 shows an illustrative example. If we choose a Gaussian input beam with a width W_0 and a Gaussian potential $V = V_0 \exp\left(-X^2 - Y^2\right)$ (the width of the potential is scaled to unity), the expression for the upper bound reads

$$P_{ucr}^{V} = 4\pi - 2\pi V_0 W_0^2 \left(1 - \frac{2}{2 + W_0^2}\right) \quad V_0 < 0 \tag{3.45a}$$

$$P_{ucr}^{V} = 4\pi + 2\pi V_0 W_0^2 \left(\frac{1}{e} + \frac{2}{2 + W_0^2}\right) \quad V_0 > 0. \tag{3.45b}$$

Hence we expect the threshold power for collapse P_{thr}^{V} increase if the width of the potential is small compared to the beam-width. Also, it would be interesting to see if we can have non collapsing solutions with $P > P_{thr}^{0}$. In the following section we will check this numerically.

3.2.3. Numerical results

In this section we present numerical solutions of Equations (3.23) and (3.35). According to the previous results, we expect the additional potential to increase the threshold power for collapse for wider beams. Figures 3.10(a) and 3.10(b) show the peak intensity over the propagation length for different Gaussian input beams. For growing input width W_0 the beam focuses less [Figure 3.10(a)], and we get non collapsing solutions

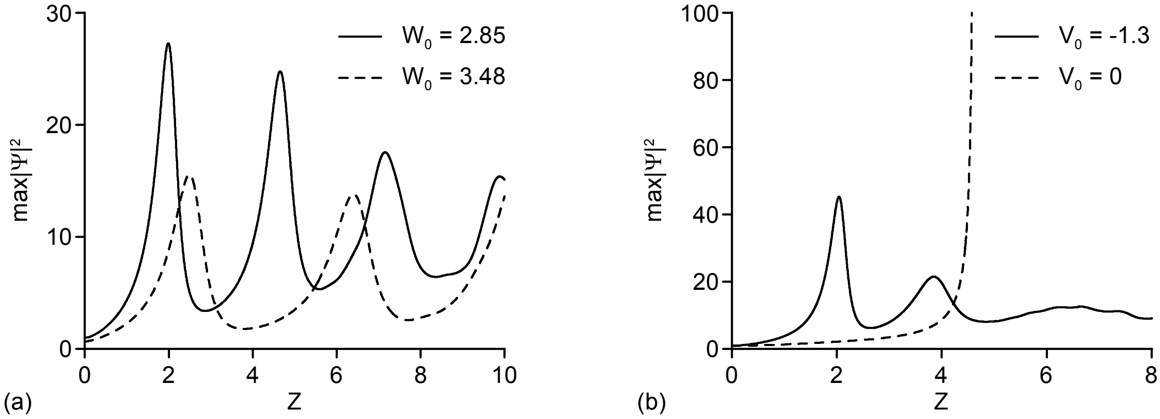

Figure 3.10.: (a) Wider beams focus less, $P = P^0_{ucr}$, $V = -1.3\exp(-X^2 - Y^2)$; (b) Collapse suppression by an "attractive" potential, $P = 1.1P^0_{ucr}$, $W_0 = 3.16$, $V = V_0\exp(-X^2 - Y^2)$.

for powers greater than P^0_{ucr} [Figure 3.10(b)]. An explanation for the increase of the threshold power is the following. For $V \equiv 0$ it is known that in the initial stage of self-focusing, the beam profile changes to a modulated Townes soliton, whereupon power is shed away from the inner part of the beam. The greater the overlap of the initial profile with the Townes profile, the lower is the threshold power P^0_{thr}. The additional interaction of the field with the potential V disturbs this initial stage of self-focusing, and therefore more power is shed away and lost for the self-focusing mechanism than in the homogeneous case. In other words, the beam avoids collapse by splitting between radiation and nonlinear core. This scenario is quite straight forward for "repelling" potentials. At first glance, for "attractive" potentials this effect is astonishing. The explanation is the following. Parts of the beam are focused very fast by the linear effect of the potential and "separated" from the rest of the beam. If this separated quantum of power is too small to collapse by itself, the collapse is suppressed. This mechanism was also observed in [57].

We mentioned in the previous Section that it is not possible to compute P^V_{ucr} [Equations 3.45] for a step potential $V(R \leq 1) = V_0$, $V(R > 1) = 0$. Nevertheless, this type of potential is able to suppress the collapse, too. Figure 3.11 shows an example for collapse suppression by an "attractive" step potential. The choice of parameters corresponds to an optical fiber with $n_b = 1.4$, $n - n_b = 5 \times 10^{-3}$, $\lambda_0 = 600$ nm and $\emptyset_{core} = 7.2$ μm. As mentioned in the antecedent section, the NLS equation with "attractive" potential supports a stable ground state soliton solution (see Figure 3.2). The power of this soliton is below the power of the Townes soliton [14]. When the collapse is suppressed by the potential, the solution relaxes to the ground state soliton and superfluous power is shed away. Oscillatory internal modes of the soliton can lead

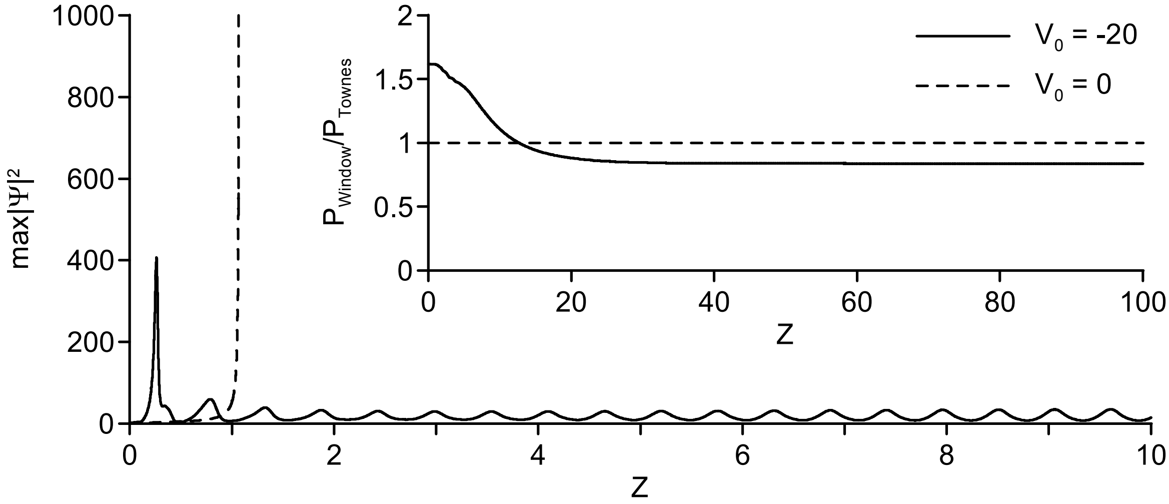

Figure 3.11.: The additional step potential expedites the initial focusing, but the collapse is suppressed and the solution relaxes to the ground state soliton. $P = 1.5P^0_{ucr}$, $W_0 = 2.22$, $V(R < 1) = -20$. The inset shows the evolution of the total power in the computing window. The solution relaxes to the ground state soliton, $P_{soliton} < P^V_{lcr} = P_{Townes}$.

to a breathing solution (see Figure 3.11). Finally, the inset in Figure 3.11 shows the evolution of the power remaining in the numerical box for the same run. We clearly observe the convergence to a power value *smaller* then that of the Townes soliton. The "attractive" potential is able to suppress collapse for powers higher than the critical one for the bulk material, but it is not able to guide these powers.

We evidenced that in the high power regime the waveguide can significantly increase the threshold power for catastrophic self-focusing. Even for powers above the upper bound of the homogeneous case a stable propagation is possible. The explanation for the increase of the threshold power is that the additional interaction of the field with the waveguide disturbs the initial stage of self-focusing, and power is shed away and lost for the self-focusing mechanism. The "nonlinear core" remains in the waveguide and converges to a soliton state with power below critical.

4. High-intense femtosecond pulsed beams in air

This last chapter is devoted to the propagation of high-intense femtosecond pulsed beams in air. In contrast to the previous chapter, a single tangible physical system is under consideration. The more applied and less theoretical nature of this part of the work allows for direct comparison with experimental data. Although temporal dynamics are involved, we focus on the spatial ones of such pulsed beams.

Femtosecond laser pulses are known to form intense channels of light in the atmosphere [10, 18, 20]. These channels result from the interplay between the Kerr self-focusing of the beam and defocusing induced by multiphoton ionization of air molecules. For input powers much larger than the critical value for self-focusing, $P_{cr} = \lambda_0^2/2\pi n_b n_2$, the beam breaks up into several spots producing long waveguides in the medium [21, 22] [S9]. One elementary channel of light stabilized by ionization consists of a femtosecond filament, whose characteristics seem to be generic, i.e., its energy, (FWHM) diameter and intensity are about $\sim$ 1 mJ, $\sim 150\,\mu$m, $10^{13} - 10^{14}$ W/cm^2, respectively, and the electron density in the plasma channel reaches 10^{17} cm^{-3}. As common in the literature of femtosecond filaments, what we call the "critical power for self-focusing" P_{cr} is strictly speaking the upper bound for the collapse threshold computed for a Gaussian input beam in the (2D+1)-dimensional NLS equation (see Section 3.2.1.2), rescaled to physical quantities.

After a brief introduction into single filament solutions in Section 4.1, we address multiple filamentation for high input powers ($10 < P_{in}/P_{cr} < 1000$) (Section 4.2). Because the numerical integration of these equations over long distances in full (3D+1)-dimensional geometry is mostly limited by the available computer capacities, we propose a (2D+1)-dimensional model derived by averaging the time dependency in the laser envelope and the plasma response. This time-averaged model [S6] admits soliton-like states that describe short-range "randomly-nucleated" filaments. We show that these structures confine themselves into a limited number of long-range coherent objects, termed as "optical pillars". Besides transient stages where turbulent cells recur, these new structures around which filaments self-organize drive the pulse dynamics. This property is confirmed by the direct solving of the (3D+1)-dimensional Equations (2.53) applied to millimeter-waisted ultrashort pulsed beams. Second, we compare experiments with numerical simulations, in order to understand how filaments are produced and how they impact on the long-distance propagation of TW pulses with peak powers as high as one thousand times P_{cr}. To do so, three series of experiments involving the Teramobile facility [29, 60] are performed in parallel geometry, with beam powers varying between $120\,P_{cr}$ and $1000\,P_{cr}$. Each series of experiments is numerically simulated by means of the averaged-in-time approach. This model is found to reproduce the qualitative features of the experimental patterns. High-intensity defects in the spatial distribution of the input beam generate "optical pillars" persisting over several tens of meters through the propagation. By "optical pillars" we mean discrete light spots capable of amalgamating short-living soliton-like cells that self-attract around specific points in the diffraction plane. The resulting structure then sustains a long-range propagation, while it can still continue to excite short-range cells in its vicinity. Optical pillars indeed evacuate power as they collapse, so that randomly-nucleated filaments may recur more and more along the optical path, in accordance with the scenario described in [11].

The major difference between the concepts of "optical pillars" and both the "optically-turbulent light guide" [11] and "self-waveguiding" [10, 18] models lies in the following: The possibility of guiding the beam through a small number of quasi-continuous long-range clusters created from its most intense regions. In contrast to the "optically-turbulent light guide", "optical pillars" are robust long-range structures. In contrast to the 'self-waveguiding" picture, an "optical pillar" consists of several filaments. An experiment realized in focused geometry validates this concept: A focused beam is observed to decay into several tens of small-scale cells before the focal point of the beam. The linear lensing shrinks all filaments at the focal point, after which only three quasi-continuous channels of light keeping the same average direction propagate over almost ten meters.

In the final Section 4.3, the interaction of ultrashort laser pulses with opaque droplets in the atmosphere is examined numerically. Intense filaments resulting from the balance between self-focusing and ionization of air molecules are shown to be robust against obscurants sized up to 2/3 of the filament diameter. Our goal is to understand the inner mechanisms that rebuild femtosecond filaments after their collision with obscurants similar to those used in the experiments in [30]. By means of (3D+1)-dimensional numerical simulations, we confirm this spectacular phenomenon and show that it takes place over a few cm after the interaction zone, for droplet sizes up to 2/3 of the filament diameter. Because in reality obstacles do not exactly interact at the filament centroid, emphasis is also given to decentered obscurants. To better understand the rebuilding process, we compare fluence patterns of noisy Gaussian beams with results from our time-reduced model that simulates the propagation of pure solitons resulting from the balance between Kerr self-focusing and plasma defocusing in the presence of an obscurant. The excellent agreement between time-averaged and 3D computations pleads in favor of identifying 3D femtosecond filaments with time-averaged 2D solitons, as suggested in Section 4.2.

All experimental results shown in this Chapter are taken from [S11], if not stated differently.

4.1. Dynamics of a single filaments

Before studying the multiple filamentation of high-intense femtosecond pulsed beams in air, it is worth to have a closer look at the spatio-temporal dynamics of a single filament (Section 4.1.1). In particular the dynamic spatial replenishment mechanism [34] is important for the subsequent sections, because it is used in the derivation of the time-averaged model in 4.2.1. Moreover, the analysis of azimuthal instabilities of the rotationally symmetric filament in Section 4.1.2 allows us to predict that multiple filamentation has its origin in the self-focusing dynamics. A single filament, once formed, is a robust spatial structure which survives over several Rayleigh lengths.

4.1.1. Rotationally symmetric solution

Let us assume that a single filament is rotationally symmetric in x and y. We solve Equations (2.53) in order to get $\mathcal{E}_R(r,z,t)$, where $r=\sqrt{x^2+y^2}$. Here we use a parallel split-step algorithm for the propagation in z. The computing window in r and t moves with the group-velocity of the pulsed beam along the z-axis. In time direction we use a spectral method, whereas the radial coordinate is treated by the Crank-Nicholson scheme. A more detailed description of the code is given in Appendix B.1.2.

Because we are interested in a single filament solution, we choose a Gaussian initial field distribution. It is known that a Gaussian beam tends to form a single self-focusing attractor, whereas a broader super-Gaussian triggers the formation of several independent filaments [27]. We will use that later, when we treat multiple filamentation in Section 4.2. We write

$$\mathcal{E}_R(r,z=0,t)=\sqrt{\frac{2P_{in}}{\pi w_0^2}}e^{-\left(\frac{r^2}{w_0^2}+\frac{t^2}{t_p^2}\right)}, \tag{4.1}$$

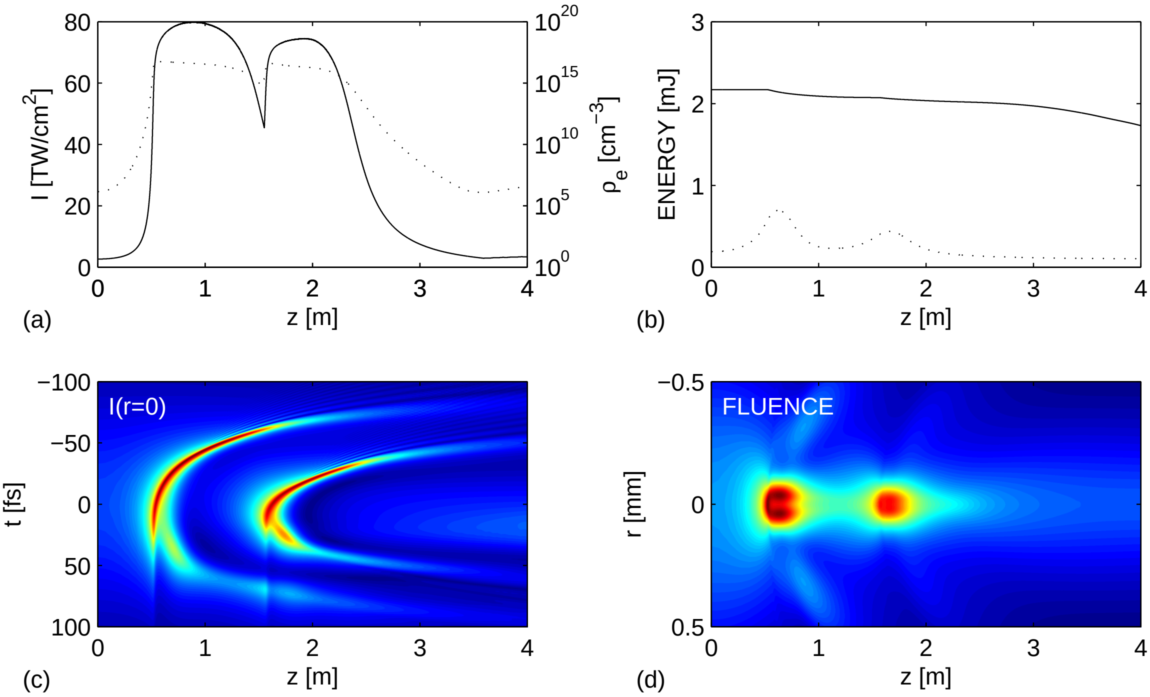

Figure 4.1.: Rotationally symmetric solution [$P_{in} = 20$ GW, $w_0 = 0.7$ mm, $t_p = 85$ fs, see Equation (4.1)]. (a) Evolution of the maximal intensity $\max_{r,t} |\mathcal{E}_R|^2$ (solid line, left-hand axis) and the maximal electron density $\max_{r,t} \rho_e$ (dotted line, right-hand axis). (b) Energy of the pulsed beam $2\pi \int |\mathcal{E}_R|^2 r dr dt$ in the computing window (solid line) and in the core region with radius 150 μm (dotted line) versus propagation distance. The size of the computing window was 5 cm × 700 fs. (c) Evolution of the on-axis temporal intensity distribution $|\mathcal{E}_R(r = 0)|^2$. (d) Fluence $\int |\mathcal{E}_R|^2 dt$ of the beam.

where P_{in} is the peak input power, w_0 the spot size, and t_p the pulse length. Optionally a focusing lens in the waist of the beam is considered, which is described by its transfer function $\exp(-ik_0 r^2/2f)$, where f is the respective focal length. It is useful to express the input power P_{in} in units of $P_{cr} = \lambda_0^2/2\pi n_b n_2$ (~ 3 GW @ 800 nm), which is the critical input power for a two dimensional Gaussian beam to collapse in the (2D+1)-dimensional nonlinear Schrödinger equation [42].

In the following we will show a typical rotationally symmetric single filament solution. We choose $P_{in} = 20$ GW $\sim 6 P_{cr}$, $w_0 = 0.7$ mm, and $t_p = 85$ fs. Figure 4.1 (a) shows the evolution of the maximal intensity of the optical field versus propagation distance z. We can distinguish three propagation stages. First, up to ~ 0.5 m, we have the Kerr stage. Here the electron density ρ_e is below 10^{15} cm^{-3} and therefore its influence in the field evolution is negligible. The beam is self-focused by the optical Kerr effect. Individual time-slices evolve almost independently, since the temporal coupling due to dispersion ($L_D = t_p^2/k'' > 100$ m) and the Raman delayed Kerr response is weak. In the self-channeling regime (~ 0.5 m to ~ 2.5 m), self-focusing is arrested by the defocusing plasma channel. The maximal optical intensity is clamped between 40 and 80 TW cm^{-2}, and the electron density ρ_e can reach 10^{16} to 10^{17} cm^{-3}. In the diffraction stage (here > 2.5 m), the beam diffracts slowly, the intensities are too low for multiphoton ionization. Although diffraction dominates the optical Kerr effect, the nonlinearity is still considerably high and the beam broadens much slower than in pure linear regime.

It is worth noticing that for pulsed beams with input power close to critical a different mechanism exists, which arrests self-focusing. In this power regime, GVD symmetrically splits pulses in time and may dominate over MPI defocusing [61]. However, in this work we deal with much higher input powers and GVD plays a minor role. Its (weak) influence is mainly that it shortens the self-channeling range by decreasing the peak power of focused time-slices [62].

Let us have a closer look on the self-channeling regime. In spite of the strong influence of the generated plasma on the optical field, the overall losses are relatively small [see Figure 4.1(b)]. Hence, the beam can focus several times until the optical power falls below the threshold for self-focusing. In our example we observe two focusing cycles, each maintaining the filament over ~ 1 m. They are clearly visible in Figure 4.1(c) as two "U"-shapes. Here each cycle starts in the center of the pulse ($t \approx 0$). After focusing the pulse splits, and both leading and trailing edge move away from center. The trailing edge is weaker, because it is defocused by the plasma generated in the leading edge. It may happen (not observed in this case) that the trailing edge lives longer than the leading part and become the most prominent spike before the next focusing cycle starts. The crux of the propagation mechanism is that different time slices take turns in maintaining the *same* filament, which is called dynamic spatial replenishment [34]. It explains the spreading of the plasma channel over several Rayleigh lengths $z_0^{fil} = \pi w_{fil}^2/\lambda_0 \sim 3$ cm, where $w_{fil} \sim 85$ μm is the typical waist of the fluence in self-channeling regime [see Figure 4.1(d)].

The snapshots of the intensity distributions versus the coordinates r and t at certain z distances reveal the focusing cycles mentioned above even more clearly [Figure 4.2(a)]. Qualitatively, both cycles are very similar: focusing at $t \approx 0$, pulse splitting and motion to the positive (respectively negative) times. In the case of the second cycle ($z = 1.6$ m and $z = 1.8$ m) low intensity remnants of the first cycle are still visible. The electron density distributions ρ_e shown in Figure 4.2(c) reveal that the generated plasma channel has a width of $\sim 50\mu$m. Moreover, we observe that only the dominant temporal spike is responsible for plasma generation.

Another interesting observation is the formation of spatial rings in certain time-

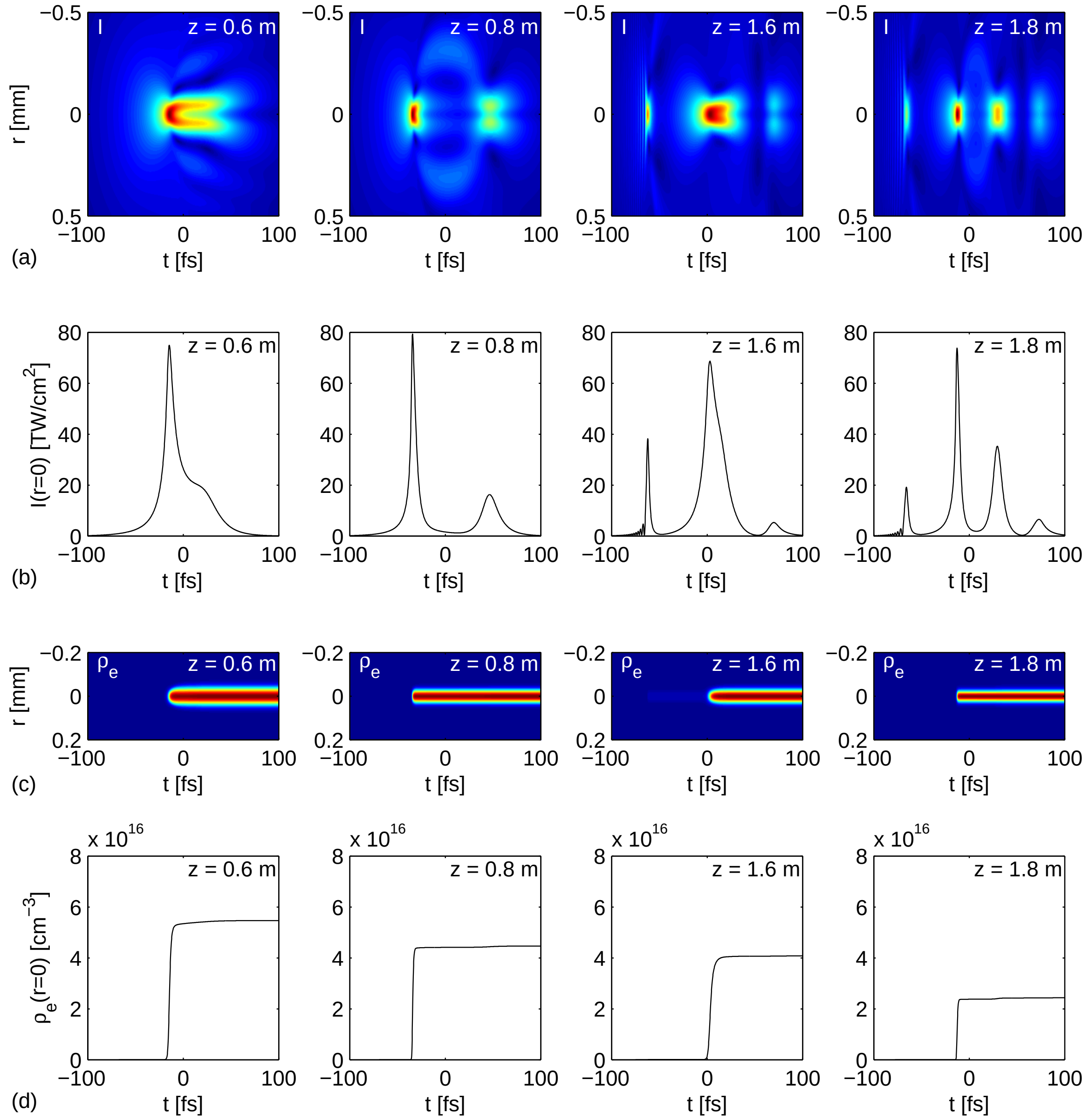

Figure 4.2.: Rotationally symmetric solution [input parameters see Figure 4.1]. (a) Intensity distribution $|\mathcal{E}_R|^2$ at 0.6 m and 0.8 m (first focusing cycle) and at 1.6 m and 1.8 m (second focusing cycle). (b) Corresponding on-axis intensity $|\mathcal{E}_R(r = 0)|^2$ to (a). Inside a focusing cycle the dominant spike moves in t, a new cycle generates a new peak. This "take-over" corresponds to the notch in Figure 4.1(a). (c) Plasma distribution ρ_e at the same propagation distances. (d) On-axis electron density $\rho_e(r = 0)$. The dominant spike alone is responsible for plasma generation.

slices. Nearly all peaks behind (at greater t) the dominant spike have a ring shape. They are caused by a contraction of the field around the defocusing plasma channel, which is generated in the leading part of the pulse. The formation of these rings motivates an azimuthal perturbation analysis of rotationally symmetric single filament solutions.

4.1.2. Azimuthal perturbation analysis

To investigate the influence of azimuthal perturbations which break the rotational symmetry we introduce a small perturbation $\mathcal{E} = \mathcal{E}_R + \delta\mathcal{E}_m$ with

$$\delta\mathcal{E}_m(r,\varphi,z,t) = v_m(r,z,t)\cos m\varphi + w_m(r,z,t)\sin m\varphi, \quad m > 0 \tag{4.2}$$

into Equations (2.53) (simplified by $x_{dK} = 0$ and $\sigma = 0$) and linearize with respect to $\delta\mathcal{E}_m$. This leads to an equation describing the onset of azimuthal instabilities around $\mathcal{E}_R$:

$$\begin{aligned}\frac{\partial}{\partial z}v_m \;=\;& \frac{i}{2k_0}\left(\frac{\partial^2}{\partial r^2}+\frac{1}{r}\frac{\partial}{\partial r}-\frac{m^2}{r^2}\right)v_m - i\frac{k''}{2}\frac{\partial^2}{\partial t^2}v_m + ik_0n_2\left(2\left|\mathcal{E}_R\right|^2 v_m + \mathcal{E}_R^2 v_m^*\right)\\ & -i\frac{k_0\sigma_K\rho_{nt}}{2\rho_c}\left[v_m\int_{-\infty}^{t}\left|\mathcal{E}_R\right|^{2K}dt' + K\mathcal{E}_R\int_{-\infty}^{t}\left|\mathcal{E}_R\right|^{2K-2}\left(\mathcal{E}_R^* v_m + \mathcal{E}_R v_m^*\right)dt'\right]\\ & -\frac{K\beta^{(K)}}{2}\left|\mathcal{E}_R\right|^{2K-2}v_m - \frac{(K-1)\,\beta^{(K)}}{2}\left|\mathcal{E}_R\right|^{2K-4}\mathcal{E}_R^2 v_m^*.\end{aligned} \tag{4.3}$$

The same equation is obtained for w_m, thus it is sufficient to solve Equation (4.3). Because we consider instabilities which break the rotational symmetry we restrict ourselves to $m > 0$ (see [S14] for details).

Simultaneously with $\mathcal{E}_R(r,z,t)$ all $v_m(r,z,t)$ are determined solving Equation (4.3) with the initial condition $v_m(r,z=0,t) \sim r^3\mathcal{E}_R(r,z=0,\tau)$. Obviously this ansatz does not account for every possible perturbation. However, possible distortions of a field distribution are usually correlated with the original shape. Figure 4.3 shows the evolution of the energies contained in each azimuthal component of the perturbation v_m for different input pulses. It is obvious that the crucial parameter which determines the growth rate is the input power P_{in}. Although we increase the pulse duration and add a focusing lens, the prevailing m is invariant [see Figure 4.3(b), (d), (e)]. But if we change the input power, the prevailing m increases with growing P_{in} [see Figure 4.3(a), (b), (c)].

The simplification $x_{dK} = 0$ and $\sigma = 0$ are of minor influence. $x_{dK} = 0$ leads to stronger self-focusing, and therefore the onset of plasma generation is shifted to

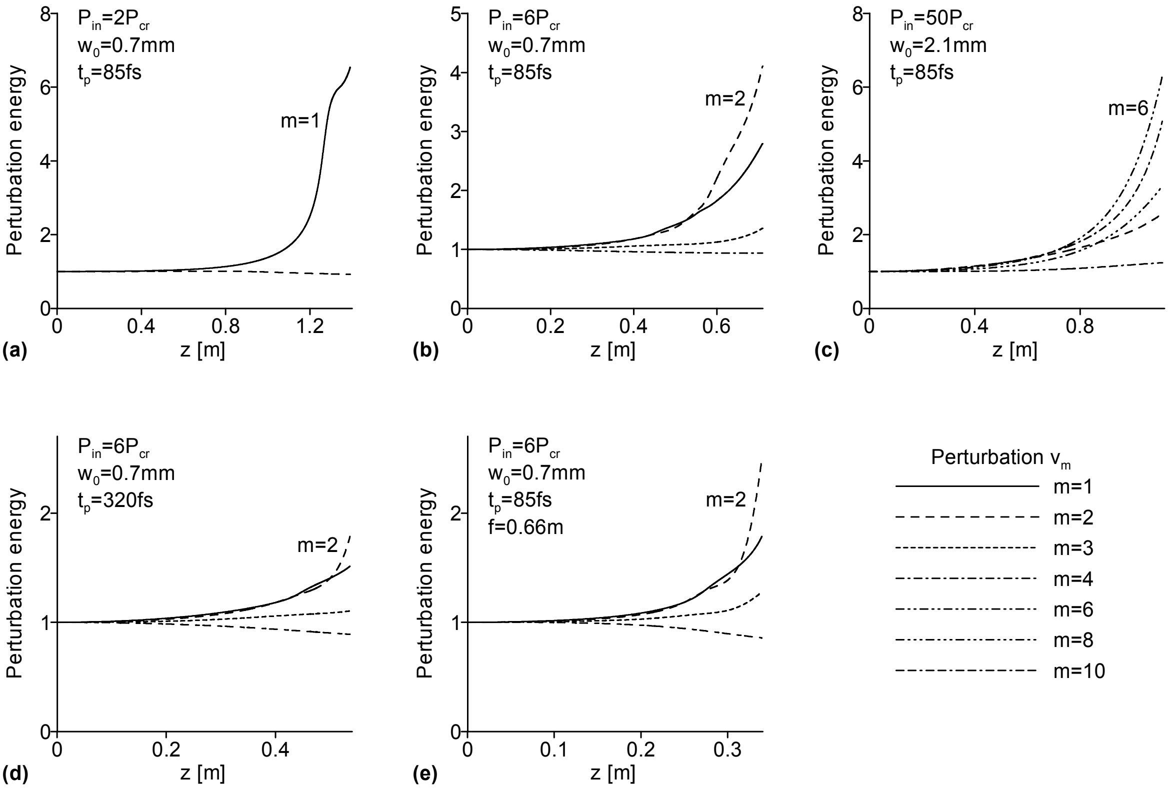

Figure 4.3.: Evolution of the energies contained in azimuthal perturbations v_m of different order for different initial field distributions. All energies are scaled to the initial ones. For sake of clarity, the (non increasing) curves of some perturbations are omitted.

slightly shorter propagation distances. The qualitative evolution of the solution is the same compared to the full model [see Figure 4.4(b)]. Since the aim of our perturbation analysis was only to show that radial solutions become azimuthally unstable, the above simplifications are justified.

Apart from showing the existence of such azimuthal instabilities, it is possible to draw some conclusions on their origin. As mentioned before, we can roughly distinguish three propagation stages of the femtosecond pulsed beam. First, we have the Kerr stage, then the plasma regime and finally diffraction. Since we treat the azimuthal perturbations with linearized equations, it does not make sense to propagate far beyond the point where we observe any perturbation growing: Equation (4.3) is valid for $|v_m| \ll |\mathcal{E}_R|$ only. Figure 4.3 shows that perturbations grow already in the Kerr stage, where we have no plasma at all. This rises the question if only the optical Kerr effect is responsible for the observed instabilities, or if the generated plasma has additional influence.

In contrast to experiments we can simply switch off the plasma generation in our

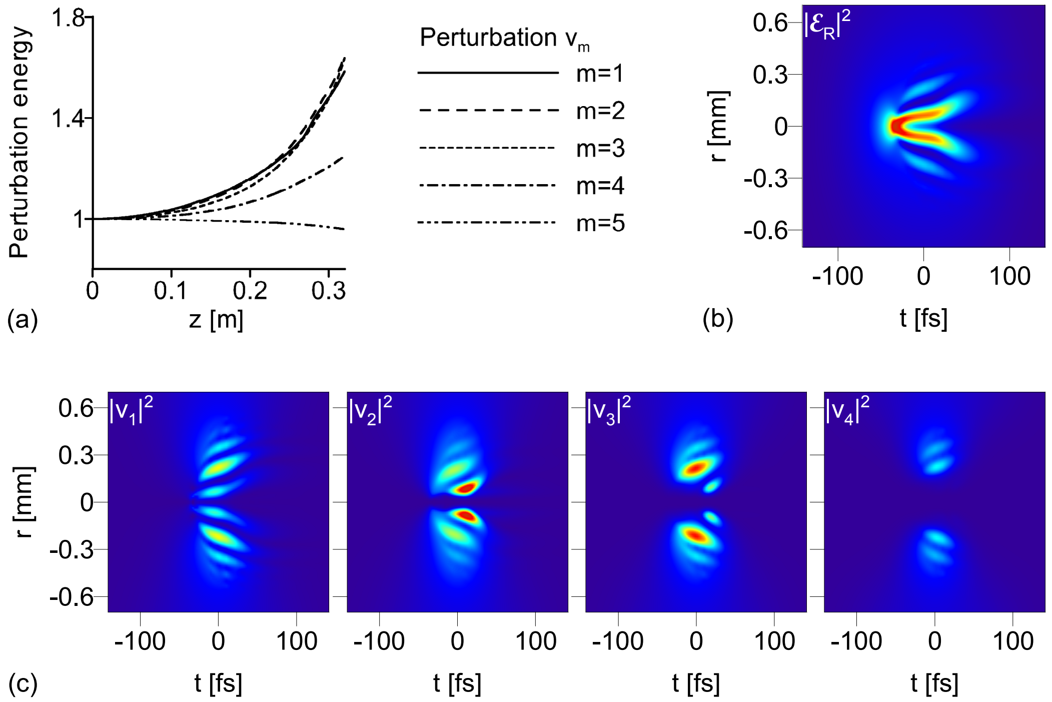

Figure 4.4.: (a) Evolution of the energies contained in azimuthal perturbations v_m of different order for different nonlinearities ($P_{in} = 10P_{cr}$, $w_0 = 0.7$ mm, $t_p = 85$ fs); all energies are scaled to the initial ones. (b) Intensity distribution of the rotationally symmetric solution at 32 cm, shortly after the onset of plasma generation. (c) Intensity distributions for the azimuthal perturbations at the same propagation distance.

numerics. Hence, we can compare our results to those obtained with a system where $\rho_e \equiv 0$. Unfortunately, then we find collapsing solutions for input powers above P_{cr}, since the defocusing effect of the generated plasma is missing. In order to work around this, we consider a saturable Kerr nonlinearity as $|\mathcal{E}|^2 / \left(1 + |\mathcal{E}|^2 / I_s\right)$ instead of $|\mathcal{E}|^2$ in Equation (2.53a), but still neglect any plasma generation. Here we choose a saturation intensity $I_s = 4 \times 10^{13}$ W cm^{-2} which is a typical value for the intensity inside the filament we observed in simulations using the full model.

If we compare Figures 4.4(a) and 4.5(a), the growth rates achieved with the model including plasma generation and those obtained from the one with saturable Kerr nonlinearity are almost the same. Hence, we can conclude that the optical Kerr effect is the origin of these azimuthal instabilities. Indeed, beam break-up in Kerr media is a well known phenomenon initiated by such instabilities [63–65]. For a pure Gaussian beam shape, the Kerr effect favors the whole-beam collapse to the detriment of modulational instability (MI). When saturation is added – whatever it may be – filaments are in contrast easily generated even with Gaussian beams. However, for a beam yielding a ring-like (diffraction) pattern (e.g., super-Gaussian), MI is able to

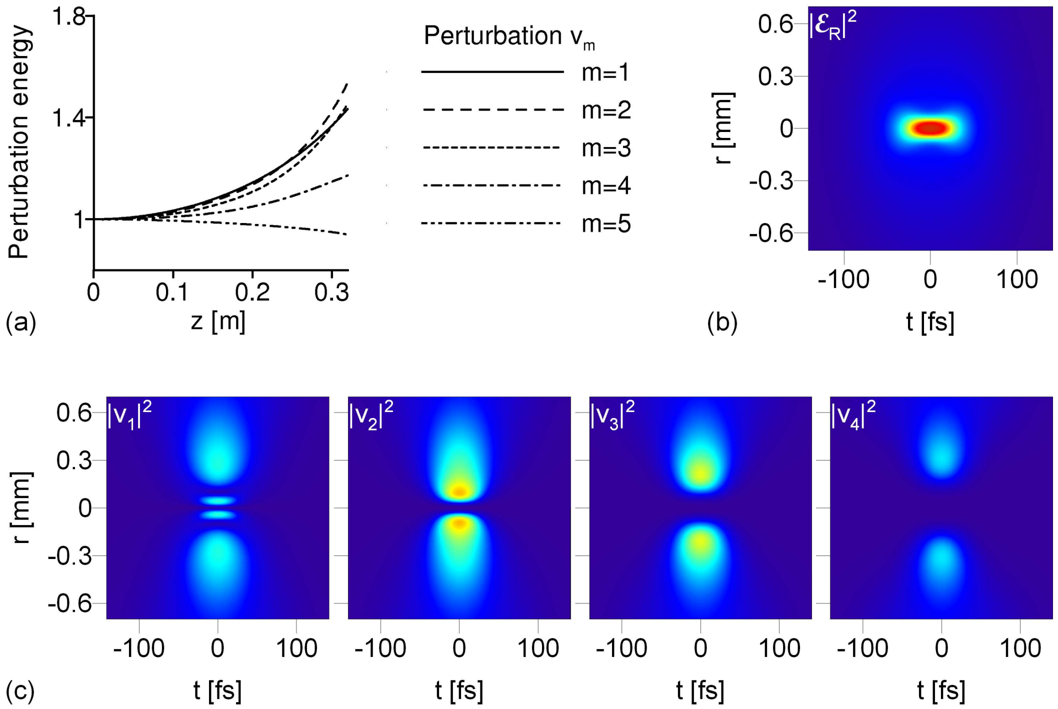

Figure 4.5.: Same as Figure 4.4, but without plasma generation and saturable Kerr nonlinearity $|\mathcal{E}|^2 / \left(1 + |\mathcal{E}|^2 / I_s\right)$.

form genuine filaments well before the saturation stage (see, e.g., [27]).

So what is the influence of the generated plasma? First of all, it produces a strong asymmetry in time in the rotationally symmetric solution [Figure 4.4(b)], which is absent in the saturable Kerr case [Figure 4.5(b)]. Apart from that, if we have a closer look at the actual field distributions of the perturbations and compare the model including plasma [Figure 4.4(c)] and the saturable Kerr case [Figure 4.5(c)], we see that the generated plasma affects the perturbations via the evolution of the rotationally symmetric solution $\mathcal{E}_R$. Especially for small m's the plasma redistributes the perturbations. In small areas we get a faster growing perturbation than in the case of a pure saturable Kerr nonlinearity (e.g. for $m = 2$ at the trailing edge of the pulse in Figure 4.5).

Another interesting result of the stability analysis is the following: Both Figures 4.4(c) and 4.5(c) show that the higher the vorticity m of the perturbation the lesser is the influence on the core region of the filament (~ 150 μm). On the other hand it is obvious that these perturbations are the ones responsible for multiple filamentation. Hence we can conjecture that multiple filamentation has its origin already in the Kerr stage, where the beam diameter is large. In contrast, a single filament, once formed, should be relatively robust and not easily split into several spots.

4.2. Multiple filamentation of femtosecond pulsed beams

In contrast to the previous section, we here treat pulsed beams which decompose into several "hot spots" in the self-channeling regime. As mentioned before, we introduce a time-averaged (2D+1)-dimensional model. Section 4.2.1 is devoted to the derivation of the reduced (2D+1)-dimensional model and to the analysis of its soliton-like solutions. Emphasis is put on soliton interactions in conservative regime and on the action of multi-photon absorption (MPA) which damps the soliton profiles and decreases their power over a generic distance. In spite of natural limitations owing to the averaging in time, the spatial dynamics described by this model is found to be qualitatively close to that provided by the original (3D+1)-dimensional equations. Direct comparisons between both models are commented in Section 4.2.2, where the limits of applicability for the 2D reduction are thoroughly discussed. Differences between an averaged-in-time filament compared with its (3D+1) counterpart developing a two-peaked temporal profile [32, 34] are discussed. Section 4.2.3 concerns experimental observations of filaments evolving from TW pulses delivered by the Teramobile facility. By means of classical CCD imaging, the filamentation figures are collected over regular distances upon the propagation axis. They emphasize the early amplification of the initial beam defects. These defects then serve as central "hot" spots around which short-scale light cells arise and rapidly recur over one meter-range distances. The local zones formed by a central spot surrounded by short-living cells are able to propagate much farther and meet the definition of an "optical pillar" given above. The qualitative events developed in the experimental patterns are shown to agree with numerical computations realized from the 2D reduced model, using a digitized file of the experimental input beam profile. Different input powers comprised between 100 and 1000 times P_{cr} are investigated for collimated beams. A special experiment involving a focused beam achieves to confirm both the validity of the 2D model and the existence of "optical pillars".

4.2.1. The time-averaged model

Current limitations of even the most modern, massively-parallel computer machines still prevent us from accessing a complete description of a km-range propagation of broad, cm-waisted beams as a whole, in reasonable CPU times. For, e.g., a beam waist of about 2.5 cm only and a pulse duration $\sim$ 100 fs, the appropriate resolution would require at least 2^{37} mesh points for numerical box lengths in (x, y, t) of

15×15 cm^2 and 600 fs, respectively. In addition, it is often necessary to employ an adaptively-refined step along z able to resolve correctly the sharp peaks coupled to narrow plasma channels with a size $\sim 50\mu$m, emerging along the filamentation process (see also Appendix B). Numerical simulations fulfilling these needs consume several Terabytes in memory for a single run, which we have to avoid. For this reason, we may alternatively derive a reduced model from the original (3D+1)-dimensional equations. This model amounts to reducing the number of effective dimensions by freezing suitably the temporal dependencies of the wave-field. Even though this reduction is primarily motivated by technical constraints, it also allows us to gain a deeper insight into the transverse dynamics of the filamentation phenomenon.

4.2.1.1. Derivation

To establish the time-averaged model, we first apply some preliminary approximations. Considering sub picosecond durations, avalanche ionization and related plasma absorption have a weak influence on the pulse dynamics for the parameters examined below and we thus ignore them ($\sigma = 0$). We can also omit group-velocity dispersion, whose physical coefficient $k'' = 0.2$ fs^2/cm makes it too weak for being a key-player competing with ionization of air molecules over filamentation distances limited to 100 m. Moreover, our main focus is not temporal but spatial dynamics. The numerical results from Section 4.1 show that femtosecond filaments result from the competition between Kerr self-focusing and multi-photon ionization (MPI). We thus assume that MPI mainly balances Kerr self-focusing at a time slice $t \simeq t_c(z)$ where a dominant spike with temporal extent T emerges in the pulse temporal profile. This duration T is conjectured to keep the same order of magnitude along propagation. Therefore, we decompose $\mathcal{E}$ as follows:

$$\mathcal{E}(x,y,z,t) = \psi(x,y,z) \times \chi[t, t_c(z)], \tag{4.4}$$

where the temporal distribution for the highest-intensity peak is modeled by the Gaussian

$$\chi[t, t_c(z)] = \mathrm{e}^{-\frac{[t-t_c(z)]^2}{T^2}}. \tag{4.5}$$

Under the previous assumptions, we can plug the above expression of $\mathcal{E}$ into Equations (2.53). Immediately we can solve Equation (2.53c) and get for the electron density

$$\rho_e = \sqrt{\frac{\pi}{8K}} T \sigma_K \rho_{nt} |\psi|^{2K} \left\{ \mathrm{Erf}\left[\frac{\sqrt{2K}[t-t_c(z)]}{T} \right] + 1 \right\}. \tag{4.6}$$

Here Erf denotes the usual error function $\mathrm{Erf}(x) = 2\int_0^x \exp(-t^2)dt/\sqrt{\pi}$. For the averaging in time, we integrate Equation (2.53a) over the entire time domain after multiplying it by χ. The resulting equation for ψ reads:

$$\frac{\partial\psi}{\partial z} = \frac{i}{2k_0}\Delta_\perp\psi + i\alpha k_0 n_2|\psi|^2\psi - i\gamma|\psi|^{2K}\psi - \frac{\beta^{(K)}}{2\sqrt{K}}|\psi|^{2K-2}\psi, \tag{4.7}$$

where $\alpha = (1-\theta+\theta D/\sqrt{2}\tau_K)/\sqrt{2}$, $\gamma = \sqrt{\pi/8K}Tk_0\sigma_K\rho_{nt}/2\rho_c$ and

$$D = \int_{-\infty}^{+\infty} \mathrm{e}^{\frac{T^2}{8\tau_K^2}-\frac{u}{\tau_K}-\frac{2u^2}{T^2}} \left[\mathrm{Erf}\left(\frac{\sqrt{2}u}{T} - \frac{T}{\sqrt{8}\tau_K}\right)+1\right] du.$$

The integral D follows from averaging in time the delayed Kerr component. Equation (4.7) describes the transverse dynamics of fs beams, with appropriate coefficients α, γ keeping the trace of averaged variations in time of the pulse. It is worth noticing that this model does not depend on the longitudinal location of the time slice $t = t_c(z)$. This is a pleasant property since we know that the dominant spike moves due to the dynamic spatial replenishment mechanism [see Section 4.1.1]. The only arbitrariness is the choice of the peak duration T. On one hand, a natural assumption would be to opt for T equal to the characteristic pulse length t_p, i.e., an ionization front raises from a wave structure with mean duration comparable to that of the input pulse. For example, for a pulse length $t_p = 85$ fs and a nonlinear delay time $\tau_K = 70$ fs, this choice leads to $D \simeq 0.707t_p$ and $\alpha \simeq 0.57$. On the other hand, there exists evidence [34, 66] that MPI can shorten pulses to mean duration reaching 1/10 of their initial values. Setting $T = 0.1t_p$ with $t_p = 85$ fs then provides the coefficients $D = 0.117t_p$, so that $\alpha = 0.39$. Note from these estimates that the global effect of the delayed Kerr component is to increase the effective power for self-focusing to some extent. This property may explain former experimental observations [10, 18], following which powers above three times P_{cr} are often necessary to create one localized filament. Because we wish to describe filamentation patterns in full ionization regime, we henceforth assume $T = t_p/10$. This value was found to provide the best approximations of fluence patterns developed by (3D+1)-dimensional fs pulses.

Let us now discuss inherent properties to Equation (4.7), before proceeding on comparisons of this 2D approach with direct simulations of Equation (2.53).

4.2.1.2. Soliton-like Dynamics

For technical convenience, we transform Equation (4.7) into a dimensionless system of units, which is employed in this subsection only. By introducing the rescaled propagation variable $Z = z\left[(\alpha k_0 n_2)^K/\gamma\right]^{1/(K-1)}$, the rescaled transverse coordinates$X = x\sqrt{2k_0}\left[(\alpha k_0 n_2)^K/\gamma\right]^{1/(2K-2)}$ and $Y = y\sqrt{2k_0}\left[(\alpha k_0 n_2)^K/\gamma\right]^{1/(2K-2)}$, the rescaled field envelope $A = \psi\,(\gamma/\alpha k_0 n_2)^{1/(2K-2)}$ and the parameter in front of the losses $\nu = (\beta^{(K)}/2\sqrt{K})\left(\alpha k_0 n_2 \gamma^{K-2}\right)^{1/(1-K)}$, it is straightforward to rewrite Equation (4.7) in the form

$$\frac{\partial A}{\partial Z} = i\Delta_\perp A + i|A|^2 A - i|A|^{2K} A - \nu |A|^{2K-2} A, \tag{4.8}$$

where $\Delta_\perp = \partial_X^2 + \partial_Y^2$ and the parameter ν takes the value $\nu = 0.154$ with the above choices of $\alpha = 0.39$, $t_p = 85$ fs and $T = t_p/10$. This change of variables and fields fixes the saturation intensity $[I_{max} = |\psi|^2_{max} = (\alpha k_0 n_2/\gamma)^{1/(1-K)}]$ to unity $[|A|^2_{max} = 1]$. This saturation intensity realizes an equilibrium between Kerr and MPI nonlinearities.

Conservative case $\nu = 0$: In the non-dissipative regime ($\nu = 0$), Equation (4.8) admits soliton solutions in the form $A = \phi(X,Y)\exp(i\Lambda Z)$, where the soliton shape ϕ is real-valued and satisfies

$$-\Lambda\phi + \Delta_\perp\phi + \phi^3 - \phi^{2K+1} = 0. \tag{4.9}$$

Here, we restrict ourselves to the single-hump, node-less ground state soliton solution. Figures 4.6(a-c) show the basic properties of this soliton family characterized by its power P_s, i.e., the power $P = \int |A|^2 d\vec{R}$ computed using the shape ϕ, its maximum amplitude ϕ_{max} and full width at half-maximum (FWHM) over the soliton parameter Λ. Low-power solitons are close to the Townes mode of the cubic NLS equation [corresponding to $|A|^2 \gg |A|^{2K}$ in Equation (4.8)], with power $P_{Townes} = 11.7$ and a spatial shape close to a Gaussian beam [4] (see Section 3.2.1). High-power ones exhibit a shape resembling high-order super-Gaussian beam. Their respective intensity ϕ^2_{max} is always below (although close to) the saturation threshold $I_{max} = 1$.

An important feature is the monotonous increase of P_s versus Λ, which indicates linear stability of these nonlinear objects, in accordance with the so-called Vakhitov-Kolokolov criterion $dP_s/d\Lambda > 0$ [67, 68] (see also Refs. [9, 69, 70]). Figure 4.6(d) confirms the stability of such stationary-wave structures from a numerical computation of azimuthal perturbations $\delta\phi \sim \exp(im\theta + i\lambda Z)$ acting on the ground state ϕ, with angular number m and eigenvalue λ (see details on the related spectral problem in Appendix A.4). First, we observe that all eigenvalues λ are real-valued, so this family of solitons is linearly stable. Second, in the parameter range $0.16 < \lambda < 0.29$ ($1.05 < P_s/P_{Townes} < 3.2$ resp.) there are no internal modes, i.e., breather modes characterized by periodic oscillations in their amplitude. Therefore, in this regime we expect the solitons to be particularly robust due to the lack of internal oscilla-

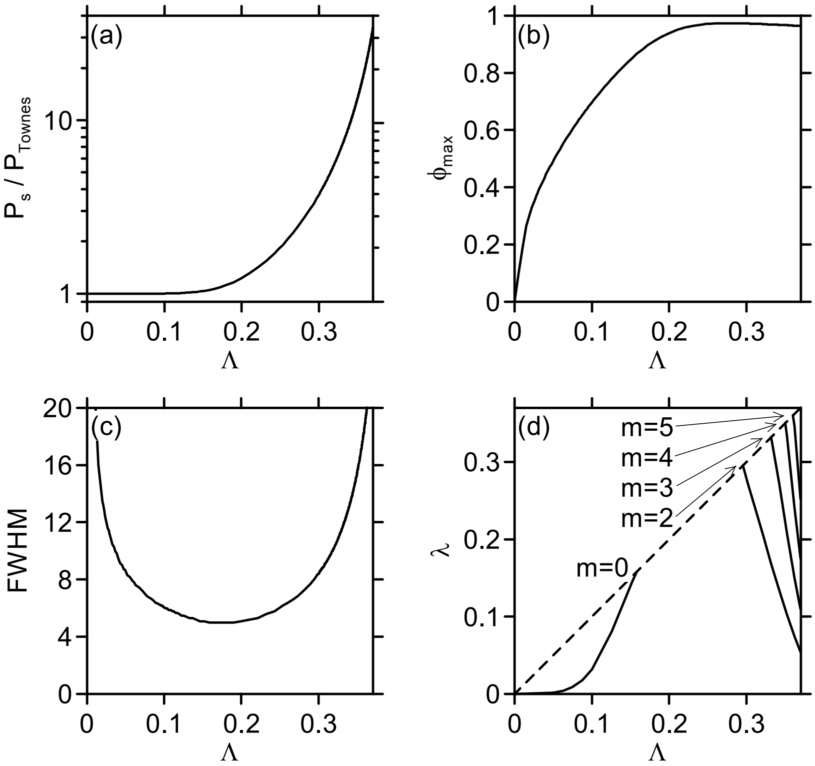

Figure 4.6.: (a) Soliton power versus Λ, (b) soliton amplitude versus Λ, (c) soliton width versus Λ, (d) eigenvalues of the internal modes $\delta\phi$ versus Λ. The dashed line marks the maximum value of λ for which discrete (localized) perturbative modes exist, i.e., $\lambda \leq \Lambda$.

tions. The corresponding FWHM and intensity maxima expressed in physical units are $150 - 200$ μm and $4 - 8 \times 10^{13}$ W/cm^2, which is in excellent agreement with the usual diameter and intensities reached by femtosecond filaments in air [30,32,33].

Solitons are strong nonlinear attractors. Starting with any low intensity field distribution containing sufficient power, self focusing always leads to the formation of one or more solitons. Another consequence of this dynamics is that these objects attract each other and may fuse. Figure 4.7 shows iso-intensity plots of the merging of two identical solitons with individual power P_s, soliton parameter Λ and separation distance Δ.

From the above analysis, we expect solitons with powers $1.05 < P_s/P_{Townes} < 3.2$ to be specifically robust (absence of internal modes). Indeed, for fixed $\Delta = 15$, solitons without internal modes [Figure 4.7(b)] merge at larger distances Z_{fus} than those capable of internal oscillations [Figures 4.7(a,c)]. Moreover, if we look at the final states after the fusion processes, only in Figure 4.7(a) a robust, new fused static waveguide emerges, starting from $2P_s/P_{Townes} \simeq 2 < 3.2$. In Figures 4.7(b,c), the opposite condition $2P_s/P_{Townes} > 3.2$ leads to “breathing” solutions due to the internal

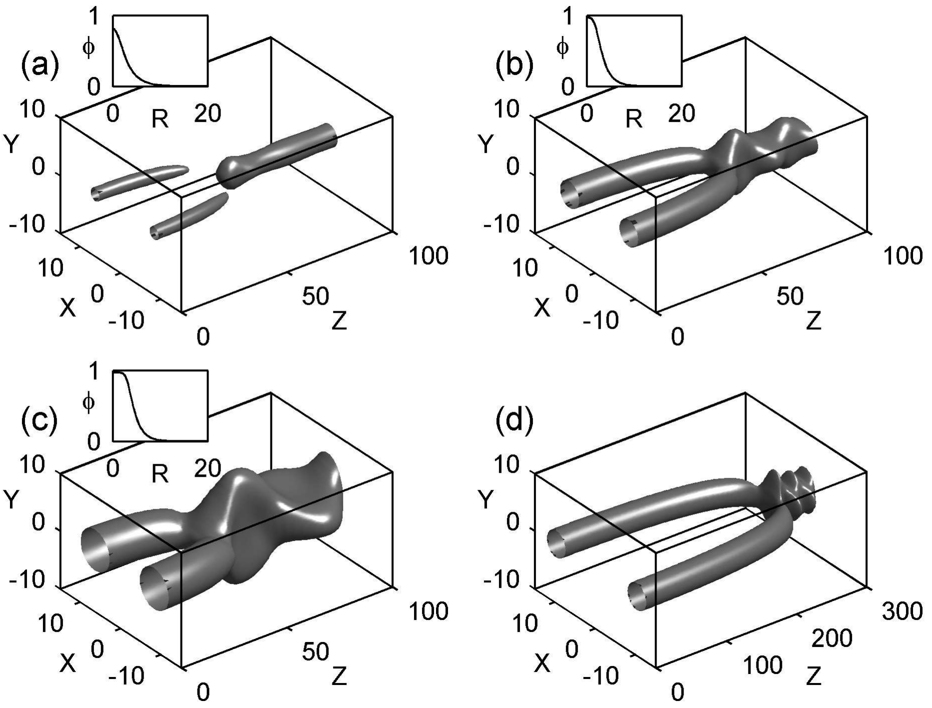

Figure 4.7.: Iso-intensity plots [$I_{iso} = 0.5$] of the fusion of conservative solitons ($\nu = 0$) with individual power P_s and separation distance Δ. The insets show the radial shape of the respective soliton. (a) $P_s = 1.02 P_{Townes}$ ($\Lambda = 0.137$) and $\Delta = 15$, $Z_{fus} = 45$. (b) $P_s = 1.92 P_{Townes}$ ($\Lambda = 0.254$) and $\Delta = 15$, $Z_{fus} = 55$. (c) $P_s = 3.84 P_{Townes}$ ($\Lambda = 0.302$) and $\Delta = 15$, $Z_{fus} = 35$. (d) Same parameters as in (b), but with $\Delta = 20$, $Z_{fus} = 250$.

mode with $m = 2$. For an increased separation, $\Delta = 20$, the point of fusion shifts to significant higher values of Z [Figure 4.7(d)]. Reexpressed in physical units, two filaments separated from each other by a distance ~ 0.6 mm can propagate over more than 3 m before merging.

Dissipative case $\nu \neq 0$: When multiphoton absorption (MPA) is introduced, Equation (4.8) no longer admits stationary solutions. Nevertheless, especially for $\nu \ll 1$, the system still holds certain features, deducible from the conservative case. First, for intensities far below the threshold ~ 1, the dissipative term is irrelevant anyway. So, in the self-focusing regime, formation of “solitons” can proceed as without losses. After reaching a “quasi-soliton” state with an intensity ~ 1, dissipation comes into play. Since there exists a conservative ground state for all $P_s \geq P_{Townes}$, the “quasi-soliton” slides “adiabatically” down the curve in Figure 4.6(a) until reaching the effective collapse threshold P_{Townes} of the cubic Schrödinger equation. Figure 4.8(a) shows this property for different powers of the initial soliton. Due to their “flat top” shape, high-power ground states undergo higher losses. As a consequence, starting with high power

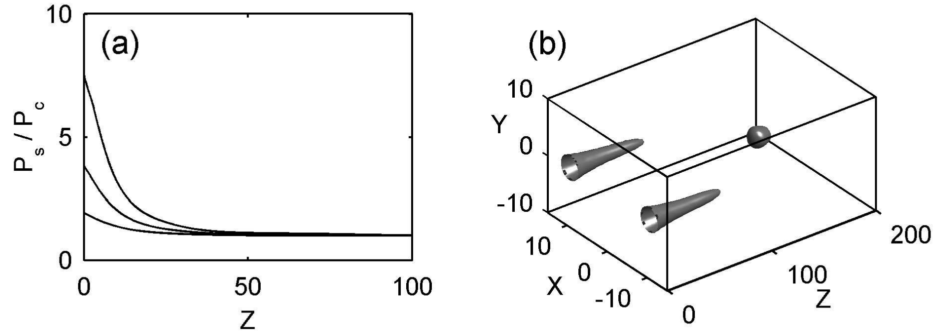

Figure 4.8.: (a) Decrease of soliton power P_s versus Z, $\nu = 0.154$, for solitons with $P_s = 1.92P_{Townes}$ ($\Lambda = 0.254$), $P_s = 3.84P_{Townes}$ ($\Lambda = 3.02$) and $P_s = 7.56P_{Townes}$ ($\Lambda = 3.32$). (b) Same as in Figure 4.7(d), but with $\nu = 0.154$, $Z_{fus} = 150$. In the region $100 < z < 150$ preceding the fusion event, beam components slightly diffract with an intensity going below the selected iso-intensity level [$I_{iso} = 0.5$].

does not significantly enlarge the dissipation range, which was found numerically less or equal 70 for input powers up to $20P_{Townes}$. Reexpressed in physical units using the above parameters α, t_p and T, this value predicts a maximum filament length < 1 m per pulse. This value agrees with the length of a single focusing cycle of the dynamic spatial replenishment mechanism recalled in Section 4.1.1.

Modeling the solitons ϕ close to the saturation threshold as $\phi = \exp[-(R/W_{fil})^{2N}]$ with an arbitrary $N \geq 1$, it is possible to solve approximately the power relation $d_z P_s \simeq -2\nu \int \phi^{2K} d\vec{R}$. By using $\int \phi^{2K} d\vec{R} = K^{-1/N} \int \phi^2 d\vec{R} = K^{-1/N} P_s$, we can evaluate the dissipation range ΔZ_{MPA}, along which the beam power persists above P_{Townes}, as

$$\Delta Z_{MPA} = \frac{K^{1/N}}{2\nu} \log \frac{P_{in}}{P_{Townes}}, \tag{4.10}$$

where P_{in} is the initial soliton power. This estimate takes the value $\Delta Z_{MPA} \approx 75$ when $P_{in} = 20P_{Townes}$, which is reasonable upper limit for the power contained in a single filament, and $N \to 1$. In physical units, Δz_{MPA} predicts a maximum filament length of ~ 1 m, which is in the same order of magnitude as our numerical result.

Last but not least, dissipation has a significant influence on the fusion dynamics. By comparing Figure 4.8(b) to Figure 4.7(d), we see that the presence of MPA promotes the mutual coalescence of filaments. The point of fusion shifts to significantly smaller propagation distances. This behavior is understandable in the sense that MPA shifts the “quasi-solitons” to the low power regime $P_s < 1.05P_{Townes}$, where we expect an easier merging. Another interesting point is that the dissipation range can be enlarged with the help of the fusion mechanism. The central beam, visible in Figure 4.8(b) at

$Z \approx 150$, indeed clearly exceeds the predicted dissipation range of a single filament.

In summary, Equation (4.8) points out that spatial solitons are the natural objects modeling self-guided femtosecond filaments in the transverse plane. Although their individual range of propagation may be limited to short distances < 1 m by MPA, their capability of merging at relatively low powers enables them to propagate over more extended ranges.

4.2.2. Time-averaged versus fully space-time-resolved simulations

We return to physical units and compare results obtained using the time averaged (2D+1)-dimensional model [Equation (4.7)] with corresponding space-time resolved 3D simulations [Equations (2.53)].

4.2.2.1. (2D+1)-dimensional simulations

Figure 4.9 illustrates filamentation patterns in the 2D approximation. For visualization, we employ iso-intensity surfaces $|\psi|^2 = \text{const}$. By comparison with antecedent experimental data [22, 23], we choose as input an anisotropic Nth-order super-Gaussian beam in the form $\psi_0 = \sqrt{I_0} \exp\left[-(x^2 + 2y^2)^N / w_0^{2N}\right]$, perturbed at $z = 0$ m by an isotropic 10% random noise in amplitude and multiplied by a 10% noisy Gaussian temporal profile ($t_p = 85$ fs). The fluence distribution $[F = \int_{-\infty}^{+\infty} |\mathcal{E}(t)|^2 dt]$ of the resulting beam, divided by the integral over the squared temporal profile, is then employed as the input condition for the 2D model.

Figure 4.9(a) shows the iso-intensity plots for a perturbed beam with $N = 3/2$, a waist $w_0 = 1$ mm and $P_{in} = 20.5 P_{cr}$. The beam first forms a ring giving rise to two filaments. These merge and reform during a transient stage, before they refocus into a robust lobe at center. Intermittence in filament nucleation occurs in the early propagation stage over short ranges, which can be compared with the scenario of optically turbulent light guide proposed in [11]. However, at larger distances, the filaments relax to a single one in the (x, y) plane. This waveform does not change until it reaches the Rayleigh length ($z \to 4$ m), beyond which it diffracts slowly. Filaments reach the maximum intensity $I_{max} \sim 7 \times 10^{13}$ W/cm^2 over distances $\sim \Delta z_{MPA} < 1$ m, but they asymptotically remain captured in longer envelopes that locate "optical pillars" in the medium. By "optical pillars" we mean discrete light spots amalgamating short-living soliton-like cells that self-attract around specific points in the diffraction plane. Similar patterns of two main filaments fusing into one were observed to generically occur with different beam shapes and peak powers comprised

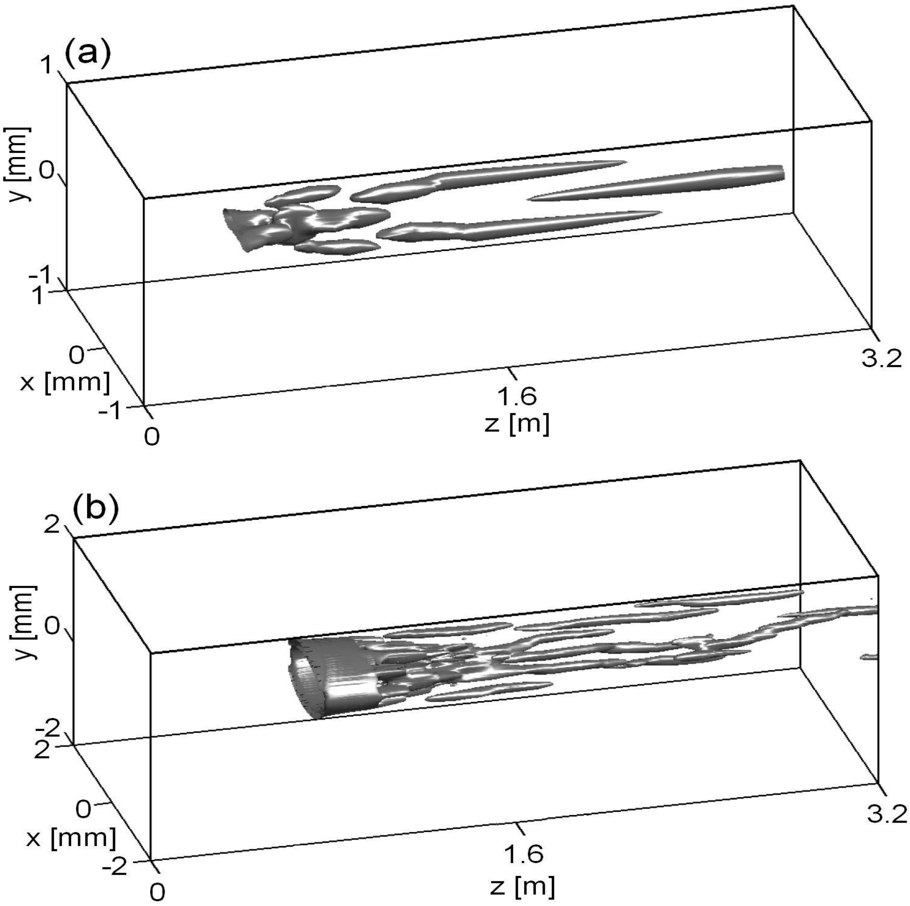

Figure 4.9.: Iso-intensity patterns ($I_{iso} \approx 10^{13}$ W/cm^2) of filamentary structures described by Equation (4.7) and created from a super-Gaussian beam with (a) $N = 3/2$, $P_{in} = 20.5\, P_{cr}$ and $w_0 = 1$ mm, (b) $N = 2$, $P_{in} = 88\, P_{cr}$ and $w_0 = 2$ mm.

between 15 P_{cr} and 40 P_{cr}. This dynamics fully agrees with previous experimental observations [22]. For higher powers, Figure 4.9(b) shows a broader ($N = 2$) super-Gaussian beam with 88 P_{cr} and wider waist $w_0 = 2$ mm. Filamentary structures with the largest separation distances create strong individual attractors, which organize the beams into long-range pillars composed of soliton-like filaments. An early stage of "random nucleation" precedes the formation of three filamentary channels, which may move in the (x, y) plane while they attempt to attain an equilibrium position.

Like the soliton pattern shown in Figure 4.8(b), these two simulations confirm that the mutual interaction between optical cells helps in maintaining the robustness of the beam envelope over several meters.

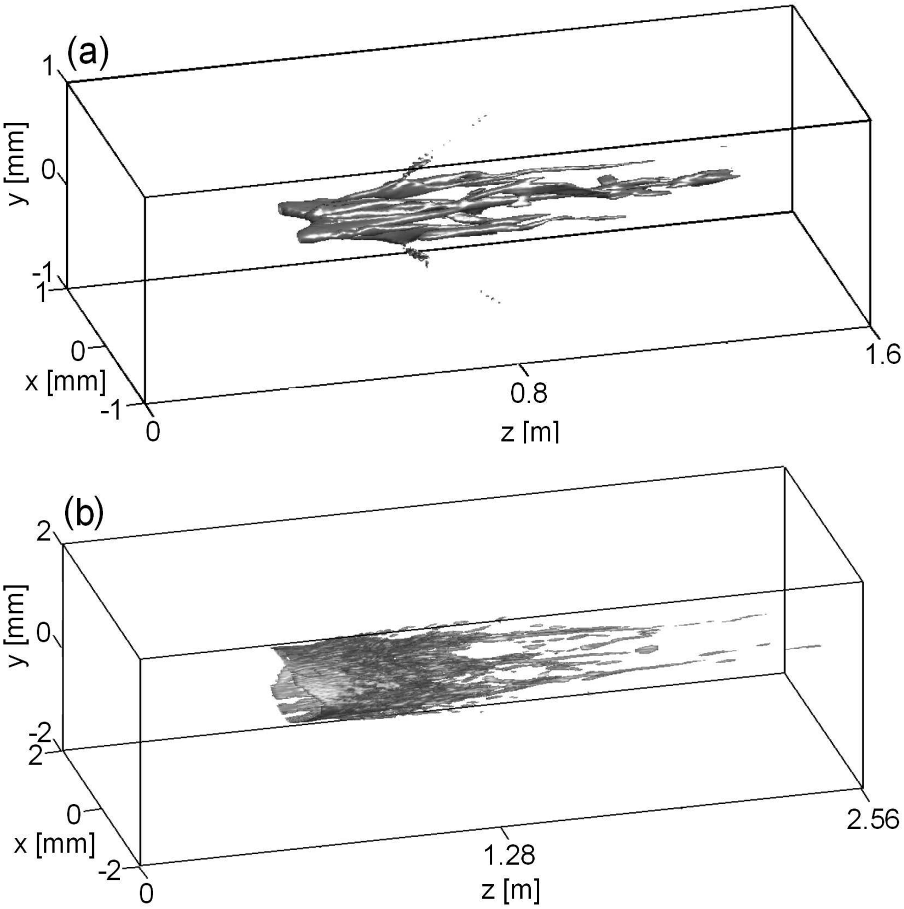

Figure 4.10.: (a) Plasma strings [$\max_t \rho(x,y,z,t) \geq 10^{15}$ cm^{-3}] of the $20.5P_{cr}$ super-Gaussian beam used in Figure 4.9(a). (b) Plasma strings from the $88P_{cr}$ super-Gaussian beam of Figure 4.9(b).

4.2.2.2. (3D+1)-dimensional simulations

For comparison, Equations (2.53) are now solved by means of a spectral code using fast Fourier transforms in the (x,y,t) variables (see Appendix B.1.3). Simulations were realized on the massively-parallel machine (TERA) of the CEA, where we used up to 128 processors per run. Details on further numerical aspects and limitations in (3D+1)-dimensional computing are given in Appendix B.2.

Figure 4.10 shows the filamentation of pulses with the same input distributions as used in Figure 4.9. In Figure 4.10(a), we display the plasma strings produced by the beam with $20.5P_{cr}$. Figure 4.11 shows their associated intensity profiles in the plane $(x, y = 0, t)$ at different z positions, along the y axis crossing the two primary spots that will merge. In the case of (3D+1)-dimensional simulations, we take into account the temporal dynamics. Filamentary structures are determined by contributions of all time-slices. Therefore, it is straightforward to use the generated

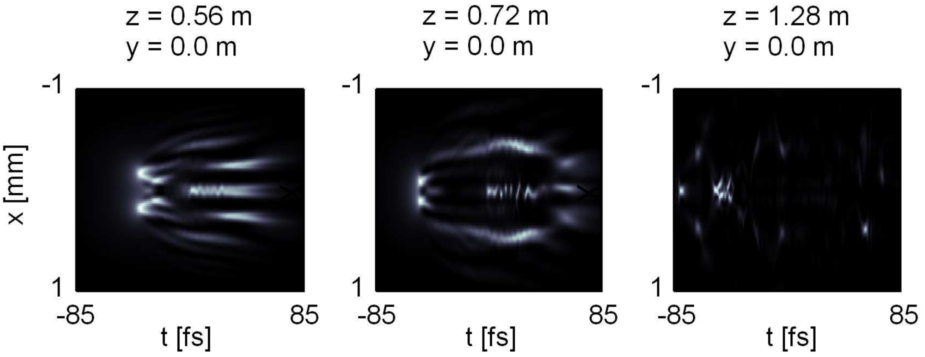

Figure 4.11.: Intensity $|\mathcal{E}|^2$ versus $(x, 0, t)$ for the beam of Figure 4.10(a).

plasma strings for identifying the filaments. The temporal pulse profile, even subject to strong distortions, does not prevent the transverse dynamics of the pulse from developing as in Figure 4.9, up to second-order discrepancies in the focus point linked to the choice of the peak duration T (see Section 4.2.2.3). Although different temporal slices come into play, all of them support the propagation of cells first nucleated at different locations, then remaining localized around the *same* place in the (x, y) plane. Plasma strings associated with pulse components of maximum intensity and duration nearby 1/10 of the input pulse dominate, which makes our previous assumption for averaging the (3D+1)-dimensional equations valid. Finally, Figure 4.10(b) depicts the plasma strings created by the super-Gaussian pulse with 88 critical powers, $N = 2$ and $w_0 = 2$ mm. Three distinct channels clearly emerge in the (x, y) plane. They do not interact significantly but remain almost robust at their transverse position, in agreement with the filamentation pattern of Figure 4.9(b).

4.2.2.3. Limitations of the time-averaged model

Major advantages in employing the (2D+1)-dimensional model concern, of course, the reduction of the computation time when we only focus on the spatial dynamics of the pulse (see Appendix B.2). Moreover, it will be employed for clearing up an alternative problem, the interaction of an ultrashort filament with an opaque droplet in Section 4.3. Experiments on this topic [30] revealed the remarkable robustness of femtosecond filaments with typical diameter $\sim 150\,\mu$m, when they hit a micrometric droplet of diameter as large as 2/3 the filament size. The collision results in a minimal loss of energy and the filament self-heals over very short distances. The interaction pattern, simulated using the full (3D+1)-dimensional system (2.53), displays evidence of the complete rebuilding of the pulse over 2 cm only. The same filament modeled by solitons of Equation (4.7) restores an identical pattern within the same interval.

Besides such convenient aspects, a time-averaging of the propagation equations cannot avoid certain weaknesses. Identifying a 3D, time-resolved filament with a 2D "soliton" means that we only focus on the core of the filament and discard its different time slices [34]. Indeed, Equation (4.7) accounts for the time slice with maximum intensity only. For describing, e.g., the self-healing of a fs filament with a micrometric droplet, this simplification has almost no effect, because the interaction length of the beam with the obstacle is short along the z axis. However, when we simulate long-range propagation, certain constrictions concerning the agreement with fully time-resolved computations have to be made:

(i) The arbitrary choice of the temporal extent $T = 0.1t_p$ prevents us from restoring quantitatively the early self-focusing distances of a beam at relatively low powers ($\leq 100P_{cr}$), as can be seen by comparing Figure 4.9 and Figure 4.10. Indeed, this choice determines the value of the parameter α [Equation (4.7)] that fixes the effective critical power in the pulse time slice under consideration. Setting $T = 0.1t_p$ suits for describing filamentation patterns evolving in ionization regimes, but this choice can lead to visible discrepancies in the location of the first focus point, for which the value $T = t_p$ yielding a higher α would be more adapted. Remembering Marburger's formula [26] that evaluates the collapse point, z_c, of collimated Gaussian beams in self-focusing regime:

$$z_c = \frac{0.367 z_0}{\sqrt{(\sqrt{\alpha P_{in}/P_{cr}} - 0.852)^2 - 0.0219}}, \tag{4.11}$$

it is seen right away that the differences in the location of the self-focus point indeed become more pronounced at low ratios P_{in}/P_{cr} and for low values of α. Here $z_0 = \pi w_0^2/\lambda_0$ is the Rayleigh length of the input beam.

(ii) Experimental setups for femtosecond pulse propagation are currently based on Chirped-Pulse Amplification (CPA) Ti:sapphire laser sources. CPA techniques allow us to modify the effective initial pulse duration by varying the distance between the gratings of the pulse compression system. These variations also entail a chirp onto the input pulse phase ($\mathcal{E} \rightarrow \mathcal{E} \exp(-iCt^2/t_p^2)$, $C =$ const), which can lead to noticeable changes in the early self-focusing distances by GVD-compensation [53, 71]. Indeed, a displacement of the first focus due to chirped pulses was observed in [S15]. Pulse chirping is used to monitor the onset of filamentation [29, 60, 72]. Since Equation (4.7) ignores the temporal dynamics, applying this model to pulses with initially-large chirped phase may then enhance the differences with the experimental observations.

(iii) Because the averaging procedure involves a single time slice only, the (2D+1)-dimensional model cannot describe a second focusing of pulses (see Section 4.1.1), which characterizes femtosecond filaments and enables the latter to pursue their propagation over about 1 m. This process allows to maintain a femtosecond filament over larger distances than those accessible by the reduced model. In connection with this point, the time-averaged model also overestimates the losses due to MPA. In fully time-resolved simulations, defocused time slices with lower intensities can maintain a nearly constant power upon propagation until they may focus again. Hence, these parts of the pulse can propagate nearly without losses. The reliability of the time-averaged model may thus be limited in, e.g., examining the post-ionization regime.

The above discrepancies should not, however, devaluate the major advantage of the time-averaged model, which can describe the qualitative dynamics of ultrashort, high-power pulses with broad waists over considerable distances of propagation.

Keeping these limitations in mind, but using the information conveyed by the 2D model, we can outline, on the basis of the previous 2D and 3D numerical results, a generic scenario for the filamentation of TW fs pulses as follows: (i) Beam modulations give rise to short-range filaments that grow in intensity until reaching the ionization threshold I_{max}. In this limit, near-soliton filaments, searching for an equilibrium position, recur in the diffraction plane within an optically-turbulent regime during the early stage of propagation [11]. (ii) As they attain a quasi-stable configuration with respect to their neighbors, short-range filaments either amalgamate or self-attract without merging, depending on their inner power and separation distances, in order to form a limited number of clusters, named as *"optical pillars"*. These optical pillars then continue the propagation over longer distances.

Note that this scenario applies to input beams where an isotropic random noise first creates short-scale cells, that next relax to quasi-coherent structures. For experimental beams exhibiting salient defects, it is not excluded that optical pillars are fixed by the most intense defects of the input beam profile, which further excite turbulent cells in their vicinity, as evidenced below (see also [S6]).

4.2.3. Time-averaged simulations versus long-range experiments

To figure out how TW laser pulses decompose into multiple filaments over long distances, we investigate some evolution stages in the filamentation patterns produced by the Teramobile laser [29, 60]. This laser system delivers at 10-Hz rate pulses with energy up to 0.5 J, transverse diameter equal to 5 cm ($w_0 \simeq 2.5$ cm), and FWHM du-

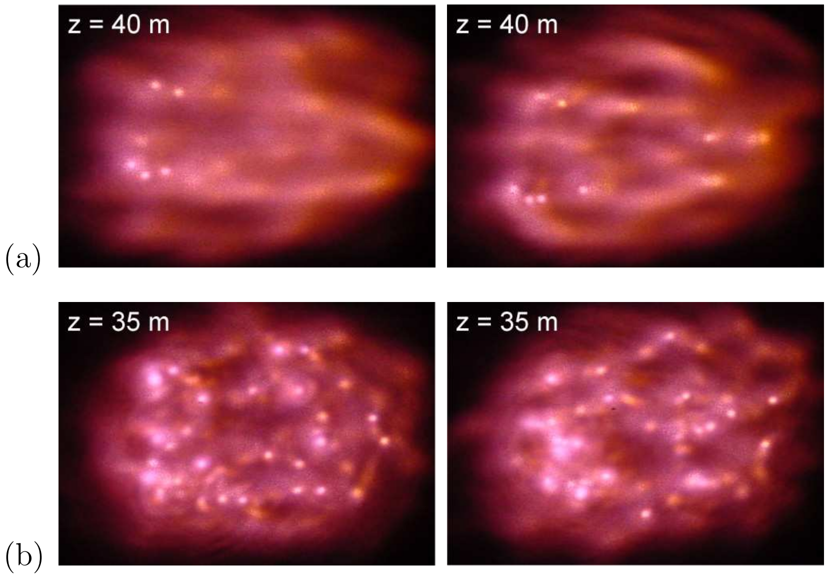

Figure 4.12.: Shot-to-shot fluctuations in the filamentation pattern of the 10-Hz rated Teramobile laser delivering 230-mJ pulses with (a) 600 fs duration ($P_{in} \simeq 120 P_{cr}$) at $z = 40$ m (b) 100 fs duration ($P_{in} \simeq 700 P_{cr}$) at $z = 35$ m. The scale of the images is about 4 cm × 3 cm.

ration tunable from 100 fs (minimal chirp) to 600 fs (large negative chirp) by detuning the compressor with a chirp opposite to air dispersion. The collected experimental data consist of photos taken from a white screen positioned in the plane orthogonal to the beam path. In the first two series of experiments [Figures (4.12-4.14)], a filter with narrow bandwidth around $\lambda_0 = 800$ nm was put in front of the camera. Two photos with exposure time of 1/8th second were taken at each distance, so that pictures mostly show single-shot beam patterns. Pictures featuring double-pulse images did not present qualitative change from shot to shot, up to slightly more visible filaments or more pronounced ones at certain distances (see Figure 4.12). Although the number of "visible" filaments may vary to some extent, the zones at which distinct clusters of filaments develop remain identical and only the relative intensity of certain spots exhibit differences. We consider these fluctuations as being of second-order importance in the global evolution of the filamentation pattern.

Concerning this point, let us emphasize that the resemblance between the experimental and numerical patterns in the forthcoming analysis will not lie in the exact position and number of the filaments, which may undergo similar fluctuations and are subject to atmospheric turbulence or local diffusive processes as they propagate. Instead, qualitative similarities occur in the following sense: Starting with a coarse input profile, the beam amplifies its initial inhomogeneities and, through modulational instability, it produces bright spots connected by lower-intensity bridges. A "global" pattern then emerges from the zones of highest concentration of light, which create characteristic figures (ring/trident/cross). These aspects are actually well restored by the time-averaged simulations, using the digitized fluence of the experimental input beam.

4.2.3.1. "Low"-power filamentation regime

To start with, we examine the filamentation dynamics of TW beams with about 100 critical powers only. Figure 4.13(a) shows the evolution of light filaments over 55 m of propagation from the Teramobile beam with 230 mJ energy and pulse duration of 600 fs. Modulations induced by caustics distributed in the spatial beam profile develop as follows: In the early propagation stage, the broad (super-Gaussian-like) beam tends to develop a ring-shaped zone by diffraction. At the edge of the beam where fluctuations are the most intense, filaments emerge from local defects. Next, several cells occur along a flattened ring inside the focal spot. More filaments are then generated around this ring. They finally self-organize into a three-pronged fork shape. For comparison, we integrated the (2D+1)-dimensional Equation (4.7) from a data file of the experimental input beam measured at the distance $d = 1$ m after the laser exit. With a pulse duration of 600 fs ($t_p \simeq 510$ fs), the coefficient α in Equation (4.7) takes the value $\alpha = 0.51$. With a beam waist of 2.5 cm, a very high spatial resolution [namely, 8192^2 in the (x, y) plane for a box length of $6w_0$] was required, in order to resolve narrow optical structures reaching 1000 times the input beam intensity I_0. Figure 4.13(b) illustrates the results of numerical simulations. The beam containing ~ 120 critical powers begins to form local clots in the highest intensity regions. Then, others emerge along a ring inside the focal spot. The final pattern, involving several small-scale spots, results in a trident-shaped figure, comparable with the experimental one. For such beams with a few tens of critical powers only, Equation (4.7) describes the filamentation of a disordered optical distribution having an effective ratio of input power over critical of about $\sim \alpha P_{in}/P_{cr} \simeq 60$, which limits at the very most to $P_{in}/P_{fil} \simeq 24$ the number of genuine filaments reaching the ionization threshold. Filaments develop as asymptotic states and become decoupled from the initial amplitude and phase of the wave-field. The discrepancy existing in the distance where the first filaments occur, $z_c \simeq 50$ m, and the experimental measurement, $z_c \simeq 30$ m, is attributed to the pulse chirping, which Equation (4.7) ignores, and to our former choice $T = 0.1\,t_p$. As underlined in Section 4.2.2.3, this value suits the experimental development of filaments in ionization regime, but it cannot restore the early self-focusing distances of the beam requiring rather $T = t_p$. Keeping $T \ll t_p$ is, however,

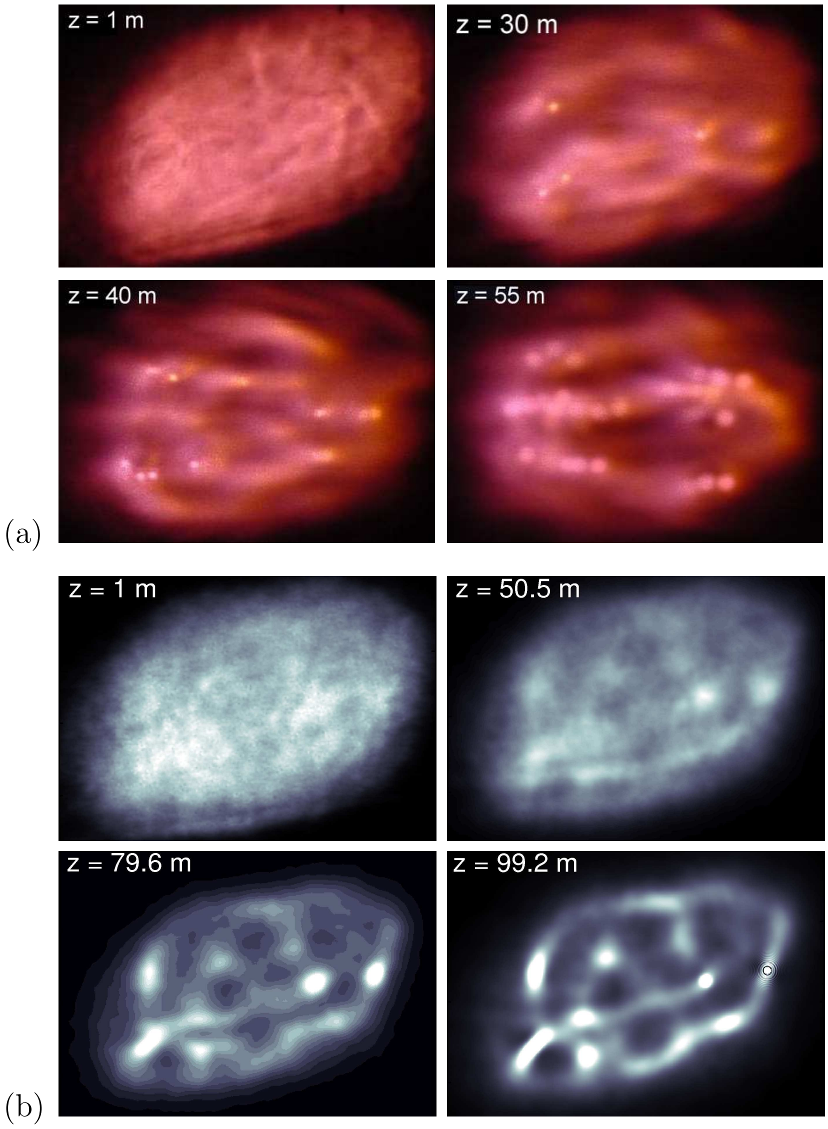

Figure 4.13.: Filamentation patterns (a) produced experimentally for the 120 P_{cr} beam at $z = 1$, 30, 40 and 55 m. (b) Numerical computations of the same beam from Equation (4.7). Maximum intensity is limited to twice the input intensity. The scale of the images is about 4 cm × 3 cm.

necessary to approach a suitable averaged power ratio in ionization regime, where filaments mostly evolve. From the numerical as well as experimental patterns, we can observe that some filamentary channels persist from the first focus point over several meters, whereas others are randomly nucleated over shorter longitudinal scales.

4.2.3.2. "Moderate"-power filamentation regimes

Reducing the pulse duration to 100 fs ($t_p = 85$ fs) makes it possible to investigate filamentary patterns promoted by fs beams with powers as high as 700 P_{cr}, i.e., 2.3

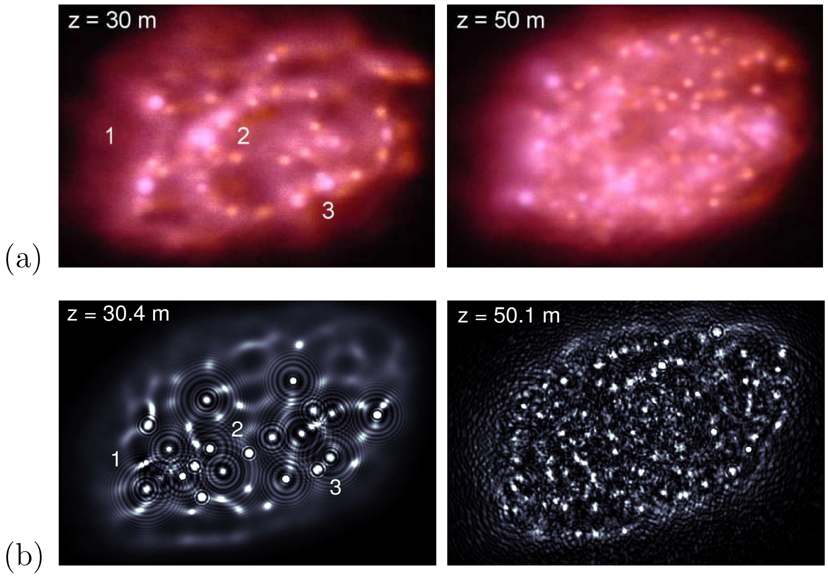

Figure 4.14.: Filamentation patterns (a) produced experimentally for the 700 P_{cr} beam at $z = 30$ and 50 m. (b) Numerical computations of the same beam from Equation (4.7). Labels (1)-(3) indicate beam zones discussed in the text. The scale of the images is about 4 cm × 3 cm.

TW. In this case displayed in Figure 4.14(a), the beam breaks up into more cells than in the previous lower-power case. Following the estimate recalled in the introduction, up to $\alpha P_{in}/P_{fil} \sim 110$ light cells may form in principle with $P_{fil} \simeq \pi^2 P_{cr}/4$. Figure 4.14(b) reproduces these experimental patterns from a numerical integration of Equation (4.7) performed with the parameter $\alpha = 0.39$ fixed by $t_p = 85$ fs. Note that the discrepancies in the early self-focusing distances signaled in the previous case almost completely disappear at higher powers. Here, a minimal pulse chirping was used. The agreement between the experimental and numerical results is thus quite satisfactory. The labels (1-3) locate active zones in the beam, which can clearly be identified in both the experimental and numerical patterns: (1) points out to a couple of bright, robust filaments, (2) restores an arch of the diffraction ring pattern supporting primary hot spots while (3) indicates a crosswise configuration of filaments. By comparing the four snapshots with those displayed in Figure 4.13, these patterns reveal that, although some filaments are able to survive over several meters at the most powerful regions of the pulse, random nucleation of filaments in the entire focal spot seems more privileged, compared with the break-up of the former 120 P_{cr} beam. We explain this property by the high power density. “Optical pillars” cannot propagate independently due to their smaller separation distance. The primary filamentary cells experience more substantial power transfers through the overall surface of the beam.

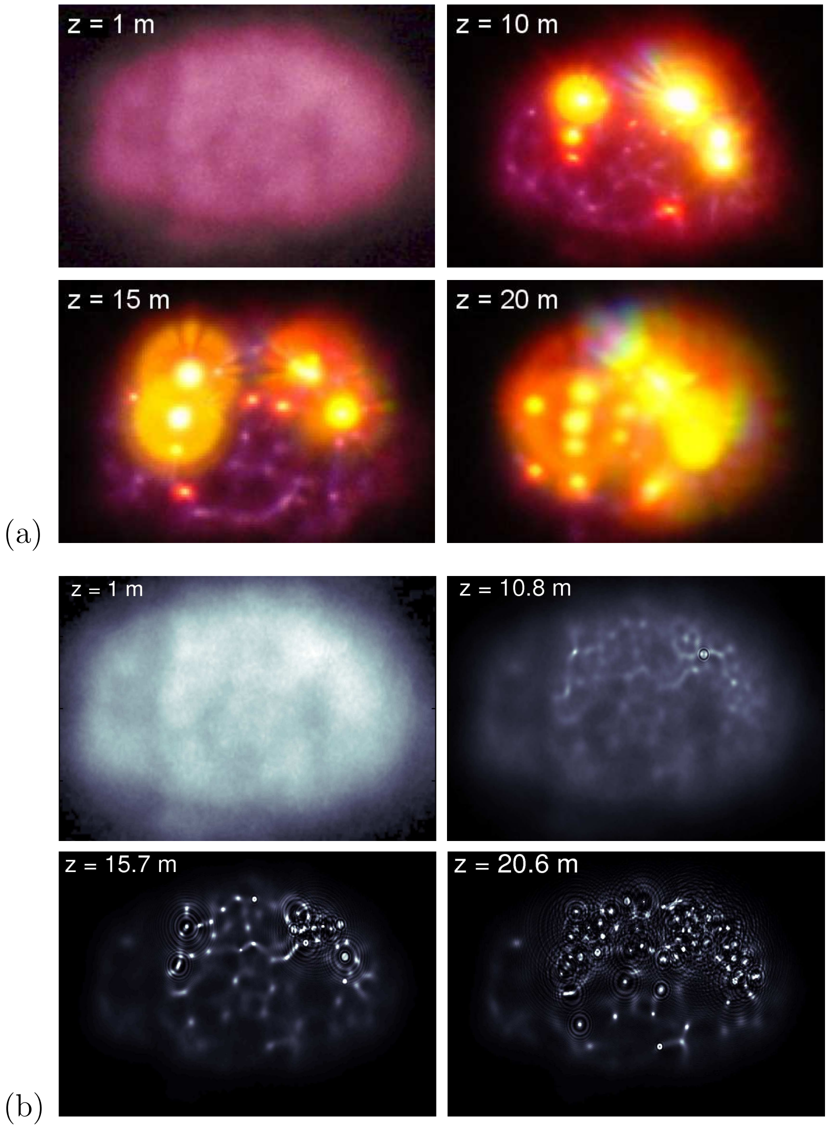

Figure 4.15.: Filamentation patterns of the 1000-P_{cr} beam delivered by the Teramobile at different propagation distances: (a) Experimental transverse distributions. (b) Image plots from numerical computations performed with Equation (4.7). The scale of the images is about 4 cm × 3 cm.

4.2.3.3. "High"-power filamentation regimes

Concerning now higher power levels, Figure 4.15(a) displays filamentation stages for pulses delivered by the Teramobile system, with a FWHM duration of 100 fs ($t_p = 85$ fs) and 330 mJ energy. The power range thus accesses 3-4 TW, i.e., about 1000 critical powers. No filter was used in this series of experiments. Although a non-trivial level of overexposure cannot be avoided from the most intense regions of the beam, removing the 800 nm filter makes it possible to exhibit true-colored filaments and to emphasize major optical pillars through the white-light conical emission which signals the presence of nonlinear self-focusing and subsequent plasma generation [29, 60, 72]. The filamentation scenario follows the former one: A ring-shaped zone supports a few big spots initiated by the highest-intense defects of the input beam. These "hot" spots self-focus more and more over several tens of meters, while white light occurs on the detection screen. The evacuation of power excess due to the collapse dynamics undergone by the primary filaments allows to transfer power to the central zone of the beam, which serves as an energy reservoir for exciting secondary filaments. Equation (4.7) computed with $\alpha = 0.39$ ($t_p = 85$ fs) restores these features with almost no discrepancy in the first focus point [$z_c \simeq 10$ m], as the beam contains very higher power. Figure 4.15(b) reproduces the experimental images in the same longitudinal interval.

From the numerical computation, the bright spots observed in the experiments appear to be first excited by an intense primary filament, which afterwards give rise to a bunch of secondary ones emerging as smaller-scale cells located near the central spot. We can observe how the local defects rapidly generate intense spots along a ring. In the upper arch of this ring, the most intense filaments, either as individual entities or gathered in clusters of few cells, produce ~ 4 distinct active zones, in agreement with Figure 4.15(a). These zones actually consist of robust optical pillars, following the definition given above. They persist over several tens of meters, whereas secondary filaments rapidly recur first around them, next in the central part of the beam.

Figure 4.16 details the spatial distortions undergone by the lowest ($120\,P_{cr}$, top row) and highest ($1000\,P_{cr}$, bottom row) power beams, computed with the 2D reduced model. It displays evidence in both cases of the early amplification of the initial beam defects, which serve as central spots around which short-living filaments develop into an optical pillar. Note the growth of intense spikes that remain in self-focused state over several tens of meters, while secondary peaks attain similar intensities at later distances.

4.2.3.4. "Moderate"-power beams in focused geometry

While the previous observations on screens provided detailed information about the beam structure at a given distance, they were, however, limited to semi-qualitative observations. Fluctuations in the initial beam as well as from the atmosphere let the profile vary from shot to shot (see Figure 4.12), so that successive images at different distances cannot be taken as quantitative information providing a complete propagation sequence over long distances. Moreover, the continuity and length of the individual filaments could not be assessed with accuracy.

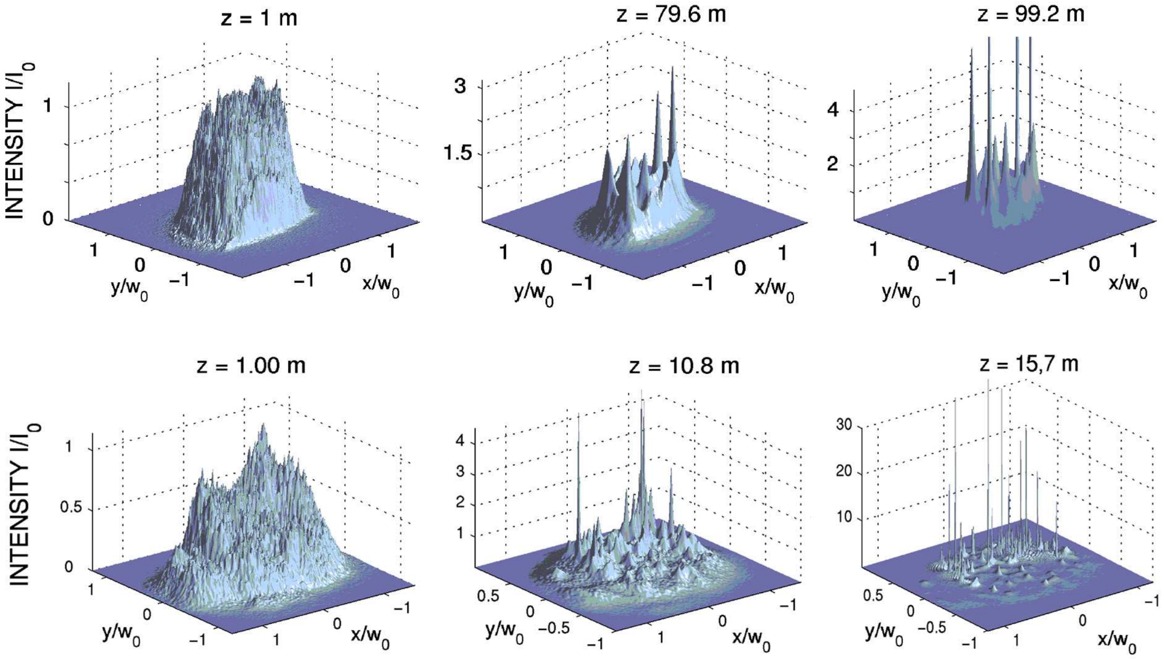

Figure 4.16.: Intensity versus (x, y) for the beams shown in Figure 4.13(b) (top row) and Figure 4.15(b) (bottom row).

In order to circumvent this limitation, we used a spatially extended, single shot characterization of the beam profile. The Teramobile laser was slightly focused ($f = 40$ m) from a larger beam waist ($w_0 \simeq 5$ cm) and emitted an energy of 250 mJ in 100 fs pulses (2.5 TW, 760 P_{cr}). It was installed outdoors on a flat humid ground and shot against the wind direction into an aerosol generator producing a thin haze at a distance of 48 m from the laser exit. With a soft regular wind, this setup produced a pretty homogeneous light haze along a distance of up to 10 m towards the laser beam. The haze density was adjusted so that beam scattering was efficient enough to detect the filaments, with limited perturbation on the beam propagation itself. In those conditions, image blurring by multiple scattering was negligible [30]. The beam was imaged with a CCD camera in true colors, from a near-forward direction. More precisely, the CCD camera was placed over the aerosol generator, about 25 cm above the center of the laser beam, and directed to the laser output of the Teramobile system. This setup allowed for the first time to acquire single shot (exposure time 1/8 s) pictures of a long section (up to 10 m) of the beam (Figure 4.17). Triangulation, calibrated with reference points along the laser path, enabled us to retrieve the distance calibration indicated in Figure 4.17. Note that the beam was imaged with a very strong parallax, since the camera was placed at only 25 cm above it. Hence, the triangulation yielding the distance scale is not linear and explains the apparent short

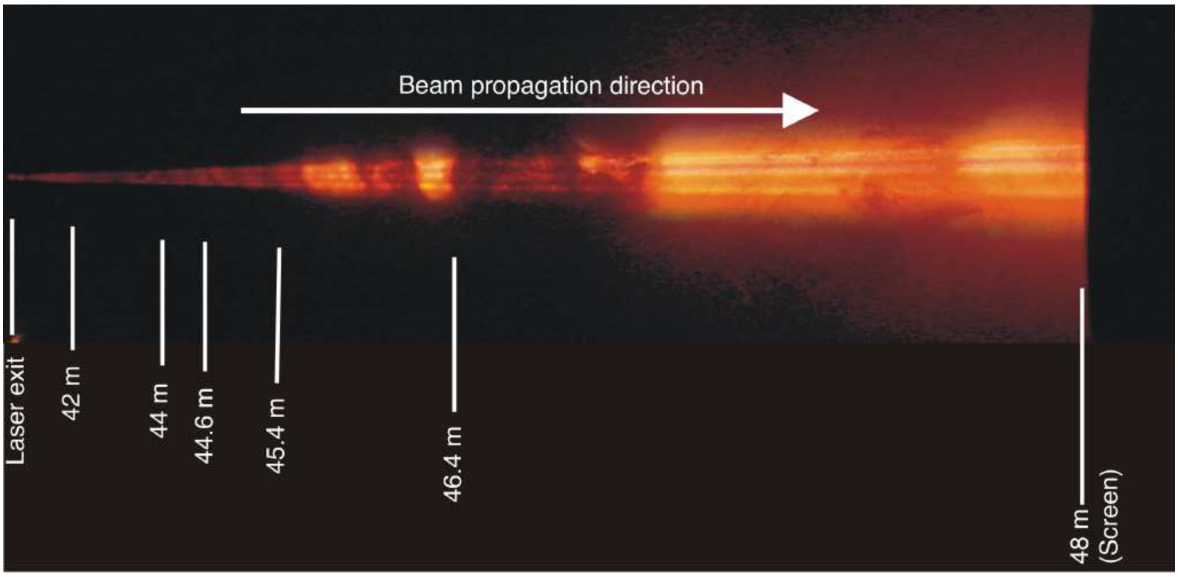

Figure 4.17.: Three "robust" filamentary structures propagating over ~ 8 m from the focal point ($f \simeq 40$ m) of a converging beam with 760 P_{cr} delivered by the Teramobile laser system.

distance between the laser exit and the first marked distance (42 m).

Figure 4.17 exhibits a quasi-continuous three-pillar structure that emerges from $z > 40$ m and was reproducible from image to image. In this Figure, the fluctuating intensity along the beam path is due to inhomogeneities in the haze, as was checked by visual inspection. Here, the observation of seemingly continuous structures along several meters on a single-shot image is an evidence for the occurrence of optical pillars within femtosecond laser beams. In the present configuration, the beam self-organizes into three major, distinct clusters of light after passing through the focal point of the long-range focusing lens.

Figure 4.18 shows a 3D plot issued from a direct numerical integration of Equation (4.7), using the same input intensity distribution multiplied by the parabolic phase $\exp(-ik_0r^2/2f)$ that accounts for the lens curvature ($f = 40$ m). As seen from this Figure, many filaments arise as the beam approaches the focal length $z \simeq f = 40$ m, where its minimum waist is attained. Remarkably, few filamentary structures emerge after this point: Only three of them propagate over ~ 10 m, under the form of sequences of quasi-continuous channels having the same direction and capable of covering more than 2 m as a whole. We attribute the transverse deflection of the most external filaments to the natural divergence of the beam envelope after the focus. This result again confirms the validity of the (2D+1)-dimensional model, together with the concept of "optical pillars": Long-range filaments can develop as individual entities located in the same region of the transverse plane, where a few intense cells

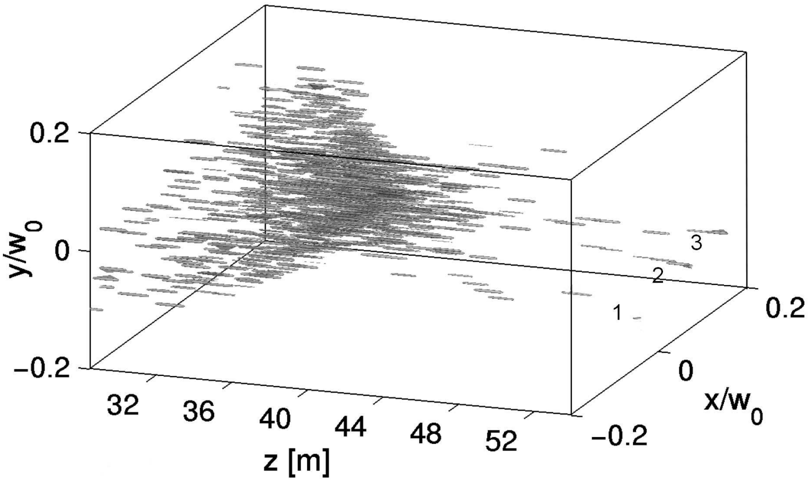

Figure 4.18.: Propagation of the same beam as in Figure 4.17, numerically computed from Equation (4.7) with a digitized data file of the input beam intensity profile affected by a spatially-parabolic phase. Three filaments, identified by the labels 1, 2 and 3, can develop long sequences (≥ 2 m) after the focus. Although partly disconnected over ~ 10 m, their strong directivity yields the appearance of quasi-continuous strings of light. The numerous filaments occurring at $z < 40$ m are not visible in Figure 4.17, due to the strong parallax in the beam imaging.

are recurrently emitted as they propagate in a quasi-continuous way.

To sum up, we have investigated the multiple filamentation of infrared femtosecond pulses in air, engaging high powers, both in nonfocused and focused geometries. Although intermittence of filaments affects the pulse dynamics, turbulent cells can converge towards long-range envelopes. These sustain the propagation over long distances while keeping an intensity close to the ionization threshold. To understand this behavior, we elaborated on a time-averaged 2D model [Equation (4.7)] describing the spatial dynamics of fs pulsed beams, even when they undergo a delayed Kerr response. First, we thoroughly discussed the major properties of this reduced model by specifying both conservative and dissipative fundamental soliton-like solutions and their mutual interaction regimes. Second, we tested this model over a few meters for ultrashort mm-waisted pulses. By fixing the effective pulse temporal extent T to 1/10 of the input duration in ionization regimes, results from this simplified model were observed to reasonably agree with the transverse patterns of (3D+1)-dimensional pulses. Next, we experimentally investigated the multiple filamentation of collimated beams delivered by the Teramobile laser, for powers up to 3-4 TW. Experimental patterns were then simulated by means of the previous 2D reduced equation, using a digitized file of the input beam fluence as initial data. Along distances limited to 100 m, long-range filaments were observed to be initiated by the most intense fluctuations of the input beam and those may persist over several tens of meters. From these ”optical pillars”, small-scale spots arise and recur rapidly at other locations in the diffraction pattern, in agreement with the scenario of ”optically-turbulent light guides” proposed in [11]. The long-living primary filaments, as well as unstable randomly-nucleated ones, can be described by the 2D model, which reproduces the qualitative and quantitative behaviors in the filamentation patterns. Further on, focused beams were investigated over several tens of meters along a complete propagation sequence. By optical coalescence, reduction of the beam waist in linearly focused geometry allowed to form very long light channels over almost 10 meters, by gathering all filamentary components into a limited number of light strings. These strings, although longer than one elementary filament and keeping the same direction, were numerically revealed to still develop from intermittent cells remaining localized in the same region of the diffraction plane. This observation thereby confirms the concept of ”optical pillars” supporting the long propagation of quasi-continuous light tubes.

4.3. Interaction of light filaments with obscurants in aerosols

In this last section we investigate the collision of femtosecond filaments with obscurants, namely water droplets. By means of (3D+1)-dimensional numerical simulations, we first compute the full space and time resolved dynamics of the interaction process. We show that the filament rebuilds over a few cm after the interaction zone, for droplet sizes up to 2/3 of the filament diameter, in agreement with recent experimental observations [30]. Because in reality obstacles do not exactly interact at the filament centroid, emphasis is also given to decentered obscurants. To understand better the rebuilding process, we compare fluence patterns of noisy Gaussian beams with results from the time-averaged model (see Section 4.2.1) in the presence of an obscurant.

Second, we investigate the influence of atmospheric humidity on the filamentation patterns created by TW laser beams over 10 m propagation scales. The dense fog dissipates quasi-linearly the energy in the beam envelope and diminishes the number of filaments in proportion. This number is strongly dependent on the power content of the beam. Power per unit filament is evaluated to about 5 critical powers for self-focusing in air. Numerical computations confirm that a dense fog composed of micrometric droplets acts like a linear dissipator of the wave envelope.

4.3.1. Single filament-droplet interaction

To start with, we perform several numerical simulations integrating Equations (2.53) with and without the interaction of the pulsed beam with a droplet. The input pulse is Gaussian, both in space and time, and perturbed by an 1 % amplitude random noise. Its initial waist w_0, half-width duration t_p and energy E_{in} are 0.5 mm, 100 fs (FWHM duration = 120 fs) and 4.2 mJ, respectively. So, the input beam power is equal to 10 P_{cr} with $P_{cr} = \lambda_0^2/2\pi n_b n_2 \simeq 3$ GW at $\lambda_0 = 800$ nm. The droplet is modelled by a circular amplitude mask, $M \equiv 1 - \sqrt{1-(r'/r_d)^2}$, where r_d and r' are the droplet radius and relative coordinate in the transverse plane. Opacity is maximum (zero transmission) at the center (x_0, y_0) of the obstacle. Its microscopic thickness $\leq 100\mu$m keeps the wave-field unchanged over comparable distances along z. We assume that photons scattered at large angles (e.g., backscattered) by the droplet are of negligible influence in the replenishment process.

Preliminary computations using the above parameters showed that the filament fully forms in free-propagation regime with a diameter (FWHM of the fluence distribution) of $\sim 160\,\mu$m at $z = 0.39$ m. It carries ~ 38 % of the input energy (this agrees with observations reported in [30]), while the remaining amount of energy is situated outwards the filament core. The round droplet (M) is then introduced on the filament path at $z \sim 0.4$ m. Figure 4.19 shows snapshots of the fluence $\mathcal{F} \equiv \int |\mathcal{E}|^2 dt$ for different droplet sizes ($50\,\mu\text{m} \leq \text{diameter} \leq 95\,\mu$m) placed at various locations in the (x, y) plane. From top to bottom, Row I illustrates the interaction of the beam with a centered droplet ($x_0 = y_0 = 0$) of $50\,\mu$m diameter. The filament core hits the droplet, refocuses at center and completely reforms within 2 cm only. In Row II, the filament robustness is tested with a larger droplet having 95 μm in diameter and shifted in space by 25 μm ($x_0 = +25\,\mu$m, $y_0 = 0$). No significant difference with the previous case appears, apart from an asymmetric refilling of the hole formed by the droplet. Figure 4.20 Row I details the corresponding intensity distributions in the (x, t) plane ($y = 0$). The "scar" introduced out of center by the droplet mainly affects the most intense time slices of the pulse. However, power is rapidly re-injected by the untouched parts of these slices to the "empty" regions of the filament. After an intermediate motion of back and forth, the symmetry around the axis $x = 0$ is restored at $z = 0.42$ m, i.e., the filament has been refilled. This refilling concerns temporal peaks located near $x = 0$, inside a contour $\leq 200\,\mu$m in diameter only. A symmetric refilling was also observed at the same distance for a centered 95 μm diameter droplet. Figure 4.20 Row II specifies the temporal profiles at $z \simeq 0.42$ m for various configurations. At this distance, the spatio-temporal structure of the filament is recovered, which signals

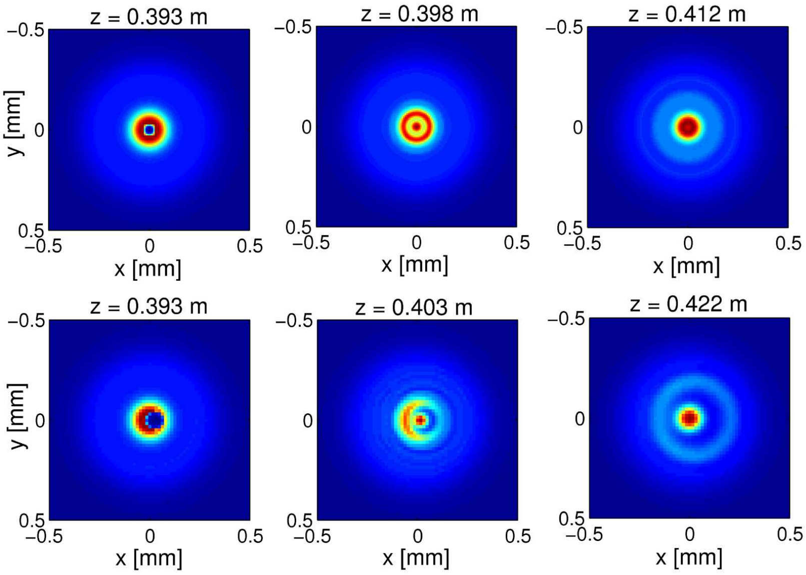

Figure 4.19.: Row I: Fluence distribution in the (x, y) plane of a fs filament hitting a 50 μm diameter centered droplet at $z = 0.393$ m; Row II: Fluence of the same filament hitting a decentered 95 μm large droplet.

its complete replenishment.

To get a deeper insight into the key-process involved in the pulse reshaping, we describe the same interactions through our time-averaged (2D+1)-dimensional model, achieved by a straightforward averaging in time of Equations (2.53) (see Section 4.2.1). We have seen that in the absence of MPA ($\nu = 0$), Equation (4.7) admits stable soliton solutions, $\psi = \phi(x, y) \exp(i\Lambda z)$ with power $P_s(\Lambda) = \int \phi^2 d\vec{r}$, resulting from the balance between the Kerr (cubic) nonlinearity and the nonlinear saturation related to the MPI defocusing source. Once MPA is introduced ($\nu \neq 0$), the soliton power decreases very fast during the early stages of ionization, but it slowly relaxes to $\sim P_{cr}$ at a maximal distance ($z_{MPA} \leq 0.5$ m). In the light of these features, we model the filament at $z = 0.39$ m by a soliton profile with an effective power $P_s \simeq 7\,P_{cr}$, which is close to the power engaged in the focused time slice at the filament front (see Figure 4.20), and let it propagate in the presence of centered 50 μm and decentered 95 μm large droplets. Figure 4.21 illustrates the resulting interactions: The pulse reshaping follows the same transversal dynamics as in Figure 4.19 and the replenishment process takes place over analogous longitudinal intervals. The initial soliton hits the obscurant, which removes part of its power. The remaining ring has a power above critical and simply self-reshapes into another soliton with lower power at center. Spatial solitons preserve their initial centroid, so that the nonlinear attractor gathers the ring structure at $x = y = 0$ into a new solitary wave. Since this modeling reproduces the collision dynamics, we

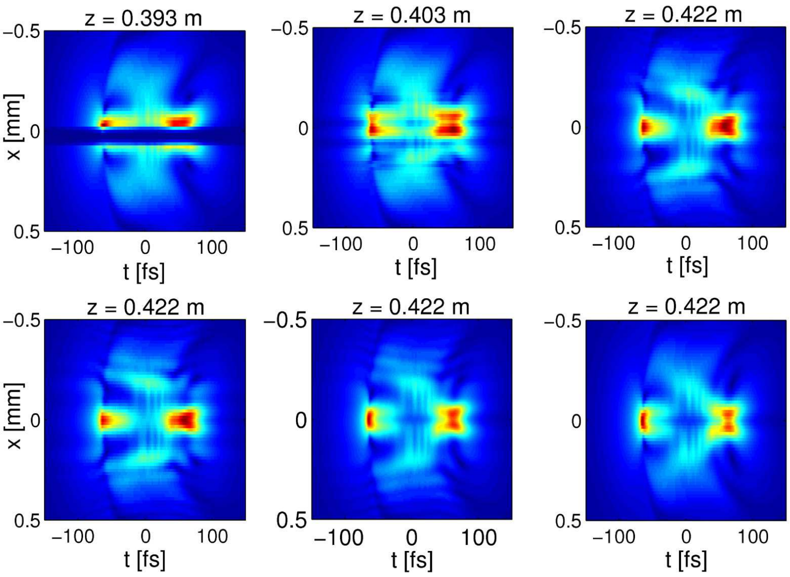

Figure 4.20.: Row I: Spatio-temporal distributions corresponding to Figure 4.19 Row II; Row II: Pulse intensity versus (x, t) at the distance $z = 0.422$ m for a centered 95 μm large droplet, a centered 50 μm large droplet and a free-of-obscurant filament (from left to right).

may evaluate the maximum radius of the droplet, $r_{d\max}$, above which the rebuilding of the filament ceases. By assuming Gaussian solitons with power P_{fil} and waist w_{fil}, the power integral remaining below critical in the radial domain $r_d \leq r < +\infty$ provides the estimate $r_{d\max} = w_{fil}\sqrt{0.5 \ln{(P_{fil}/P_{cr})}}$. We verified numerically with $P_{fil} = 7P_{cr}$ that a replenishment generating stable solitons ceased for droplet sizes larger than $150 - 180\mu$m, which agrees with this estimate.

In the pioneering experimental work [30], the authors attribute the robustness of the femtosecond filaments to a surrounding "photon bath". By "photon bath", they mean low-intensity components outside the core region which serve as an energy reservoir and compensate for the losses due to the interaction with the obscurant. It is important to observe that, by using pure solitons in the time averaged model, there is neither a "photon bath", nor a radiative component propagating with the filament in a collimated way and thus interacting with it. So, our previous result indicates that a "photon bath" is not needed to rebuild the beam. On the other hand, experiments performed in [32] show that a filament vanishes within $\sim$ 10 cm after propagating through an aperture, which cuts the surrounding low-intensity components. This shows that the low-intensity components are important for the long-range propagation. So how to clear up this contradiction? Both processes, self-healing of the scar introduced by the droplet and stalling of the filament by an aperture act on different z-scales. The

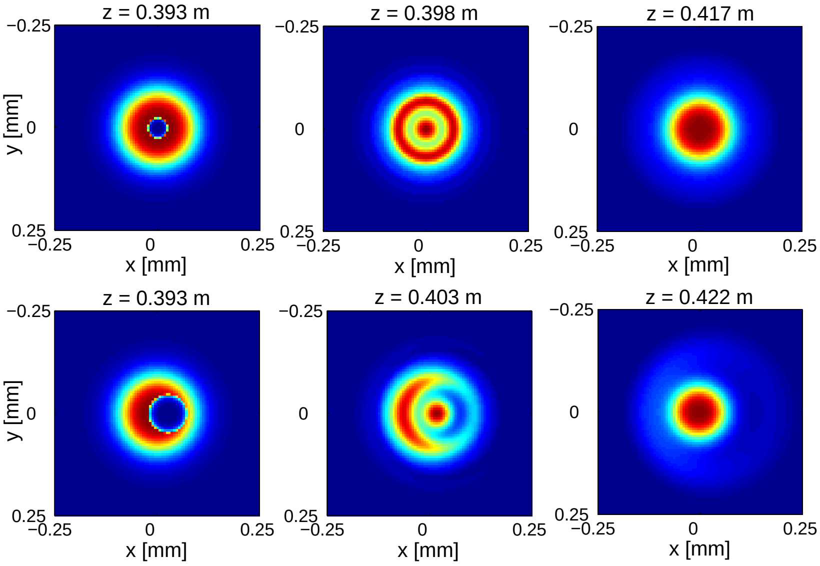

Figure 4.21.: Row I: Intensity distribution versus (x, y) of a soliton solution of Equation (3) conveying 7 critical powers and hitting a 50 μm diameter centered droplet; Row II: Same soliton hitting a decentered 95 μm large obscurant.

latter one is a direct consequence of the spatial replenishment mechanism: defocused time-slices are cut by the aperture, they can not (re-)focus and maintain the plasma channel at distant z-positions. The effect is visible on z-scales of the spatial replenishment mechanism $\sim$ 10 cm. The first process, the self-healing of the filament, acts on z-scales $\sim$ 1 cm. It is much faster than the spatial replenishment mechanism, because energy is redistributed in the core-region $\sim$ 300 μm only.

To confirm this property, we plotted the variations of energy along z for several configurations, both in the entire simulation box [Figure 4.22(a)] and inside a circular contour of 300 μm enclosing the filament core [Figure 4.22(b)]. In Figure 4.22(a), an energy drop of $\Delta E/E_{in} < 7\%$ occurs after the impact for the 95 μm large spatially-shifted droplet. This small energy loss also characterizes the interaction with a centered 95 μm large droplet, even though the major part of the filament is blocked by the obscurant. Figure 4.22(a) supports the comparison with experimental decreases of energy (see Figure 4.22(c)), measured upon one meter after the impact point. One can identify a first slow energy loss over $\sim$ 20 cm. This stage is then followed by a sharper decrease and ends by the final dissipation of the filament. Figure 4.22(b) details inner energy losses. Just after the interaction point, the energy in the filament continues to be evacuated *outwards* from the core region over more than 10 cm of propagation. If the surrounding "photon bath" was involved in the refilling process, we should instead observe a flux of energy *inwards* to the core region. The hump caused by a sudden energy growth at $z \sim 0.65$ m differs from the pulse re-filling and can be

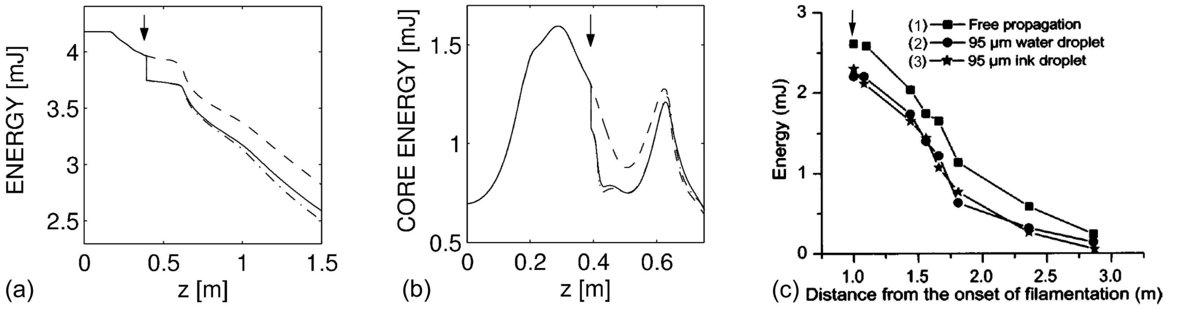

Figure 4.22.: (a) Energy versus z integrated throughout the entire simulation box for a 95 μm large spatially-shifted droplet (solid curve), for a 95 μm large centered droplet (dash-dotted curve) and for free propagation (dashed curve). (b) Energy variations computed over a disk of 300 μm in diameter enclosing the filament core. Arrow indicates the impact point. (c) Experimental results taken from [30]. The filament survives the interaction with a droplet (at $z = 1$ m) as large as 95 mm (2), even when the droplets are stained with black ink (3).

explained by the dynamic spatial replenishment mechanism (see previous paragraph). In free-propagation regime, when the back of the pulse takes over its front part, some intense pulse components are shifted outside the axis $x = y = 0$ [34, 73] [S7]. Energy is later reinjected into the filament core when these time slices refocus at center (see Figure 4.23). These "convected" components *belong to the filament itself* (see also [32]). With an obscurant, the same phenomenon affects the pulse in identical proportions, *far behind the impact point.*

Finally, we find it instructive to comment on the plasma channels excited by ionization of air molecules. These are illustrated in Figure 4.24 for an electron density level of 5×10^{15} cm^{-3}, in regimes of free propagation [Figure 4.24(a)] and for the interaction with the 95 μm large, decentered droplet [Figure 4.24(b)]. When the pulse propagates freely, a first channel emerges over $\Delta z \simeq 0.5$ m from the primary defocusing of the back of the pulse, which produces a short leading peak. At $z = 0.6 - 0.7$ m, plasma generation partly turns off and a trailing peak increases to the detriment of the front pulse. This prolongates the plasma channel after a transient stage where azimuthal instabilities develop [S7] and induce "snake-like" motions along the optical path. In Figure 4.24(b), the plasma channel is cut at the interaction point $z \simeq 0.4$ m, but it rapidly restarts from the short-scale refilling of the pulse. Up to residual modulations, it follows the same dynamics as in Figure 4.24(a) and covers an almost identical range.

In this section, we have numerically analyzed the interaction between femtosecond filaments with obscurants exhibiting different sizes and locations in the diffraction plane. For opacities up to 2/3 of the filament diameter, the energy loss caused by

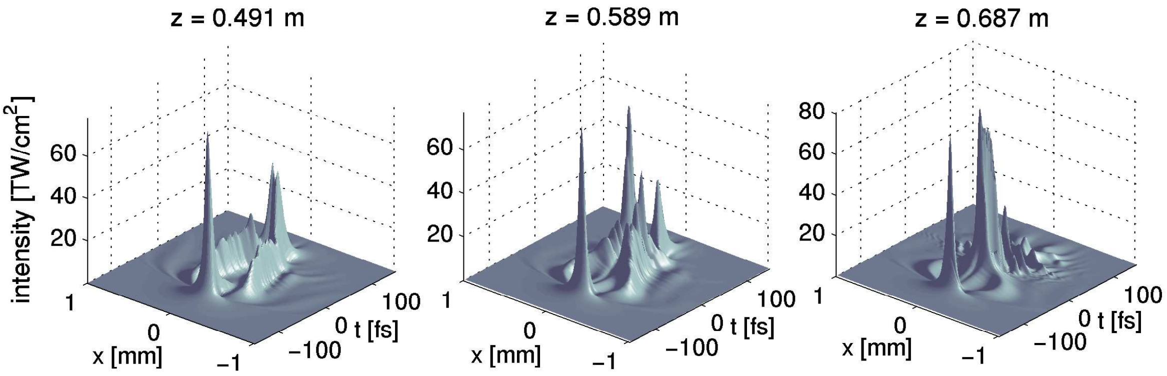

Figure 4.23.: Temporal profiles showing the displacement and re-focusing at center of the filament trail at $z \simeq 0.65$ m for free propagation.

the interaction was limited to 10 % of the input energy, and the replenishment of the filament is accomplished over a few cm along the propagation axis. This replenishment process is mainly driven by the dynamics of spatial solitons in saturable, dissipative media and takes place upon short longitudinal scales. The ”self-healing” of the filament follows from the relaxation of a high-power focused state to a lower-power one undergoing Kerr re-compression. The surrounding energy reservoir formed outside the filament core was proven to play a minor role in this mechanism.

4.3.2. Multifilamentation transmission through fog

In this last section we will present some recent results on the transmission of multiple filaments through a water cloud, which will be detailed in [S16]. The experiments were conducted with the Teramobile laser system, allowing for outdoor experiments under any weather condition. The Teramobile beam was propagated horizontally at the sea level (Lyon, 170 m altitude). After 40 m of free propagation, it hit a synthetic fog of water droplets produced in an open cloud chamber, depicted in [74]. The initial laser chirp was adjusted, so that filamentation began shortly before the beam enters the cloud. This corresponds to an initial pulse duration of 600 fs. Then, the filaments propagated over 10 meters through a quasi homogeneous cloud. The cloud density was estimated by measuring the elastic transmission of a low-power He:Ne laser. Its droplet size distribution was centered at 1 μm radius (i.e., much smaller than the filament size), as monitored by using an optical sizer (Grimm model G 1-108).

In a series of experiments, the beam profiles at the exit of the cloud chamber were recorded, both in the free propagation regime and with the synthetic cloud. Two different input laser energies, 220 mJ and 90 mJ, were used, the beam waist was about 2 cm. Filaments were clearly transmitted through the 10 m long cloud with 50%

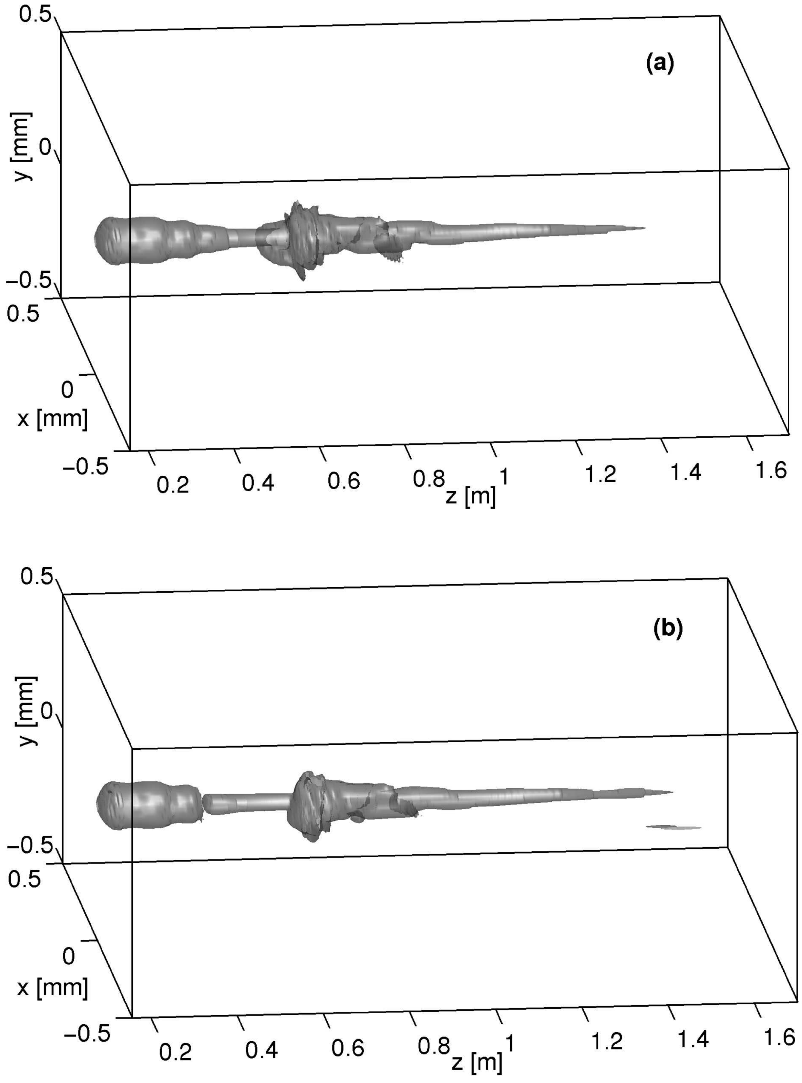

Figure 4.24.: Plasma strings created by ionization and computed from Equations (2.53) in the cases of (a) free propagation and (b) impact with a 95 μm diameter decentered droplet.

transmission. This transmission corresponds to an extinction coefficient $\epsilon = 0.07$ m^{-1}, i.e., to a droplet density of $N = 2.2 \times 10^4$ cm^{-3}. Thus, filamentation can survive the propagation in a fog. However, since much larger droplets are not sufficient to block the filaments (see previous section), the filaments are not destroyed by the cloud. The cloud's influence on the beam propagation can be expected to occur through the energy losses escaping from the overall beam envelope only. The transmitted beam power P_{tr} strongly influences the spatial distribution of filaments, and especially their number. The number of filaments decreases accordingly with the power left at the output of the cloud chamber. This shows that the cloud globally acts like a power attenuator on the beam as a whole: It promotes elastic extinction of the "photon bath" and its

P_{in}/P_{cr}	120		60	50	
Propagation	Free	Fog	Free	Free	Fog
P_{tr}/P_{cr} (exp)	120	60	-	50	25
# of Filaments (exp)	24	13	-	11	6
P_{tr}/P_{cr} (num)	120	60	60	50	25
# of Filaments (num)	25	12-15	13	12	6

Table 4.1.: Filament number versus input beam power after 50 m of propagation, thereof 10 m in free or foggy atmospheres.

embedded filaments.

Another argument which supports the identification of droplet induced losses with linear dissipation is the following: Assuming that droplets are completely opaque, the rate of losses caused by the obstacles along one small z-step Δz can be evaluated by $N\pi R^2\Delta z$, where N is the droplet density and R the droplet radius. Besides, the equivalent loss rate induced by the extinction coefficient ϵ is $\epsilon\Delta z$, since $\exp(-\epsilon\Delta z) \simeq 1 - \epsilon\Delta z$. Identifying both contributions leads to $\epsilon = N\pi R^2$. This result agrees with the experimental estimates for ϵ, N and R given above.

The power dependency of the number of filaments was investigated both experimentally and numerically. As far as numerics are concerned, we used the time-averaged model [Equation (4.7)]. The linear dissipation was introduced by an additional term $-(\epsilon/2)\psi$ on the right hand side. As input condition, we used a digitized file of the experimental input beam fluence with centrimetric waist. Results have been summarized in Table 4.3.2. Assuming weak absorption caused by plasma generation [S6], the beam power transmitted over 50 m of free propagation is almost constant, whereas that crossing the cloud chamber upon the same propagation distance can be estimated by $P_{tr} \simeq P_{in}/2$. A linear fit shows a ratio of one filament cell for every 15 GW of transmitted power. With $P_{cr} \simeq 3$ GW, this curve clearly indicates that about 5 critical powers are engaged in each filament, regardless of whether the beam propagates through a cloud or not. This estimate is in reasonably good agreement with previous theoretical expectations: It lies between the theoretical expectations applying to purely Kerr media ($P_{fil} \sim 3P_{cr}$) [27] and (3D+1)-dimensional simulations of femtosecond filaments self-channeling in air ($P_{fil} \sim 7P_{cr}$) [S12].

5. Conclusion and further prospects

In this thesis we have discussed nonlinear light propagation in waveguides and homogeneous transparent media, namely the atmosphere. As far as the propagation in a waveguide is concerned, we worked in two different regimes. First we considered the low power limit, where nonlinear effects are small and the trapping is linear (Section 3.1). Here we presented a sufficient stability criterion for weakly nonlinear bound states (weakly nonlinear guided waves). The simple knowledge of the eigenvalues associated with the linear modes of the potential V (refractive index distribution) allows us to predict the stability of the nonlinear bound states of the extended NLS equation (3.1). In spite of the fact that the criterion is valid for low power solitons only, the example of a step-potential shows that the present results may hold for wider ranges of power, both for focusing and defocusing nonlinearities.

Second, in the high power regime we showed that the waveguide can significantly increase the threshold power for catastrophic self-focusing (Section 3.2). Even for powers above the upper bound of the homogeneous case a stable propagation was observed. The explanation for the increase of the threshold power is that the additional interaction of the field with the waveguide disturbs the initial stage of self-focusing, and power is shed away and lost for the self-focusing mechanism.

The universality of the system under consideration, NLS equation with additional potential, offers a good perspective for further investigations and applications. As pointed out before, besides nonlinear optics the model also applies to Bose-Einstein condensates (BECs). The most apparent question is whether our sufficient stability criterion is a necessary one, too. At least our numerical results support this assumption. A further step would be to examine the decay dynamics of higher order solitons in non-rotationally symmetric potentials. It is still an open issue if they decay always into the ground state solution (as observed in our numerical examples), or if a decay into radiative modes only is possible. Moreover, allowing for a third transverse dimension (time) the wide field of "light bullets" is encountered. Here first interesting results dealing with stable 3D solitons in optical lattices are reported [75, 76].

In Chapter 4 we have investigated the multiple filamentation of infrared femtosecond pulses in air, engaging high powers, both in nonfocused and focused geometries. Although intermittence of filaments affects the pulse dynamics, turbulent cells can converge towards long-range envelopes. These sustain the propagation over long distances while keeping an intensity close to the ionization threshold. To understand this behavior, we elaborated on a time-averaged 2D model [Equation (4.7)] describing the spatial dynamics of fs pulsed beams, even when they undergo a delayed Kerr response. First, we thoroughly discussed the major properties of this reduced model by specifying both conservative and dissipative fundamental soliton-like solutions and their mutual interaction regimes. A noticeable enhancement of the propagation range through fusion processes combined with MPA was evidenced. Second, we tested this model over a few meters for ultrashort mm-waisted pulses. By fixing the effective pulse temporal extent T to 1/10 of the input duration in ionization regimes, results from this simplified model were observed to reasonably agree with the transverse patterns of (3D+1)-dimensional pulses. For narrow beams ($w_0 = 1$ mm) and weak powers ($\leq 40\,P_{cr}$), two filaments form and merge into one central lobe. For broader beams ($w_0 = 2$ mm) up to 90 P_{cr}, several filaments propagate almost independently of their neighbors. The physical length of each asymptotic filament is of the same order (≤ 1 m) in both configurations. This result is important, since Equation (4.7) provides an easy model to be integrated, which can be useful for estimating the number and position of filamentary channels created by high-power fs pulses.

Next, we experimentally investigated multifilamentation of collimated beams delivered by the Teramobile laser, for powers up to 3-4 TW. Experimental patterns were then simulated by means of the previous 2D reduced equation, using a digitized file of the input beam fluence as initial data. Along distances limited to 100 m, long-range filaments were observed to be initiated by the most intense fluctuations of the input beam and those may persist over several tens of meters. From these "optical pillars", small-scale spots arise and recur rapidly at other locations in the diffraction pattern, in agreement with the scenario of "optically-turbulent light guides" proposed in [11]. The long-living primary filaments, as well as unstable randomly-nucleated ones, can be described by the 2D model, which reproduces the qualitative and quantitative behaviors in the filamentation patterns. Direct confrontations of experimental results and numerical simulations revealed the existence of active optical zones keeping the beam collimated over considerable distances.

Further on, focused beams were investigated over several tens of meters along a complete propagation sequence. By optical coalescence, reduction of the beam waist in linearly focused geometry allowed to form very long light channels over almost 10 meters, by gathering all filamentary components into a limited number of light strings.

These strings, although longer than one elementary filament and keeping the same direction, were numerically revealed to still develop from intermittent cells remaining localized in the same region of the diffraction plane. This observation thereby confirms the concept of "optical pillars" supporting the long propagation of quasi-continuous light tubes.

Finally, we have numerically analyzed the interaction between femtosecond filaments with obscurants exhibiting different sizes and locations in the diffraction plane. For opacities up to 2/3 of the filament diameter, the energy loss caused by the interaction was limited to 10 % of the input energy, and the replenishment of the filament is accomplished over a few cm along the propagation axis. This replenishment process is mainly driven by the dynamics of spatial solitons in saturable, dissipative media and takes place upon short longitudinal scales. The "self-healing" of the filament follows from the relaxation of a high-power focused state to a lower-power one undergoing Kerr re-compression. The surrounding energy reservoir formed outside the filament core was proven to play a minor role in this mechanism.

Due to the overall subject of this thesis, namely nonlinear dynamics of trapped beams, we concentrated on the spatial dynamics of the femtosecond pulsed beams. However, temporal dynamics are important and far from being trivial. One important question is the influence of an initial chirp on femtosecond pulsed beam propagating in air. Pulse chirping introduces a quadratic temporal dependence in the pulsed beam phase at the laser exit. Combined with the group-velocity dispersion (GVD) in air, negatively chirped pulses with a duration t_p and phase in the form $\exp(-iCt^2/t_p^2)$ $C < 0$ undergo a compression in time. In linear regime, the minimum temporal extent $t_p^{min} = t_p/\sqrt{1+C^2}$ is achieved at the propagation distance $z_{min} = |C|t_p^2/2k''(1+C^2)$ [53]. This property, combined with plasma defocusing, can be used to trigger filamentation at different foci. Hence, negative chirps can be used for enhancement of the self-channeling length. Applying this property to Lidar experimental setups [72], chirping the pulse from 100 to 600 fs ($C \sim -5.92$) can re-trigger filamentation at z_{min} reaching the kilometer range. Combining pulse chirping with plasma defocusing also results in a tunable pulse shortening, whose characteristic distances could easily be accessed in further experiments [S15].

Another issue disregarded in this thesis is the supercontinuum generation by femtosecond filaments. Temporal variations experienced by the pulse produce a very broad spectral continuum, spanning from UV to IR wavelengths. Coherence is preserved between the different spectral components, so that the broadened pulse is often referred to as a "white light laser" [77]. Part of this supercontinuum leaks out from the beam as a narrow cone in the forward direction, called "conical emission" [18, 78], with typical half-angle of ∼ 0.12° at 500 nm. Most experimental and theoretical investigations using femtosecond Ti:Sa laser sources (800 nm) reported spectral broadening extending from 4.5 μm to an UV cut-off around 350 nm [79]. However, it was demonstrated that another emission peak around 265 nm arises from an additional process: Third Harmonic Generation [80–82]. Coupling between the pump field and the third harmonics develops an important spectral broadening in the wavelength domain 200 nm $\leq \lambda \leq$ 500 nm, which favors supercontinuum generation (two-colored filament). This spectral dynamics is identical over meter-range scales as well as over ∼ 100 m and beyond [S17]. The fact that long-range Lidar propagation (Teramobile laser) and laboratory-scaled experiments exhibit comparable supercontinuum generation can be explained by generic dynamics of a single filament. A broad beam undergoing multiple filamentation consists of many independent filaments with a typical length of ∼ 1 m [83]. In a way, the Lidar experiment is the incoherent superposition of ∼ 100 laboratory single filament experiments [S18]. Moreover, the two-colored filament is stabilized by third harmonic generation, whose principal effect on the IR pulse dynamics is to introduce a quintic, defocusing nonlinearity at large wave-vector mismatch values. This extra defocusing contribution arises as a saturating nonlinearity, which lowers the maximum intensity threshold reached by the fundamental component and, thereby, enhances the self-guiding range by an efficient decrease of the MPA damping of the filament [S19]. The question of knowing whether $\chi^{(5)}$ saturation is important or not was raised in several recent papers (see, e.g., [84–86], where quintic saturation were suggested to influence the propagation dynamics. However, no precise evaluation of the quintic coefficient was given, as no specific measurement of higher-order nonlinearities for oxygen molecules at 800 nm was realized up to now.

When it comes to temporal dynamics, especially supercontinuum generation and pulse shortening, higher order terms with respect to the temporal dynamics become important [Equation (2.52) should replace Equation (2.53a)]. The inclusion of the operators $\hat{T}$ and $\hat{T}^{-1}$ accounts for self steepening and space-time focusing [41]. Moreover, higher order dispersion terms may become no longer negligible. Additional efforts in the modeling are necessary, which may go far beyond the slowly varying envelope approximation [87].

To end with, nonlinear light propagation in homogeneous material is not restricted to the atmosphere. Similar effects like self-guided filamentation, plasma generation etc. were observed in fused silica [12, 88]. These processes usually originate from the early self-focusing of the beam, which causes an important growth of the laser intensity. Depending on the respective weights of dispersion versus the input peak power, the beam collapse can be halted by either chromatic dispersion [89, 90] or by plasma generation [66]. Whereas attention was mostly paid on femtosecond pulses undergoing normal GVD, much fewer studies were devoted to the influence of anomalous GVD. From the mathematical point of view, the possibility of creating "light bullets" in (2D+1)-dimensional media, stabilized by higher-order dispersion without plasma generation, was reported in [91]. For a cubic nonlinearity, fourth-order dispersion is able to regularize the wave blow-up for 1D spatial diffraction and anomalous GVD. This property, however, does not hold in (3D+1) dimensions, for which collapse still occurs [91]. From the experimental point of view, only one paper recently dealt with this fascinating dynamics [88]. Here, 50-fs pulses were focused into a BK7 glass sample at different laser wavelengths leading to normal or anomalous GVD. With normal GVD, the pulse developed short, multiple self-focusing events, guiding the beam within one Rayleigh length only. In contrast, with anomalous GVD, collapse events appeared over many Rayleigh lengths, giving rise to a long "segment" of light followed by shorter focusing/defocusing cycles at high enough powers. Anomalous GVD maintains the self-channeling of ultrashort pulses by continuously reinjecting energy into the self-focusing region, owing to the temporal compression that characterizes a 3D collapse. This dynamics, proposed in [88], has been confirmed by recent numerical simulations [S20]. It is possible to determine analytically the zones in the plane $(2z_0/L_D, P_{in}/P_{cr})$, where the collapse is strictly forbidden and where it triggers plasma generation. Moreover, the beam is clamped upon long distances at its peak saturation intensity, because the pulse temporal components are continuously compressed and shifted to the back of the pulse through self-steepening and third-order dispersion. This evolution favors the quasi-periodic formation of narrow, self-compressed cells of light, which typical duration can reach the optical cycle limit [S21]. This property could open new trends to produce few-cycle laser pulses.

Bibliography

References

[1] R. K. Dodd, J. C. Eilbeck, J. D. Gibbon, and H. C. Morris. *Solitons and Nonlinear Wave Equations*. Academic Press, London, 1982.

[2] F. Dalfovo, S. Giorgini, L. P. Pitaevskii, and S. Stringari. Theory of Bose-Einstein condensation in trapped gases,. *Rev. Mod. Phys.*, 71:463, 1999.

[3] V. E. Zakharov and E. A. Kuznetsov. Multi-scale expansions in the theory of systems integrable by the inverse scattering transform. *Physica D*, 18:455, 1986.

[4] R. Y. Chiao, E. Garmire, and C. H. Townes. Self-trapping of optical beams. *Phys. Rev. Lett.*, 13:479, 1964.

[5] S. A. Akhmanov, A. P. Sukhorukov, and R. V. Khokolov. Self-focusing and self-trapping of intense light beams in a nonlinear medium. *JETP Lett.*, 23:1025, 1966.

[6] T. Taniuti and H. Washimi. Self-trapping and instability of hydromagnetic waves along the magnetic field in a cold plasma. *Phys. Rev. Lett.*, 21:209, 1968.

[7] A. Hasegawa and F. Tappert. Transmission of stationary nonlinear optical pulses in dispersive dielectric fibers. I. Anomalous dispersion. *Appl. Phys. Lett.*, 23:142, 1973.

[8] L. F. Mollenauer, R. H. Stolen, and J. P. Gordon. Experimental observation of picosecond pulse narrowing and solitons in optical fibers. *Phys. Rev. Lett.*, 45:1095, 1980.

[9] L. Bergé. Wave collapse in physics: principles and applications to light and plasma waves. *Phys. Rep.*, 303:259, 1998.

[10] A. Braun, G. Korn, K. Liu, D. Du, J. Squier, and G. Mourou. Self-channeling of high-peak-power femtosecond laser pulses in air. *Opt. Lett.*, 20:73, 1995.

[11] M. Mlejnek, M. Kolesik, J. V. Moloney, and E. M. Wright. Optically turbulent femtosecond light guide in air. *Phys. Rev. Lett.*, 83:2938, 1999.

[12] S. Tzortzakis, L. Sudrie, M. Franco, B. Prade, A. Mysyrowicz, A. Couairon, and L. Berge. Self-guided propagation of ultrashort ir laser pulses in fused silica. *Phys. Rev. Lett.*, 87:213902, 2001.

[13] H. A. Rose and M. I. Weinstein. On the bound states of the nonlinear Schrödinger equation with a linear potential. *Physica D*, 30:207, 1988.

[14] T. J. Alexander and L. Bergé. Ground states and vortices of matter-wave condensates and optical guided waves. *Phys. Rev. E*, 65:026611, 2002.

[15] L. Bergé. Soliton stability versus collapse. *Phys. Rev. E*, 62:R3071, 2000.

[16] J. Schjødt-Eriksen, Yu. B. Gaididei, and P. L. Christiansen. Collapse arresting in an inhomogeneous two-dimensional nonlinear Schrödinger model. *Phys. Rev. E*, 64:06661, 2001.

[17] Yu. B. Gaididei, J. Schjødt-Eriksen, and P. L. Christiansen. Collapse arresting in an inhomogeneous quintic nonlinear Schrödinger model. *Phys. Rev. E*, 60:4890, 1999.

[18] E. T. J. Nibbering, P. F. Curley, G. Grillon, B. S. Prade, M. A. Franco, F. Salin, and A. Mysyrowicz. Conical emission from self-guided femtosecond pulses in air. *Opt. Lett.*, 21:62, 1996.

[19] A. Brodeur, C. Y. Chien, F. A. Ilkov, S. L. Chin, O. G. Kosareva, and V. P. Kandidov. Moving focus in the propagation of ultrashort laser pulses in air. *Opt. Lett.*, 22:304, 1997.

[20] B. La Fontaine, F. Vidal, Z. Jiang, C. Y. Chien, D. Comtois, A. Desparois, T. W. Johnston, J. C. Kieffer, H. Pépin, and H. P. Mercure. Filamentation of ultrashort pulse laser beams resulting from their propagation over long distances in air. *Phys. Plasmas*, 6:1615, 1999.

[21] S. L. Chin, A. Talebpour, J. Yang, S. Petit, V. P. Kandidov, O. G. Kosareva, and M. P. Tamarov. Filamentation of femtosecond laser pulses in turbulent air. *Appl. Phys. B*, 74:67, 2002.

[22] S. Tzortzakis, L. Bergé, A. Couairon, M. Franco, B. Prade, and A. Mysyrowicz. Breakup and fusion of self-guided femtosecond light pulses in air. *Phys. Rev. Lett.*, 86:5470, 2001.

[23] D. Mondelain. *Lidar linéaire et non-linéaire dans l'infrarouge moyen.* Phd Thesis N^O 212-2001, Université Cl. Bernard, Lyon 1, France, 2001.

[24] L. Wöste, C. Wedekind, H. Wille, P. Rairoux, B. Stein, S. Nikolov, C. Werner, S. Niedermeier, F. Ronneberger, H. Schillinger, and R. Sauerbrey. Femtosecond atmospheric lamp. *Laser & Optoelektron.*, 29:51, 1997.

[25] V. I. Bespalov and V. I. Talanov. Filamentary structure of light beams in nonlinear liquids. *JETP Lett.*, 3:307, 1966.

[26] J. H. Marburger. Self-focusing: Theory. *Prog. Quantum Electron.*, 4:35, 1975.

[27] L. Bergé, Cl. Gouédard, J. Schjødt-Eriksen, and H. Ward. Filamentation patterns in Kerr media vs. beam shape robustness, nonlinear saturation and polarization states. *Physica D*, 176:181, 2003.

[28] P. Rairoux, H. Schillinger, S. Niedermeier, M. Rodriguez, F. Ronneberger, R. Sauerbrey, B. Stein, D. Waite, C. Wedekind, H. Wille, L. Wöste, and C. Ziener. Remote sensing of the atmosphere using ultrashort laser pulses. *Appl. Phys. B*, 71:573, 2000.

[29] J. Kasparian, M. Rodriguez, G. Méjean, J. Yu, E. Salmon, H. Wille, R. Bourayou, S. Frey, Y. B. André, A. Mysyrowicz, R. Sauerbrey, J. P. Wolf, and L. Wöste. White-light filaments for atmospheric analysis. *Science*, 301:61, 2003.

[30] F. Courvoisier, V. Boutou, J. Kasparian, E. Salmon, G. Méjean, J. Yu, and J. P. Wolf. Ultraintense light filaments transmitted through clouds. *Appl. Phys. Lett.*, 83:213, 2003.

[31] A. C. Newell and J. V. Moloney. *Nonlinear Optics.* Addison-Wesley, Reading, MA, 1992.

[32] S. L. Chin, A. Brodeur, S. Petit O. G. Kosareva, and V. P. Kandidov. Filamentation and supercontinuum generation during the propagation of powerful ultrashort laser pulses in optical media (white light laser). *J. Nonlinear Opt. Phys. Mater.*, 8:121, 1999.

[33] A. Couairon, S. Tzortzakis, L. Bergé, M. Franco, B. Prade, and A. Mysyrowicz. Infrared femtosecond light filaments in air: simulations and experiments. *J. Opt. Soc. Am. B*, 19:1117, 2002.

[34] M. Mlejnek, E. M. Wright, and J. V. Moloney. Dynamic spatial replenishment of femtosecond pulses propagating in air. *Opt. Lett.*, 23:382, 1998.

[35] P. N. Butcher and D. Cotter. *The Elements of Nonlinear Optics.* Cambridge University Press, Cambridge, 1990.

[36] N. Kuzuu, K. Yoshida, H. Yoshida, T. Kamimura, and N. Kamisugi. Laser-induced bulk damage in various types of vitreous silica at 1064, 532, 355, and 266 nm: evidence of different damage mechanisms between 266-nm and longer wavelengths. *Appl. Opt.*, 38:2510, 1999.

[37] J. F. Ripoche, G. Grillon, B. Prade, M. Franco, E. Nibbering, R. Lange, and A. Mysyrowicz. Determination of the time dependence of n_2 in air. *Opt. Commun.*, 135:310, 1997.

[38] L. V. Keldysh. Ionization in field of a strong electromagnetic wave. *Sov. Phys. JETP*, 20:1307, 1965.

[39] M. V. Ammosov, N. B. Delone, and V. P. Krainov. Tunnel ionization of complex atoms and of atomic ions in an alternating electromagnetic field. *JETP Lett.*, 64:1191, 1986.

[40] A. M. Perelomov, V. S. Popov, and M. V. Terent'ev. Ionization of atoms in an alternating electric field. *JETP Lett.*, 23:924, 1966.

[41] T. Brabec and F. Krausz. Nonlinear optical pulse propagation in the single-cycle regime. *Phys. Rev. Lett.*, 78:3282, 1997.

[42] N. E. Kosmatov, V. F. Shvets, and V. E. Zakharov. Computer simulation of wave collapses in the nonlinear Schrödinger equation. *Physica D*, 52:16, 1991.

[43] C. A. Sackett, J. M. Gerton, M. Welling, and R. G. Hulet. Measurements of collective collapse in a Bose-Einstein condensate with attractive interactions. *Phys. Rev. Lett.*, 82:876, 1999.

[44] J. M. Gerton, D. Strekalov, I. Prodan, and R. G. Hulet. Direct observation of growth and collapse of a Bose-Einstein condensate with attractive interactions. *Nature*, 408:692, 2000.

[45] E. A. Donley, N. R. Claussen, S. L. Cornish, J. L. Roberts, E. A. Cornell, and C. E. Wieman. Dynamics of collapsing and exploding Bose-Einstein condensates. *Nature*, 412:295, 2001.

[46] M. R. Matthews, B. P. Anderson, P. C. Haljan, D. S. Hall, C. E. Wieman, and E. A. Cornell. Vortices in a Bose-Einstein condensate. *Phys. Rev. Lett.*, 83:2498, 1999.

[47] N. V. Alexeeva, I. V. Barashenkov, and D. E. Pelinovsky. Dynamics of the parametrically driven NLS solitons beyond the onset of the oscillatory instability. *Nonlinearity*, 12:103, 1999.

[48] I. V. Barashenkov, M. M. Bogdan, and V. I. Korobov. Stability diagram of the phase-locked solitons in the parametrically driven, damped nonlinear Schrödinger-equation. *Europhys. Lett.*, 15:113, 1991.

[49] D. V. Skryabin. Instabilities of vortices in a binary mixture of trapped Bose-Einstein condensates: Role of collective excitations with positive and negative energies. *Phys. Rev. A*, 63:013602, 2000.

[50] V. I. Korneev, N. N. Akhmediev, and T. D. Shermergor. Eigenmodes of a cylindrical wave-guide in a medium with nonlinear dielectric permittivity. *Izv. Vyssh. Uchebn. Zaved. Radiofiz. [Sov. Radiophys.]*, 37:1525, 1984.

[51] A. W. Snyder, D. J. Mitchell, and L. Poladian. Linear approach for appoximating spatial solitons and nonlinear guided modes. *J. Opt. Soc. Am. B*, 8:1618, 1991.

[52] J. J. Rasmussen and K. Rypdal. Blow-up in nonlinear Schrödinger equations-I. A general review. *Phys. Scr.*, 33:481, 1986.

[53] G. P. Agrawal. *Nonlinear Fiber Optics*. Academic Press, San Diego, third edition, 2001.

[54] D. L. Feder, M. S. Pindzola, L. A. Collins, B. I. Schneider, and C. W. Clark. Dark-soliton states of Bose-Einstein condensates in anisotropic traps. *Phys. Rev. A*, 62:053606, 2000.

[55] G. H. Golub and C. F. van Loan. *Matrix Computations*. Johns Hopkins University Press, Baltimore, 1996.

[56] B. J. LeMesurier and P. L. Christiansen. Regularization and control of self-focusing in the 2D cubic Schrödinger equation by attractive linear potentials. *Physica D*, 184:226, 2003.

[57] B. J. LeMesurier, P. L. Christiansen, Yu. B. Gaididei, and J. J. Rasmussen. Beam stabilization in the two-dimensional nonlinear Schrödinger equation with an

attractive potential by beam splitting and radiation. *Phys. Rev. E*, 70:046614, 2004.

[58] M. I. Weinstein. Non-linear Schrödinger-equations and sharp interpolation estimates. *Commun. Math. Phys.*, 87:567, 1983.

[59] G. Fibich and A. L. Gaeta. Critical power for self-focusing in bulk media and in hollow waveguides. *Opt. Lett.*, 25:335, 2000.

[60] H. Wille, M. Rodriguez, J. Kasparian, D. Mondelain, J. Yu, A. Mysyrowicz, R. Sauerbrey, J. P. Wolf, , and L. Wöste. Teramobile: A mobile femtosecond-terawatt laser and detection system. *Eur. Phys. Jour. - Appl. Phys.*, 20:183, 2002.

[61] S. Champeaux and L. Bergé. Femtosecond pulse compression in pressure-gas cells filled with argon. *Phys. Rev. E*, 68:066603, 2003.

[62] S. Champeaux and L. Bergé. Postionization regimes of femtosecond laser pulses self-channeling in air. To appear in Phys. Rev. E, 2005.

[63] A. J. Campillo, S. L. Shapiro, and B. R. Suydam. Periodic breakup of optical beams due to self-focusing. *Appl. Phys. Lett.*, 23:628, 1973.

[64] A. J. Campillo, S. L. Shapiro, and B. R. Suydam. Relationship of self-focusing to spatial instability modes. *Appl. Phys. Lett.*, 24:178, 1974.

[65] K. Konno and H. Suzuki. Self-focussing of laser beam in nonlinear media. *Phys. Scr.*, 20:382, 1979.

[66] H. Ward and L. Bergé. Temporal shaping of femtosecond solitary pulses in photoionized media. *Phys. Rev. Lett.*, 90:053901, 2003.

[67] A. A. Kolokolov. Stability of stationary solutions of the nonlinear wave equation. *Izv. Vyssh. Uchebn. Zaved. Radiofiz. [Sov. Radiophys.]*, 17:1332, 1974.

[68] N. G. Vakhitov and A. A. Kolokolov. Stationary solutions of the wave equation in the medium with nonlinearity saturation. *Izv. Vyssh. Uchebn. Zaved. Radiofiz. [Sov. Radiophys.]*, 16:1020, 1973.

[69] E. A. Kuznetsov, A. M. Rubenchik, and V. E. Zakharov. Soliton stability in plasmas and hydrodynamics. *Phys. Rep.*, 142:103, 1986.

[70] M. I. Weinstein. Lyapunov stability of ground-states of nonlinear dispersive evolution-equations. *Commun. Pure Appl. Math.*, 39:51, 1986.

[71] L. Bergé, J. J. Rasmussen, E. A. Kuznetsov, E. G. Shapiro, and S. K. Turitsyn. Self-focusing of chirped optical pulses in media with normal dispersion. *J. Opt. Soc. Am. B*, 13:1879, 1996.

[72] M. Rodriguez, R. Bourayou, G. Méjean, J. Kasparian, J. Yu, E. Salmon, A. Scholz, B. Stecklum, J. Eislöffel, U. Laux, A. P. Hatzes, R. Sauerbrey, L. Wöste, and J. P. Wolf. Kilometer-range nonlinear propagation of femtosecond laser pulses. *Phys. Rev. E*, 69:036607, 2004.

[73] L. Bergé and A. Couairon. Nonlinear propagation of self-guided ultra-short pulses in ionized gases. *Phys. Plasmas*, 7:210, 2000.

[74] G. Mejéan, J. Kasparian, J. Yu, A. Frey, E. Salmon, and J. P. Wolf. Remote detection and identification of biological aerosols using a femtosecond terawatt lidar system. *Appl. Phys. B*, 78:535, 2004.

[75] D. Mihalache, D. Mazilu, F. Lederer, Y. V. Kartashov, L. C. Crasovan, and L. Torner. Stable three-dimensional spatiotemporal solitons in a two-dimensional photonic lattice. *Phys. Rev. E*, 70:055603(R), 2004.

[76] D. Mihalache, D. Mazilu, F. Lederer, B. A. Malomed, Y. V. Kartashov, L. C. Crasovan, and L. Torner. Stable spatiotemporal solitons in bessel optical lattices. Submitted to Phys. Rev. Lett., 2005.

[77] S. L. Chin, S. Petit, F. Borne, and K. Miyazaki. The white light supercontinuum is indeed an ultrafast white light laser. *Jpn. J. Appl. Phys.*, 38:L126, 1999.

[78] O. Kosareva, V. P. Kandidov, A. Brodeur, C. Y. Chien, and S. L. Chin. Conical emission from laser-plasma interactions in the filamentation of powerful ultrashort laser pulses in air. *Opt. Lett.*, 22:1332, 1997.

[79] J. Kasparian, R. Sauerbrey, D. Mondelain, S. Niedermeier, J. Yu, J. P. Wolf, Y. B. André, M. Franco, B. Prade, S. Tzortzakis, A. Mysyrowicz, M. Rodriguez, H. Wille, and L. Wöste. Infrared extension of the super continuum generated by femtosecond terawatt laser pulses propagating in the atmosphere. *Opt. Lett.*, 25:1397, 2000.

[80] N. Aközbek, A. Iwasaki, A. Becker, M. Scalora, S. L. Chin, and C. M. Bowden. Third-harmonic generation and self-channeling in air using high-power femtosecond laser pulses. *Phys. Rev. Lett.*, 89:143901, 2002.

[81] H. Yang, J. Zhang, J. Zhang, L. Z. Zhao, Y. J. Li, H. Teng, Y. T. Li, Z. H. Wang, Z. L. Chen, Z. Y. Wei, J. X. Ma, W. Yu, and Z. M. Sheng. Third-order harmonic generation by self-guided femtosecond pulses in air. *Phys. Rev. E*, 67:015401, 2003.

[82] F. Théberge, W. Liu, Q. Luo, and S. L. Chin. Ultrabroadband continuum generated in air (down to 230 nm) using ultrashort and intense laser pulses. *Appl. Phys. B*, 80:221, 2005.

[83] L. Bergé, S. Skupin, F. Lederer, G. Méjean, J. Yu, J. Kasparian, E. Salmon, J. P. Wolf, M. Rodriguez, L. Wöste, R. Bourayou, and R. Sauerbrey. Multiple filamentation of terawatt laser pulses in air. *Phys. Rev. Lett.*, 92:225002, 2004.

[84] N. Aközbek, C. M. Bowden, A. Talebpour, and S. L. Chin. Femtosecond pulse propagation in air: Variational analysis. *Phys. Rev. E*, 61:4540, 2000.

[85] N. Aközbek, M. Scalora, C. M. Bowden, , and S. L. Chin. White-light continuum generation and filamentation during the propagation of ultra-short laser pulses in air. *Opt. Commun.*, 191:353, 2001.

[86] A. Vinçotte and L. Bergé. $\chi^{(5)}$ susceptibility stabilizes the propagation of ultrashort laser pulses in air. *Phys. Rev. A*, 70:061802(R), 2004.

[87] M. Kolesik, J. V. Moloney, and M. Mlejnek. Unidirectional optical pulse propagation equation. *Phys. Rev. Lett.*, 89:283902, 2002.

[88] K. D. Moll and A. L. Gaeta. Role of dispersion in multiple-collapse dynamics. *Opt. Lett.*, 29:995, 2004.

[89] M. Kolesik, G. Katona, J. V. Moloney, and E. M. Wright. Physical factors limiting the spectral extent and band gap dependence of supercontinuum generation. *Phys. Rev. Lett.*, 91:043905, 2003.

[90] M. Kolesik, E. M. Wright, and J. V. Moloney. Dynamic nonlinear X waves for femtosecond pulse propagation in water. *Phys. Rev. Lett.*, 92:253901, 2004.

[91] G. Fibich and B. Ilan. Optical light bullets in a pure Kerr medium. *Opt. Lett.*, 29:887, 2004.

[92] W. H. Press, B. P. Flannery, S. A. Teukolsky, and W. T. Vetterling. *Numerical Recipies.* Cambridge University Press, Cambridge, 1989.

[93] G. R. Hadley. Transparent boundary-condition for beam propagation. *Opt. Lett.*, 16:624, 1991.

List of publications

[S1] S. Skupin, U. Peschel, L. Bergé, and F. Lederer. Nonlinearly induced single mode behavior in multi-mode fibers. In *Technical Digest Nonlinear Guided Waves and Their Applications,* TUB1, 2004.

[S2] S. Skupin, U. Peschel, L. Bergé, and F. Lederer. Stability of weakly nonlinear localized states in attractive potentials. *Phys. Rev. E*, 70:016614, 2004.

[S3] S. Skupin, U. Peschel, and F. Lederer. Collapse suppression by a positive index profile. In *Europhys. Conf. Abstracts*, volume 27E, EB3W, 2003.

[S4] S. Skupin, U. Peschel, C. Etrich, L. Leine, F. Lederer, and D. Michaelis. Simulation of femtosecond pulse propagation in air. *Opt. Quant. Electron.*, 35:573, 2003.

[S5] S. Skupin, U. Peschel, and F. Lederer. Simulation of femtosecond laser pulses propagating in air. In *Proceedings 10th International Workshop on Optical Waveguide Theory and Numerical Modelling*, page 24, 2002.

[S6] L. Bergé, S. Skupin, F. Lederer, G. Méjean, J. Yu, J. Kasparian, E. Salmon, J. P. Wolf, M. Rodriguez, L. Wöste, R. Bourayou, and R. Sauerbrey. Multiple filamentation of terawatt laser pulses in air. *Phys. Rev. Lett.*, 92:225002, 2004.

[S7] S. Skupin, U. Peschel, C. Etrich, L. Leine, D. Michaelis, and F. Lederer. Intense pulses in air: Breakup of rotational symmetry. *Opt. Lett.*, 27:1812, 2002.

[S8] S. Skupin, U. Peschel, and F. Lederer. Azimuthal instabilities of intense femtosecond pulses propagating in air. In *Technical Digest Conference on Lasers & Electro-Optics*, volume 1, page 451, 2002.

[S9] L. Bergé, S. Skupin, F. Lederer, G. Méjean, J. Yu, J. Kasparian, E. Salmon, and J. P. Wolf. Spatial break-up of femtosecond laser pulses in the atmosphere. *Phys. Scr.*, T107:135, 2004.

[S10] S. Skupin, L. Bergé, U. Peschel, and F. Lederer. Filamentation of femtosecond pulses in air: Turbulent short-scale cells versus long-range clusters. In *Technical Digest Nonlinear Guided Waves and Their Applications,* TUC28, 2004.

[S11] S. Skupin, L. Bergé, U. Peschel, F. Lederer, G. Méjean, J. Yu, J. Kasparian, E. Salmon, J. P. Wolf, M. Rodriguez, L. Wöste, R. Bourayou, and R. Sauerbrey.

Filamentation of femtosecond light pulses in the air: Turbulent cells versus long-range clusters. *Phys. Rev. E*, 70:046602, 2004.

[S12] S. Skupin, L. Bergé, U. Peschel, and F. Lederer. Interaction of femtosecond light filaments with obscurants in aerosols. *Phys. Rev. Lett.*, 93:023901, 2004.

[S13] L. Bergé, S. Skupin, U. Peschel, and F. Lederer. Femtosecond light filaments: Robust "tracks" through the atmosphere? In *Technical Digest Conference on Lasers & Electro-Optics,* JME6, 2004.

[S14] S. Skupin. Simulation der Ausbreitung hochenergetischer Lichtpulse in Gasen. Diplomarbeit, Physikalisch-Astromische Fakultät, Friedrich-Schiller-Universität Jena, 2001.

[S15] R. Nuter, S. Skupin, and L. Bergé. Chirp-induced dynamics of femtosecond filaments in air. To appear in Opt. Lett., 2005.

[S16] G. Méjean, J. Kasparian, J. Yu, S. Frey, J. P. Wolf, S. Skupin, A. Vinçotte, R. Nuter, S. Champeaux, and L. Bergé. Multifilamentation transmission through fog. Submitted to Phys. Rev. A, 2005.

[S17] G. Méjean, J. Kasparian, J. Yu, S. Frey, E. Salmon, R. Ackermann, J. P. Wolf, L. Bergé, and S. Skupin. UV-supercontinuum generated by laser-pulse filamentation in air. Submitted to Appl. Phys. Lett., 2005.

[S18] S. Skupin, F. Lederer, L. Bergé, G. Méjean, J. Kasparian, J. Yu, S. Frey, E. Salmon, R. Ackermann, and J. P. Wolf. Super-broadband continuum at UV-visible wavelengths generated by ultrashort laser-pulses in air. To appear in *Technical Digest Conference on Lasers & Electro-Optics*, CMK4, 2005.

[S19] L. Bergé, S. Skupin, G. Méjean, J. Kasparian, J. Yu, S. Frey, E. Salmon, and J. P. Wolf. Supercontinuum emission and enhanced self-guiding of infrared femtosecond filaments sustained by third-harmonic generation in air. *Phys. Rev. E*, 71:016602, 2005.

[S20] S. Skupin, L. Bergé, U. Peschel, and F. Lederer. On the propagation of high intense laser pulses in media with normal and anomalous dispersion. To appear in *Europhys. Conf. Abstracts*, 2005.

[S21] L. Bergé and S. Skupin. Self-channeling of ultrashort laser pulses in materials with anomalous dispersion. Submitted to Phys. Rev. Lett., 2005.

A. Mathematical details

A.1. Components of unstable modes have equal norm

We prove the relation $\Im\lambda \int \left(|\delta U_1|^2 - |\delta U_2|^2\right) RdR = 0$ [Equation (3.13)].

$$\begin{aligned}
& \Im\lambda \int \left(|\delta U_1|^2 - |\delta U_2|^2\right) RdR \qquad\qquad (\text{A.1}) \\
= & \frac{1}{2i} \int \left\{ [\delta U_1^* i(\Im\lambda)\delta U_1 - \text{c.c.}] - [\delta U_2^* i(\Im\lambda)\delta U_2 - \text{c.c.}] \right\} RdR \\
= & \frac{1}{2i} \int \left\{ \left[\delta U_1^* \left(\hat{D}_{M+m} - \beta - \Re\lambda + 2\sigma U^2\right)\delta U_1 + \delta U_1^* \sigma U^2 \delta U_2 - \text{c.c.}\right] \right. \\
& \left. - \left[\delta U_2^* \left(-\hat{D}_{M-m} + \beta - \Re\lambda - 2\sigma U^2\right)\delta U_2 - \delta U_2^* \sigma U^2 \delta U_1 - \text{c.c.}\right] \right\} RdR \\
= & \frac{1}{2i} \int \left\{ \left[\delta U_1^* \frac{1}{R}\frac{\partial}{\partial R}\left(R\frac{\partial}{\partial R}\right)\delta U_1 + \delta U_1^* \sigma U^2 \delta U_2 - \text{c.c.}\right] \right. \\
& \left. + \left[\delta U_2^* \frac{1}{R}\frac{\partial}{\partial R}\left(R\frac{\partial}{\partial R}\right)\delta U_2 + \delta U_2^* \sigma U^2 \delta U_1 - \text{c.c.}\right] \right\} RdR
\end{aligned}$$

where we used Equation (3.7a) and the fact that the quantities $\Re\lambda$, β, V, σU^2 and M^2/R^2 are real-valued. In the above equation, it is easy to see that

$$\left[\delta U_1^* \sigma U^2 \delta U_2 - \text{c.c.}\right] + \left[\delta U_2^* \sigma U^2 \delta U_1 - \text{c.c.}\right] = 0, \tag{A.2}$$

which leaves us with the task to show that

$$\int \left[f^* \frac{\partial}{\partial R}\left(R\frac{\partial}{\partial R}\right) f - f \frac{\partial}{\partial R}\left(R\frac{\partial}{\partial R}\right) f^* \right] dR = 0, \tag{A.3}$$

where either $f = \delta U_1$ or $f = \delta U_2$. Since $\lim_{R\to\infty} f,\ \partial_R f = 0$, integration by parts in both terms immediately shows the desired result.

Similar integral relations were previously established in [47], in order to prove that a resonance of two localized eigenmodes produce soliton instability in the context of the parametrically driven NLS equation.

A.2. Power integral and Hamiltonian are constants of motion

We show that Power integral [Equation (3.24)] and Hamiltonian [Equation (3.36)] are conserved for solutions of Equation (3.35). In the case $V \equiv 0$ the same follows for the pure NLS equation [Equation 3.23]. With Equation (3.35) and integration by parts we see

$$\begin{aligned}
\frac{\partial}{\partial Z}P &= \int\left(\Psi^*\frac{\partial}{\partial Z}\Psi + \text{c.c.}\right)dXdY \qquad\qquad (\text{A}.4)\\
&= \int\left[i\Psi^*\left(\frac{\partial^2}{\partial X^2}+\frac{\partial^2}{\partial Y^2}\right)\Psi + i\left|\Psi\right|^4 - iV\left|\Psi\right|^2 + \text{c.c.}\right]dXdY\\
&= -\int\left(i\left|\frac{\partial\Psi}{\partial X}\right|^2 + i\left|\frac{\partial\Psi}{\partial Y}\right|^2 + \text{c.c.}\right)dXdY = 0
\end{aligned}$$

and

$$\begin{aligned}
\frac{\partial}{\partial Z}H^V &= \int\left\{\left[\frac{\partial\Psi^*}{\partial X}\frac{\partial}{\partial X} + \frac{\partial\Psi^*}{\partial Y}\frac{\partial}{\partial Y} + \left(V-\left|\Psi\right|^2\right)\Psi^*\right]\frac{\partial}{\partial Z}\Psi + \text{c.c.}\right\}dXdY \qquad (\text{A}.5)\\
&= \int\left\{i\frac{\partial\Psi^*}{\partial X}\left(\frac{\partial^2}{\partial X^2}+\frac{\partial^2}{\partial Y^2}\right)\frac{\partial\Psi}{\partial X} + i\frac{\partial\Psi^*}{\partial Y}\left(\frac{\partial^2}{\partial X^2}+\frac{\partial^2}{\partial Y^2}\right)\frac{\partial\Psi}{\partial Y}\right.\\
&\quad +i\Psi^2\left[\left(\frac{\partial\Psi^*}{\partial X}\right)^2 + \left(\frac{\partial\Psi^*}{\partial Y}\right)^2\right] + i2\left|\Psi\right|^2\left(\left|\frac{\partial\Psi}{\partial X}\right|^2 + \left|\frac{\partial\Psi}{\partial Y}\right|^2\right)\\
&\quad -i\Psi\left(\frac{\partial V}{\partial X}\frac{\partial\Psi^*}{\partial X} + \frac{\partial V}{\partial Y}\frac{\partial\Psi^*}{\partial Y}\right) - iV\left(\left|\frac{\partial\Psi}{\partial X}\right|^2 + \left|\frac{\partial\Psi}{\partial Y}\right|^2\right)\\
&\quad \left. +i\left(V-\left|\Psi\right|^2\right)\Psi^*\left(\frac{\partial^2}{\partial X^2}+\frac{\partial^2}{\partial Y^2}\right)\Psi - i\left|\Psi\right|^2\left(V-\left|\Psi\right|^2\right)^2 + \text{c.c.}\right\}\\
&= -\int\left\{i\left(\left|\frac{\partial^2\Psi}{\partial X^2}\right|^2 + 2\left|\frac{\partial^2\Psi}{\partial X\partial Y}\right|^2 + \left|\frac{\partial^2\Psi}{\partial Y^2}\right|^2\right) + iV\left(\left|\frac{\partial\Psi}{\partial X}\right|^2 + \left|\frac{\partial\Psi}{\partial Y}\right|^2\right)\right.\\
&\quad +i2\Re\left(\Psi\frac{\partial V}{\partial X}\frac{\partial\Psi^*}{\partial X} + \Psi\frac{\partial V}{\partial Y}\frac{\partial\Psi^*}{\partial Y}\right) - i2\Re\left[\Psi^2\left(\frac{\partial\Psi^*}{\partial X}\right)^2 + \Psi^2\left(\frac{\partial\Psi^*}{\partial Y}\right)^2\right]\\
&\quad \left. -i2\left|\Psi\right|^2\left(\left|\frac{\partial\Psi}{\partial X}\right|^2 + \left|\frac{\partial\Psi}{\partial Y}\right|^2\right) + \text{c.c.}\right\} = 0.
\end{aligned}$$

A.3. Computing the virial

We show that Equation (3.41) is valid. In the case $V \equiv 0$ Equation (3.34) follows for the pure NLS equation [Equation 3.23]. With Equations (3.35), (3.36) and integration by parts we see

$$
\begin{aligned}
\frac{\partial^2 S}{\partial Z^2} &= \frac{\partial}{\partial Z}\int \Bigg[\left(X^2+Y^2\right)\Psi^*\frac{\partial}{\partial Z}\Psi + \text{c.c.}\Bigg]\, dXdY \\
&= \frac{\partial}{\partial Z}\int \Bigg[i\left(X^2+Y^2\right)\Psi^*\left(\frac{\partial^2}{\partial X^2}+\frac{\partial^2}{\partial Y^2}\right)\Psi + \text{c.c.}\Bigg]\, dXdY \\
&= \frac{2}{i}\int \Bigg[\frac{\partial \Psi^*}{\partial Z}\left(X\frac{\partial}{\partial X}+Y\frac{\partial}{\partial Y}\right)\Psi + \Psi^*\left(X\frac{\partial}{\partial X}+Y\frac{\partial}{\partial Y}\right)\frac{\partial \Psi}{\partial Z} + \text{c.c.}\Bigg]\, dXdY \\
&= 2\int \Bigg[2\left|\frac{\partial \Psi}{\partial X}\right|^2 + 2\left|\frac{\partial \Psi}{\partial Y}\right|^2 - \Psi^*\left(X\frac{\partial^3}{\partial X^3}+Y\frac{\partial^3}{\partial X^2\partial Y}+X\frac{\partial^3}{\partial X\partial Y^2}\right)\Psi \\
&\qquad -\Psi^* Y\frac{\partial^3}{\partial Y^3}\Psi - \left(|\Psi|^2 - V\right)\Psi^*\left(X\frac{\partial}{\partial X}+Y\frac{\partial}{\partial Y}\right)\Psi + \Psi^* X\frac{\partial^3}{\partial X^3}\Psi \\
&\qquad +\Psi^*\left(Y\frac{\partial^3}{\partial X^2\partial Y}+X\frac{\partial^3}{\partial X\partial Y^2}+Y\frac{\partial^3}{\partial Y^3}\right)\Psi + |\Psi|^2 X\frac{\partial}{\partial X}\left(|\Psi|^2 - V\right) \\
&\qquad +|\Psi|^2 Y\frac{\partial}{\partial Y}\left(|\Psi|^2 - V\right) + \left(|\Psi|^2 - V\right)\Psi^*\left(X\frac{\partial \Psi}{\partial X}+Y\frac{\partial \Psi}{\partial Y}\right) + \text{c.c.}\Bigg]\, dXdY \\
&= 2\int \Bigg[2\left|\frac{\partial \Psi}{\partial X}\right|^2 + 2\left|\frac{\partial \Psi}{\partial Y}\right|^2 + \frac{1}{2}|\Psi|^2\left(X\frac{\partial}{\partial X}+Y\frac{\partial}{\partial Y}\right)\left(|\Psi|^2 - 2V\right) \\
&\qquad -\frac{1}{2}|\Psi|^2\left(2+X\frac{\partial}{\partial X}+Y\frac{\partial}{\partial Y}\right)|\Psi|^2 + \text{c.c.}\Bigg]\, dXdY \\
&= 8H^V - 4\int |\Psi|^2\left[2V + \left(X\frac{\partial}{\partial X}+Y\frac{\partial}{\partial Y}\right)V\right] dXdY.
\end{aligned}
\tag{A.6}
$$

A.4. Spectral problem for soliton stability against non-isotropic perturbations

We briefly sketch the spectral equations for the ground state stability versus non-isotropic perturbations with azimuthal number m. According to the standard procedure for linear stability analysis we introduce a small perturbation $\delta\phi$ on the real valued soliton shape ϕ. We plug $A = (\phi + \delta\phi)\exp(i\Lambda Z)$ into Equation (4.8) and linearize it with respect to the perturbation. The resulting evolution equation for the perturbative mode $\delta\phi$ is then given by

$$\frac{\partial}{\partial Z}\delta\phi = i\Delta_\perp\delta\phi - i\Lambda\delta\phi + i2\phi^2\delta\phi + i\phi^2\delta\phi^* - i(K+1)\phi^{2K}\delta\phi - iK\phi^{2K}\delta\phi^*. \tag{A.7}$$

In order to separate azimuthal eigenfunctions of the transverse Laplacian, we transform Equation (A.7) from Cartesian (X, Y) to polar (R, Θ) coordinates. With the ansatz $\delta\phi(R, \Theta, Z) = \delta\phi_1(R)\exp(im\Theta + i\lambda Z) + \delta\phi_2^*(R)\exp(-im\Theta - i\lambda^* Z)$, the eigenvalue problem is then derived under the form:

$$\begin{pmatrix} \hat{L}_{11} & \hat{L}_{12} \\ \hat{L}_{21} & \hat{L}_{22} \end{pmatrix} \begin{pmatrix} \delta\phi_1 \\ \delta\phi_2 \end{pmatrix} = \lambda \begin{pmatrix} \delta\phi_1 \\ \delta\phi_2 \end{pmatrix}, \tag{A.8}$$

where $\delta\phi_1$ and $\delta\phi_2$ are independent complex functions, $\hat{L}_{11} = -\hat{L}_{22} = \Delta_\perp - \Lambda + 2\phi^2 - (K+1)\phi^{2K}$ and $\hat{L}_{12} = -\hat{L}_{21} = \phi^2 - K\phi^{2K}$.

Figure 4.6(d) in Section 4.2.1.2 shows the eigenvalues λ of the discrete (localized) perturbation modes ($\delta\phi_1$, $\delta\phi_2$) of Equation (A.8), numerically identified for different values of m. All modes have zero growth rate ($\mathrm{Im}\lambda = 0$), which implies linear stability.

B. Numerical details

In this Appendix we shortly discuss some specifications related to our numerical codes. Here we restrict ourselves to the codes used in Chapter 4, solving Equations (2.53) [respectively (4.7)]. The codes used in Chapter 3 are either using library routines, or can be seen as a simple modification of the (2D+1)-dimensional time-averaged code (Section B.1.1). Moreover, the numerical problems of Chapter 3 can be solved straight forward with sequential algorithms.

In contrast, the simulation of pulsed-beam propagation in air is very challenging from the technical point of view, and requires massively parallel computations. Simulations were realized on the COMPAQ alpha cluster (TERA) at the Commissariat à l'Énergie Atomique, Direction des Applications Militaires (CEA/DAM) in Bruyères-le-Châtel, France and on the IBM p690 cluster (JUMP) at the Forschungszentrum Jülich, Germany. Up to 128 processors were employed for runs consuming several ten thousands of CPU hours. In spite of these substantial capacities, (3D+1)-dimensional simulations of broad (cm-waisted) pulsed beams over several tens of meters could not be properly achieved in reasonable times yet.

All codes are written in Fortran90 and parallelized for distributed memory architecture by using the MPI (Message Passing Interface) library. Fast Fourier Transformations (FFTs) are performed by routines of the FFTW library, version 3.

B.1. Numerical schemes for pulsed-beam propagation in air

A split-step scheme was employed for solving Equations (2.53) in radial symmetry (B.1.2), fully transversely resolved (B.1.3), and Equation (4.7) (B.1.1). The basic idea of the split-step (or operator splitting) scheme is the following: We have an initial value problem

$$\frac{\partial}{\partial z}\psi = \hat{\mathcal{L}}\psi, \tag{B.1}$$

where $\hat{\mathcal{L}}$ is some operator. Our aim is an updating scheme to advance ψ from z to $z+\Delta z$, which we can formally write as

$$\psi(z+\Delta z) = \mathrm{e}^{\int \hat{\mathcal{L}} dz} \psi(z), \tag{B.2}$$

where $\int$ denotes $\int_z^{z+\Delta z}$. We suppose that $\hat{\mathcal{L}}$ can be written as a sum of m pieces

$$\hat{\mathcal{L}} = \hat{\mathcal{L}}_1 + \hat{\mathcal{L}}_2 + \cdots + \hat{\mathcal{L}}_m, \tag{B.3}$$

and we know an updating scheme for ψ from z to $z+\Delta z$ for each piece, valid if that piece of the operator were the only one. Then, the straight forward split-step scheme is

$$\psi(z+\Delta z) = \mathrm{e}^{\int \hat{\mathcal{L}}_1 dz} \mathrm{e}^{\int \hat{\mathcal{L}}_2 dz} \ldots \mathrm{e}^{\int \hat{\mathcal{L}}_m dz} \psi(z), \tag{B.4}$$

and again $\int$ denotes $\int_z^{z+\Delta z}$. Since in general the pieces $\int \hat{\mathcal{L}}_i dz$ do not commute, there is much to say about advancing the scheme by changing the order of the updating schemes $\exp(\int \hat{\mathcal{L}}_i dz)$ [31, 92]. However, in this short overview we restrict ourselves to the basic concepts and do not go into details.

A crucial thing for all codes is controlling the increment along the z axis Δz adaptively. Both in Equation (2.53a) and in Equation (4.7) we split the operator $\hat{\mathcal{L}}$ into the linear part $\hat{\mathcal{L}}_{lin}$, containing diffraction resp. dispersion terms, and the nonlinear part $\hat{\mathcal{L}}_{nl}$ containing all other terms. We see that $\hat{\mathcal{L}}_{lin}$ is independent of z. Thus, here a constant step-size, determined by the transverse discretization, should be sufficient. In contrast, the nonlinear operator $\hat{\mathcal{L}}_{nl}$ is strongly dependent on z, and therefore decisive for the adaptive step-size control. Let us show the principles by means of the simple example

$$\frac{\partial}{\partial z}\psi = i\frac{\partial^2}{\partial t^2}\psi + i\left|\psi\right|^2\psi. \tag{B.5}$$

Then we have $\hat{\mathcal{L}}_{lin} = i\partial_t^2$ and $\hat{\mathcal{L}}_{nl} = i\left|\psi\right|^2$. We have three constraints for Δz: The two advancing schemes $\exp(\int \hat{\mathcal{L}}_{lin} dz)$ and $\exp(\int \hat{\mathcal{L}}_{nl} dz)$ have to work, and Δz has to be small enough for our split-step scheme. The linear step can be achieved exact in Fourier space $\exp(\int \hat{\mathcal{L}}_{lin} dz) = \mathrm{FFT}^{-1}\exp(-i\omega^2\Delta z)\mathrm{FFT}$. Thus, no limitation for Δz from this scheme. For the nonlinear step we have to compute $\int |\psi|^2 dz \approx |\psi|^2 \Delta z$, the relative error of this approximation is $\sim |\psi|^4 \Delta z^2$. In order to control this relative error, we opt for $c_2 < |\psi|^2 \Delta z < c_1$. The constant c_1 guarantees a small enough error, and $c_2 < c_1$ a preferably large step-size. The split-step scheme requires to control the size of $\|\hat{\mathbb{I}} - \exp(\int \hat{\mathcal{L}}_{lin} dz)\| \sim \Delta z/\Delta t^2$ and $\|\hat{\mathbb{I}} - \exp(\int \hat{\mathcal{L}}_{nl} dz)\| \sim |\psi|^2 \Delta z$, where Δt is the increment of the transverse coordinate t. Hence, we have to introduce a third constant $c_3 > \Delta z/\Delta t^2$. Because Δt is constant during the whole run, c_3 determines a second upper limit for Δz independent from $|\psi|^2$. It turned out that $c_1 = 0.01$, $c_2 = c_1/2.5$ and $c_3 = 1$ give reasonable results, provided that the transverse discretization is sufficient.

B.1.1. (2D+1)-dimensional time-averaged code

The code integrating the (2D+1)-dimensional time-averaged [Equation (4.7)] model is the most simple one. The operator $\hat{\mathcal{L}}$ is split into

$$\begin{aligned}\hat{\mathcal{L}}_{lin} &= \frac{i}{2k_0}\left(\frac{\partial^2}{\partial x^2} + \frac{\partial^2}{\partial y^2}\right), \\ \hat{\mathcal{L}}_{nl} &= i\alpha k_0 n_2 |\psi|^2 - i\gamma|\psi|^{2K} - \frac{\beta^{(K)}}{2\sqrt{K}}|\psi|^{2K-2}.\end{aligned}$$

$\hat{\mathcal{L}}_{lin}$ is treated in Fourier space and $\hat{\mathcal{L}}_{nl}$ by multiplying with $\exp(\int \hat{\mathcal{L}}_{nl} dz)$. The integral is solved approximatively, in the easiest case we can take $\int_z^{z+\Delta z} \hat{\mathcal{L}}_{nl} dz \approx \hat{\mathcal{L}}_{nl}(z)\Delta z$. Since the FFT's require periodic boundary conditions, a transparent box is not possible. Nevertheless, a few (~ 16) absorbing layers give reasonable results, provided that the intensities of the fields leaving the box are small.

The parallelization of the scheme is straightforward. We split the $n_x \times n_y$ array, which contains the discretized complex field $\psi(x, y)$, in stripes along y. If we use p processors (both n_x and n_y should be multiples of p), proc number 0 stores $\psi(x_i, y_j)$, $i = 1, \ldots, n_x$, $j = 1, \ldots, n_y/p$, proc number 1 stores $\psi(x_i, y_j)$, $i = 1, \ldots, n_x$, $j = n_y/p+1, \ldots, 2n_y/p$ and so on. The multiplication with $\exp(\int \hat{\mathcal{L}}_{nl} dz)$ can be performed on each proc independently. Also the multiplication with $\exp(-i(k_x^2 + k_y^2)\Delta z)$ in Fourier space is local. The crucial thing is the parallel two dimensional FFT, which is composed of $n_x + n_y$ one dimensional ones. In order to perform a one dimensional FFT effectively, all relevant data should rest on a single proc. Hence, we first perform n_y FFT's with respect to x, i.e., n_y/p transformations on each proc. After that, we transpose the array, in order to split the array in stripes along x and to perform the FFT's with respect to y. Then proc number 0 stores $\widehat{\psi}(k_{yj}, k_{xi})$, $j = 1, \ldots, n_y$, $i = 1, \ldots, n_x/p$, proc number 1 stores $\widehat{\psi}(k_{yj}, k_{xi})$, $j = 1, \ldots, n_y$, $i = n_x/p+1, \ldots, 2n_x/p$ and so on.

Let us have a closer look at the necessary transposition of the array a_{ij}. For two processors ($p = 2$) this is very easy. In a first step, both procs transpose the sub-array, which will remain on the same proc. For proc number 0 it is a_{ij}, $i = 1, \ldots, n_x/2$, $j = 1, \ldots, n_y/2$, and for proc number 1 it is a_{ij}, $i = n_x/2+1, \ldots, n_x$, $j = n_y/2+1, \ldots, n_y$.

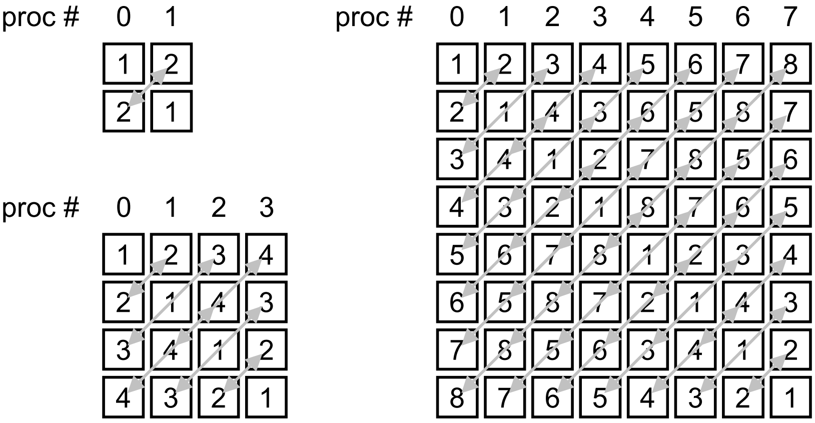

Figure B.1.: Effective send-receive scheme for transposing a 2D array for two, four and eight processors. Each column represents the memory of one proc. The figures in the caskets represent the number of the exchange step.

In a second step, both procs exchange the two remaining fourths and transpose them. The first subfigure in Figure B.1 shows this procedure schematically. For even numbers of processors p it should always be possible to find a transposing scheme, where all procs do exactly the same amount of work and are busy all the time. E.g., for $p = 4$ four steps are necessary. First, the sub-arrays along the diagonal are transposed. Second, proc 0 and 1 (resp. 2 and 3) exchange and transpose sub-arrays. Third, proc 0 and 2 (resp. 1 and 3) perform the exchange and last but not least proc 0 and 3 (resp. 1 and 2). Figure B.1 shows this scheme diagrammatically, as well as one for $p = 8$.

B.1.2. Radial code

The radial code solves Equations (2.53) in radial symmetry, that means the transverse coordinates x and y are replaced by $r = \sqrt{x^2 + y^2}$. We split the operator of Equation (2.53a) into

$$\begin{aligned} \hat{\mathcal{L}}_{lin1} &= \frac{i}{2k_0 r}\frac{\partial}{\partial r}\left(r\frac{\partial}{\partial r}\right), \qquad \hat{\mathcal{L}}_{lin2} = -ik''\frac{\partial^2}{\partial t^2}, \\ \hat{\mathcal{L}}_{nl} &= ik_0 n_2 \int \mathcal{R}(t-t')\,|\mathcal{E}(t')|^2\,dt' - i\frac{k_0}{2\rho_c}\rho_e - \frac{\sigma}{2}\rho_e - \frac{\beta^{(K)}}{2}|\mathcal{E}|^{2K-2}, \end{aligned}$$

where we treat $\hat{\mathcal{L}}_{lin1}$ with a Crank-Nicholson scheme (see Ref. [92]), $\hat{\mathcal{L}}_{lin2}$ in Fourier space and $\hat{\mathcal{L}}_{nl}$ by multiplying with $\exp(\int \hat{\mathcal{L}}_{nl} dz)$. The integral is solved approximatively, as in the (2D+1)-dimensional time-averaged code. To perform the time integration for the delayed Kerr response and the electron density [Equation (2.53c)] a simple

Euler scheme (see Ref. [92]) works, provided that the time resolution is sufficiently fine. The boundaries of the numerical box are absorbing ones in t, and transparent ones in r [93]. The parallelization scheme of the (2D+1)-dimensional time-averaged code can be adopted straight forward, but more effective schemes are possible.

B.1.3. (3D+1)-dimensional code

The (3D+1)-dimensional code solves Equations (2.53) as they are. We split the operator into

$$\begin{aligned}\hat{\mathcal{L}}_{lin} &= \frac{i}{2k_0}\left(\frac{\partial^2}{\partial x^2}+\frac{\partial^2}{\partial y^2}\right) - ik''\frac{\partial^2}{\partial t^2},\\ \hat{\mathcal{L}}_{nl} &= ik_0 n_2 \int \mathcal{R}(t-t')\,|\mathcal{E}(t')|^2\,dt' - i\frac{k_0}{2\rho_c}\rho_e - \frac{\sigma}{2}\rho_e - \frac{\beta^{(K)}}{2}|\mathcal{E}|^{2K-2},\end{aligned}$$

where we treat $\hat{\mathcal{L}}_{lin}$ in Fourier space and $\hat{\mathcal{L}}_{nl}$ by multiplying with $\exp(\int\hat{\mathcal{L}}_{nl}dz)$. The integral is solved as in the radial code. The boundaries of the numerical box are absorbing ones in x, y and t. The parallelization scheme is the same than that of the (2D+1)-dimensional time-averaged code. We simply have to substitute one element of the two dimensional array by a vector with n_t elements. The one dimensional FFT's with respect to t can be performed before the transposition.

B.2. Complementary numerical aspects

One of the sharpest constraints met in 3D numerical computing is to solve accurately individual plasma channels, whose typical size reaches a few tens of microns only. In this regard, we find it instructive to show plots of under-resolved filamentary patterns corresponding to Figure 4.10(b) and Figure 4.14 (see Figures B.2 and B.3). In this latter case, the input beam amplitude has been multiplied by a perturbed temporal Gaussian profile. The (3D+1)-dimensional simulations were performed with spatial steps limited to $\sim 100\mu$m along the x and y directions. Under-resolution leads to an artificial increase of the number of small-scale cells, caused by the coarse plasma response that cannot hold a robust channel. Energy is dissipated outwards, which contributes to increase wrongly the number of light cells. The filaments finally spread out too early, compared with the experimental data and with the results yielded by the 2D model [Equation (4.7)], integrated with much higher spatial resolution.

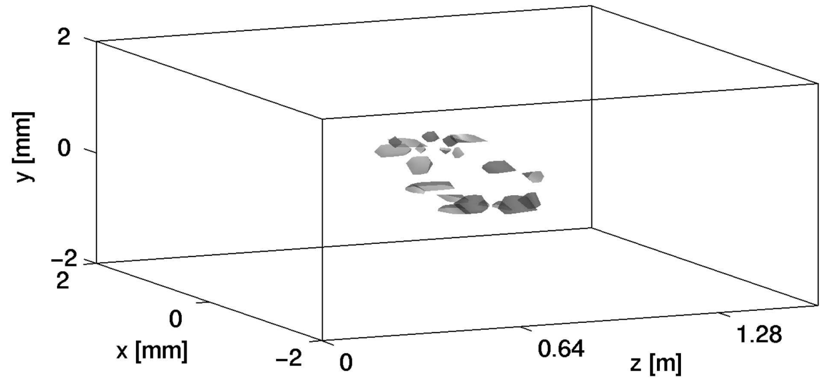

Figure B.2.: Under-resolved (3D+1) numerical results with spatial step-size $\Delta x = \Delta y \simeq 100 \mu\mathrm{m}$ for the multiple filamentation patterns shown in Figure 4.10(b)

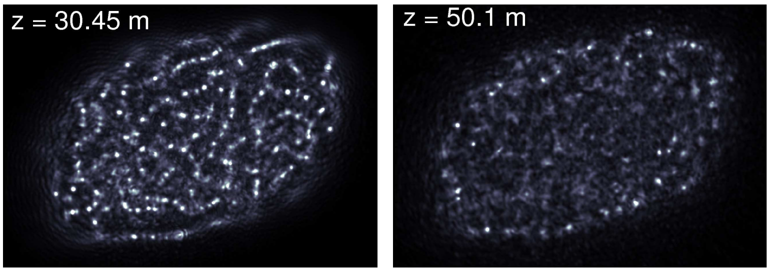

Figure B.3.: Under-resolved (3D+1) numerical results with spatial step-size $\Delta x = \Delta y \simeq 100 \mu\mathrm{m}$ for the multiple filamentation patterns shown in Figure 4.14

C. Symbols and conventions

$\hat{\mathbb{I}}$	unity operator
$\Im A$	imaginary part of A
$\Re A$	real part of A
∂_x	partial differentiation with respect to x
∇	Nabla operator $\nabla = \partial_x \vec{e}_x + \partial_y \vec{e}_y + \partial_z \vec{e}_z$
$\vec{e}_x$	unit vector in x direction
$\vec{r}$	position vector $\vec{r} = x\vec{e}_x + y\vec{e}_y + z\vec{e}_z$
Δ	Laplace operator $\Delta = \partial_x^2 + \partial_y^2 + \partial_z^2$
$\Delta_\perp$	transverse Laplace operator $\Delta_\perp = \partial_x^2 + \partial_y^2$
δ_{ij}	Kronecker $\delta_{ij} = \begin{cases} 1, & \text{if } i = j \\ 0, & \text{if } i \neq j \end{cases}$
$\delta(x)$	δ-distribution $\delta(x) = \begin{cases} \infty, & \text{if } x = 0 \\ 0, & \text{if } x \neq 0 \end{cases}$, $\int \delta(x) dx = 1$
ϵ_0	vacuum susceptibility $\epsilon_0 = 8.854187817 \times 10^{-12}$ As/Vm
$\epsilon(\omega)$	relative susceptibility
λ_0	vacuum wavelength $\lambda_0 = 2\pi c/\omega_0$
μ_0	vacuum permeability $\mu_0 = 4\pi \times 10^{-7}$ Vs/Am
$\Theta(x)$	Heavyside function $\Theta(x) = \begin{cases} 1, & \text{if } x \geq 0 \\ 0, & \text{if } x < 0 \end{cases}$
ω	frequency
ω_0	center frequency
BEC	Bose-Einstein condensate
c	velocity of light in vacuum $c = 299792458$ m/s
FFT	Fast Fourier Transformation
FWHM	Full Width Half Maximum
GVD	Group Velocity Dispersion
k_0	wavenumber in the material $k_0 = \omega_0 n(\omega_0)/c$
k'	reciprocal group velocity $k' = 1/v_g = \partial_\omega k(\omega)\vert_{\omega_0}$
k''	group velocity dispersion coefficient $k'' = \partial_\omega^2 k(\omega)\vert_{\omega_0}$

$k(\omega)$	dispersion relation $k(\omega) = \omega n(\omega)/c$
L_D	dispersion length for a Gaussian pulse $L_D = t_p^2/\lvert k''\rvert$
MPI	Multi Photon Ionization
MPA	Multi Photon Absorption
Lidar	Light detection and ranging
n	linear refractive index $n(\omega) = \sqrt{\Re\epsilon(\omega)}$
n_b	refractive index of the background material at ω_0
n_2	Kerr coefficient
NLS	Nonlinear Schrödinger Equation
P_{cr}	critical power for collapse $P_{cr} = \lambda_0^2/2\pi n_b n_2$
SVEA	Slowly Varying Envelope Approximation
t_p	pulse duration
v_g	group velocity
w_0	beam waist
z_0	Rayleigh length $z_0 = n_b \pi w_0^2/\lambda_0$

Zusammenfassung

Die vorliegende Arbeit befasst sich mit der nichtlinearen Propagation von Licht in schwach führenden Wellenleitern und in der Atmosphäre. Dabei steht die räumliche Dynamik der zu untersuchenden nichtlinearen Objekte im Vordergrund. Bei der Lichtausbreitung im Wellenleiter werden zwei unterschiedliche Regime betrachtet. Im Bereich kleiner Leistungen sind die zu erwartenden nichtlinearen Effekte klein, die Lichtführung ist rein linear. Wir leiten ein hinreichendes Kriterium für die Stabilität schwach nichtlinearer Wellenleitermoden ab. Hier ermöglicht bereits die Kenntnis der Propagationskonstanten der einzelnen linearen Wellenleitermoden eine Vorraussage. Obwohl das Kriterium nur für sehr kleine Leistungen gültig ist, zeigt das numerische Beispiel einer Standardfaser gute Übereinstimmung auch für höhere Leistungen. Im Bereich hoher Leistungen zeigen wir, dass der Wellenleiter die kritische Leistung für Kollaps signifikant erhöhen kann. Für Eingangsleistungen deutlich über der kritischen Leistung des homogenen Mediums kann eine stabile Propagation beobachtet werden. Die Erklärung für die Erhöhung der kritischen Leistung ist, dass die Wechselwirkung zwischen Feld und Wellenleiter die Selbstfokussierungsdynamik derart stört, das mehr Leistung abgestrahlt wird und für den Selbstfokussierungsmechanismus nicht mehr zur Verfügung steht.

Der zweite Teil der Arbeit beschäftigt sich mit der Ausbreitung hochintensiver ultrakurzer Laserpulse in der Atmosphäre, insbesondere mit multipler Filamentierung. Wir zeigen, dass mehrere Filamente langreichweitige Cluster ausbilden können. Zum besseren Verständnis der zugrundeliegenden transversalen Dynamik wird eine zeitlich gemitteltes Modell abgeleitet. In diesem Modell ist es möglich, die Filamente mit solitären Lösungen zu identifizieren. Simulationen des zeitlich gemittelten Modells werden mit voll zeitaufgelösten Simulationen und experimentellen Resultaten erfolgreich verglichen. Schlussendlich wird die Interaktion von Filamenten mit Partikeln, z. B. Wassertröpfchen, betrachtet. Es zeigt sich, dass Tröpfchen bis zu 2/3 des Filamentdurchmessers kein Hindernis darstellen. Wir erklären diese bemerkenswerte Selbstheilung im zuvor entwickelten Solitonenbild.

Acknowledgments

This work would not have been possible without the help, support, and inspiration of a number of people. It is a pleasure to acknowledge my debt of gratitude toward them.

First of all, I want to express my sincere thanks to my supervisors Prof. Dr. Falk Lederer from the Institut für Festkörpertheorie und -optik (Friedrich-Schiller-Universität, Jena, Germany) and Dr. Luc Bergé from the Département de Physique Théorique et Appliquée (CEA/DAM Ile de France, Bruyères-le-Châtel, France) for their continuous scientific, technical and moral support.

I am indebted to Dr. Ulf Peschel for the stimulating experience of working alongside him and for the excellent ideas he provided.

I would like to thank the people of the group in Jena, Dr. Christoph M. Etrich, Rumen Iliew, André Janasch, Oleg Jegorov, Dr. Lutz Leine, Dr. Dirk Michaelis, Dr. Thomas Pertsch, Dr. Carsten Rockstuhl and Henrike Trompeter for numerous big and small hints, helps and discussions.

I owe special thanks to Dr. S. Champeaux, Dr. Cl. Gouédard, Dr. Rachel Nuter, Dr. Françoise Simonet, Antoine Vinçotte and Dr. Helen Ward from Bruyères-le-Châtel for helpful discussions and a lot of aid to manage my daily life in France without speaking French.

I am obliged to Prof. Dr. Roland Sauerbrey, head of the Institut für Optik und Quantenelektronik (Friedrich-Schiller-Universität, Jena, Germany), who strongly supported me in my work on femtosecond filaments.

Last, but no least, I was fortunate to collaborate with the people of the group of Prof. Dr. J. P. Wolf at the Laboratoire de Spectrométrie Ionique et Moléculaire, Université Cl. Bernard Lyon 1 in France.

Ehrenwörtliche Erklärung

Ich erkläre hiermit ehrenwörtlich, dass ich die vorliegende Arbeit selbständig, ohne unzulässige Hilfe Dritter und ohne Benutzung anderer als der angegebenen Hilfsmittel und Literatur angefertigt habe. Die aus anderen Quellen direkt oder indirekt übernommenen Daten und Konzepte sind unter Angabe der Quelle gekennzeichnet.

Weitere Personen waren an der inhaltlich-materiellen Erstellung der vorliegenden Arbeit nicht beteiligt. Insbesondere habe ich hierfür nicht die entgeltliche Hilfe von Vermittlungs- bzw. Beratungsdiensten (Promotionsberater oder andere Personen) in Anspruch genommen. Niemand hat von mir unmittelbar oder mittelbar geldwerte Leistungen für die Arbeiten erhalten, die im Zusammenhang mit dem Inhalt der vorgelegten Dissertation stehen.

Die Arbeit wurde bisher weder im In- noch im Ausland in gleicher oder ähnlicher Form einer anderen Prüfungsbehörde vorgelegt.

Die geltende Promotionsordnung der Physikalisch-Astronomischen Fakultät ist mir bekannt.

Ich versichere ehrenwörtlich, dass ich nach bestem Wissen die reine Wahrheit gesagt und nichts verschwiegen habe.

Jena, den 7. April 2005

Stefan Skupin

Lebenslauf

Persönliche Daten

Name: Stefan Skupin
Geburtsdatum: 8. Mai 1976
Geburtsort: Düsseldorf

Ausbildung

1982 – 1986	Wilhelm-Hüls-Gemeinschafts-Grundschule in Hilden
1986 – 1995	Helmholtz-Gymnasium-Hilden Abschluss: Abitur
1995 – 1996	Zivildienst bei der Freizeitgemeinschaft für Behinderte und Nichtbehinderte e.V. in Hilden
1996 – 1998	Grundstudium Diplom Physik und Diplom Mathematik an der Heinrich-Heine-Universität Düsseldorf
1998 – 2001	Hauptstudium Physik an der Friedrich-Schiller-Universität Jena Abschluss: Diplomphysiker Thema der Diplomarbeit: “Simulation der Ausbreitung hochenergetischer Lichtpulse in Gasen”
seit 2001	Promotionsstudent am Institut für Festkörpertheorie und -optik der Friedrich-Schiller-Universität Jena

Jena, den 7. April 2005

Stefan Skupin